Gian Marco Melito, MSc.

Sensitivity analysis for model optimization and calibration in type B aortic dissection

Doctoral Thesis
to achieve the university degree of
Doctor of Technical Sciences

submitted to

Graz University of Technology

Supervisor
Univ.-Prof. Dr.-Ing. habil. Katrin Ellermann

Graz, February 2022

Gian Marco Melito, MSc.

Sensitivitätsanalyse zur Modelloptimierung und -kalibrierung bei Aortendissektion Typ B

Dissertation

zur Erlangung des akademischen Grades
Doktor der technischen Wissenschaften

eingereicht an der

Graz University of Technology

Betreuerin
Univ.-Prof. Dr.-Ing. habil. Katrin Ellermann

Graz, February 2022

Affidavit

I declare that I have authored this thesis independently, that I have not used other than the declared sources/resources, and that I have explicitly indicated all material which has been quoted either literally or by content from the sources used. The text document uploaded to TUGRAZonline is identical to the present doctoral's thesis.

———————————————————   ———————————————————————————
Date   Signature

Eidesstattliche Erklärung

Ich erkläre an Eides statt, dass ich die vorliegende Arbeit selbstständig verfasst, andere als die angegebenen Quellen/Hilfsmittel nicht benutzt, und die den benutzten Quellen wörtlich und inhaltlich entnommenen Stellen als solche kenntlich gemacht habe. Das in TUGRAZonline hochgeladene Textdokument ist mit der vorliegenden Dissertation identisch.

———————————————————   ———————————————————————————
Datum   Unterschrift

Thanks

Doing a doctorate is not an easy choice. But few people know what they are up against once that choice is made. Few have warned me, few have supported me in accepting this position and going forward day after day. At the beginning of my Ph.D., I had no idea what was ahead of me, and now that it is at the end, I have no idea how I could have gone on during these years.

They have been definitive years for me and for many who are close to me. There has even been a global pandemic, which no one expected, but many have been predicting for years. This pandemic is also included in this text as a fundamental part of the development of my doctorate.

I would like to dedicate this space to the people I care most about, who have supported me and believed in me, always, unconditionally.

First of all, I don't need to specify it, but there are, and there will be my parents. Without the support that my parents have given me all these years to create my own future, as I wanted, well, I would not be here right now to write these words. This thesis is dedicated to my father, who has always believed in me, is always ready to help, and always knows the right direction. He has always been a cornerstone, a "pietra" to all affections. This thesis is dedicated to my mother, whose infinite love and care I will always carry within me. Life was not fair to my mother. Life decided to take her unjustly too early and at the wrong time. Her unfailing laughter, her smile, and her caresses are just a few of the thousands of things I tremendously miss about her. Dear parents, thank you for all of this, and more, which I will not report.

My sister should deserve a whole chapter. My sister and I built our relationship one piece at a time, me away from home to study, her still too young to be independent. THE relationship of which I am most proud of in the world. No distance gives me the impression of how far away we are. My sister has always given me the grit, the energy I needed, and the most incredible pride ever. Maristella, thank you!

Then there is her, my Viki, chaotic and disorganized Viki. She has a smile that can stop the spinning world, an enchanting look it is impossible to escape. Viki has taught me a lot in these three and a half years of relationship and Ph.D. She has taught me things that only she could. Viki made me see the world in a sweeter way. She has been the sweetest pillar at a time in my life when I could see nothing but chaos, confusion, pain. I will never be able to put into words how much love I feel for her.

Next, I tried to name everyone, but I apologize in advance if I have forgotten anyone. If you know me well enough, you know that it can happen quite undoubtedly. The order is, of course, not tied to any particular criteria.

I feel the duty and pleasure to thank my supervisor, Prof. Katrin Ellermann, without whom all this would not have been possible. She believed in me. She gave me the necessary space I needed to range in a scientific field totally new to me. She gave me freedom and reassurance again when I was looking for it everywhere. Thank you.

Remaining in the academic field, how can I not mention my colleagues and now friends, with whom we shared the joys and sorrows of an unimaginable Ph.D. Thank you for the support, the laughs, the advice and opinions, the sturm, and so much more. You all have made me grow.

~ This thesis is for her
always with me from afar
together with my grandfathers.

Abstract

Aortic dissection is a complex unsolved issue in medical and biomechanics fields. It affects the main artery of the human body, the vessel that carries oxygen-rich blood from the heart to the rest of the body through branch arteries: the aorta. The dissection of the aorta occurs inside its wall, which is composed of three different layers of material, i.e., intima, media, and adventitia. The load-bearing structure of the aorta is the media, which is composed of 50 to 70 sublayers. The separation of the media layers and consecutive rupture of the intima causes the blood to flow into the newly formed cavity. The blood pressure will cause the propagation of the secondary volume, creating the aortic dissection. The new volume, in which the blood flows, is called a *false lumen.* According to the Stanford Classification System, aortic dissection initiates from the origin of an initial tear. A relative position to the ascending aorta will classify the disease as Type A aortic dissection or Type B aortic dissection.

Consequently, a profound study on aortic wall mechanics and fluid-structure interaction are at the basis of the mechanics of the disease. As for the hemodynamics of the system, it is worth mentioning the beneficial role of thrombus formation in such a disease. The hemodynamics condition in the false lumen often promotes the formation and growth of thrombi. Thrombus development in aortic dissection has been the focus of many medical studies. The thrombus was found to have a beneficial effect on a patient's prognosis. The disease's incidence is about 3 to 6 cases per 100 000 population in its acute condition. However, recent studies mention numbers up to 15 cases per 100 000 population due to better diagnostics and awareness of the disease among the medical community. Nonetheless, the disease's management is challenging due to its rapid progression, given the high uncertainty in its diagnosis and treatment. At the moment, it is still unclear what is the mechanism that initiates aortic dissection, how and how fast it propagates, and which is the best treatment to cure it.

Aortic dissection is a medical problem that benefits from the engineering approaches, like many other scientific issues. The medical field is strongly affected by high uncertainty due to the extreme variation of the human body. Here, body proportions, the morphology of internal organs, lifestyles, and living environment represent some of the challenges that modelers face when reproducing the mechanics of the human body through complex computational models. The material and failure properties of aortic walls dominate the occurrence and progression of a tear in the aorta. Numerical values of the parameters are inherently difficult to determine and include a certain level of epistemic uncertainty, i.e., the tissue may be altered by genetics, loading conditions, or traumas. Hence, the location of material and geometrical imperfections can hardly be predicted.

Sensitivity analysis is used to investigate the variations in the output of a dynamical system

caused by input values. Among various approaches, global sensitivity analysis with the variance-based method allows the analyst to focus on output variations. This approach also examines the whole input space of a model considering possible interactions among the input factors. On the contrary, a local approach will only investigate how the variation of single parameters will change the quantity of interest of the numerical model. A variance-based approach requires relevant statistical information, for instance, the probability density function of the desired model output. Given the vast amount of data that sensitivity analysis requires, the use of metamodels, such as polynomial chaos expansion, is considered. Metamodels allow the computation of more or less expensive numerical simulations and are convenient for quantitative sensitivity measures.

Sensitivity analysis is applied to reduce the uncertainty in aortic dissection detection using impedance cardiography, a non-invasive methodology primarily aimed at the medical community. Furthermore, given the lack of knowledge on the thrombus formation model, sensitivity analysis assists the process of defining the governing variables that could accelerate or inhibit its formation and growth. The use of sensitivity analysis helps to reduce the uncertainty in the modeling phase, aids the modelers in the model reduction process, and promotes the bond between engineers and physicians. While the firsts are more concerned with a mathematical and computational approach to the disease, developing new models and predictors demands a clearer understanding of the mechanics of the process and the applicability of newly developed tools.

Zusammenfassung

Die Aortendissektion ist ein komplexes, ungelöstes Problem im Bereich der Medizin und der Biomechanik. Sie betrifft die Hauptarterie des menschlichen Körpers, das Gefäß, das sauerstoffreiches Blut vom Herzen über die Nebenarterien in den Rest des Körpers transportiert: die Aorta. Die Dissektion der Aorta erfolgt innerhalb ihrer Wand, die aus drei verschiedenen Materialschichten besteht, nämlich Intima, Media und Adventitia. Die tragende Struktur der Aorta ist die Media, die sich aus 50 bis 70 Subschichten zusammensetzt. Durch die Trennung der Arterienwandschichten fließt das Blut in den neu entstandenen Hohlraum, wo det Blutdruck die Ausbreitung dieses sekundären Volumens bewirkt, wodurch die Aortendissektion entsteht. Das neue Volumen, in welches das Blut fließt, wird als falsches Lumen (*false lumen*) bezeichnet. Nach dem Stanford-Klassifikationssystem geht die Aortendissektion vom Ursprung eines ersten Risses aus. Anhand der relativen Lage zum Aortenbogenwird die Erkrankung als Typ-A- oder Typ-B-Aortendissektion klassifiziert.

Folglich ist eine gründliche Untersuchung der Aortenwandmechanik und der Fluid-Struktur-Interaktion die Grundlage der Mechanik der Aortendissektion. Was die Hämodynamik des Systems betrifft, so ist die günstigste Rolle der Thrombusbildung bei einer solchen Erkrankung zu erwähnen. Zweifellos begünstigen die hämodynamischen Bedingungen im falschen Lumen häufig die Bildung und das Wachstum von Thromben. Die Thrombusbildung bei Aortendissektion ist Gegenstand zahlreicher medizinischer Forschungsarbeiten, die zu dem Schluss kommen, dass sich der Thrombus rasch positiv auf die Prognose des Patienten auswirkt. Die Inzidenz der Krankheit liegt im akuten Zustand bei etwa 3 bis 6 Fällen pro 100 000 Einwohner. Neuere Studien gehen jedoch von bis zu 15 Fällen pro 100 000 Einwohner aus, was auf eine bessere Diagnostik und die Sensibilisierung der medizinischen Fachwelt für diese Krankheit zurückzuführen ist. Dennoch ist die Behandlung der Krankheit aufgrund ihres raschen Fortschreitens und der großen Unsicherheit bei Diagnose und Behandlung eine Herausforderung. Derzeit ist noch immer unklar, welcher Mechanismus die Aortendissektion auslöst, wie und wie schnell sie sich ausbreitet und welche Behandlung am besten geeignet ist, sie zu heilen.

Die Aortendissektion ist ein medizinisches Problem, das wie viele andere wissenschaftliche Fragen auch von der Technik profitiert. Medizinische Fragen sind aufgrund der extremen Variabilität des menschlichen Körpers von einer großen Unsicherheit geprägt. Die Körperproportionen, die Morphologie der inneren Organe, die Lebensgewohnheiten und das Lebensumfeld sind nur einige der Herausforderungen, denen sich die Modellierer stellen müssen, wenn sie die Mechanik des menschlichen Körpers mit Hilfe komplexer Computermodelle nachbilden wollen. Die Material- und Versagenseigenschaften der Aortenwände dominieren das Auftreten und Fortschreiten eines Risses in der Aorta. Die numerischen Werte der Parameter sind von Natur aus schwer zu bes-

timmen und beinhalten ein gewisses Maß an epistemischer Unsicherheit, d.h. das Gewebe kann durch Genetik, Belastungsbedingungen oder Traumata verändert werden, und der Ort solchen Unvollkommenheit lässt sich kaum vorhersagen.

Mit Hilfe der Sensitivitätsanalyse werden die durch die Eingangswerte verursachten Schwankungen in der Ausgabe eines dynamischen Systems untersucht. Die Methode, die es dem Analysten besser ermöglicht, sich auf die Ausgangsvariationen zu konzentrieren, ist eine globale Sensitivitätsanalyse, die eine varianzbasierte Methode verwendet. Bei der globalen Sensitivitätsanalyse wird der gesamte Eingaberaum eines Modells untersucht, wobei mögliche Wechselwirkungen zwischen den Eingabefaktoren berücksichtigt werden. Im Gegensatz dazu wird bei einem lokalen Ansatz nur untersucht, wie die Variation einzelner Parameter die interessierende Größe des numerischen Modells verändert. Ein varianzbasierter Ansatz erfordert die Erstellung relevanter statistische Informationen, z. B. der Wahrscheinlichkeitsdichtefunktion der gewünschten Modellausgabe. Angesichts der großen Datenmengen, die für die Sensitivitätsanalyse erforderlich sind, wird die Verwendung von Metamodellen wie der Polynomial Chaos Expansion in Betracht gezogen. Metamodelle ermöglichen die Berechnung von numerischaufwändigen Simulationen und sind für quantitative Sensitivitätsmessungen sehr vorteilhaft.

Die Sensitivitätsanalyse wird angewandt, um die Unsicherheit bei der Erkennung von Aortendissektionen mit Hilfe der Impedanzkardiographie zu verringern, einer nicht-invasiven Methode, die in erster Linie in der Medizin verwendet wird. Angesichts des fehlenden Wissens über das Modell der Thrombusbildung hilft die Sensitivitätsanalyse außerdem bei der Definition der Variablen, die die Bildung und das Wachstum des Thrombus beschleunigen oder hemmen könnten. Der Einsatz von Sensitivitätsanalysen trägt dazu bei, die Unsicherheit in der Modellierungsphase zu verringern, unterstützt den Modellierern bei der Modellreduktion und fördert die Verbindung zwischen Ingenieuren und Ärzten. Während sich die Erstgenannten eher mit einem mathematischen und rechnerischen Ansatz für die Krankheit befassen, erfordert die Entwicklung neuer Modelle und Prädiktoren ein klareres Verständnis der Mechanik des Prozesses und der Anwendbarkeit neu entwickelter Instrumente.

List of scientific contributions

This thesis is mainly based on the work of the author during his work in the LEAD project "**Mechanics, Modeling and Simulation of Aortic Dissection**" at Graz University of Technology. The published scientific articles are listed below and are listed in chronological order. The thesis reports only some of the scientific work produced in this project. To highlight the reported work, a star ($\star$) is used as bullet point.

Journal articles

- Ranftl et al. [130], Bayesian Uncertainty Quantification with Multi-Fidelity Data and Gaussian Processes for Impedance Cardiography of Aortic Dissection - Published in: *Entropy*, 2019
  https://doi.org/10.3390/e22010058

- $\star$ Badeli et al. [10], Electrode positioning to investigate the changes of the thoracic bioimpedance caused by aortic dissection – a simulation study - Published in: *Journal of Electrical Bioimpedance*, 2020
  https://doi.org/10.2478/joeb-2020-0007

- $\star$ Melito et al. [103], Sensitivity Analysis of a Phenomenological Thrombosis Model and Growth Rate Characterisation - Published in: *Journal of Biomedical Engineering and Biosciences (JBEB)*, 2020
  https://jbeb.avestia.com/2020/004.html

- $\star$ Melito et al. [105], Sensitivity analysis study on the effect of the fluid mechanics assumptions for the computation of electrical conductivity of flowing human blood - Published in: *Reliability Engineering & System Safety*, 2021
  https://doi.org/10.1016/j.ress.2021.107663

Conference papers

- $\star$ Melito et al. [102], Sensitivity analysis for electrical detection of aortic dissection - Published in: *Proceedings in Applied Mathematics and Mechanics - 90th Annual Meeting of the International Association of Applied Mathematics and Mechanics (GAMM)*, 2019
  https://doi.org/10.1002/pamm.201900062

- Ranftl et al. [129], On the Diagnosis of Aortic Dissection with Impedance Cardiography: A Bayesian Feasibility Study Framework with Multi-Fidelity Simulation Data - Published in: *Proceedings / Electrochemical Society*, 2019
  `https://doi.org/10.3390/proceedings2019033024`

- Egger et al. [51], A comprehensive Workflow and Framework for immersive Virtual Endoscopy of dissected Aortae from CTA Data - Published in: *Medical Imaging 2020 - Image-Guided Procedures, Robotic Interventions, and Modeling*, 2020
  `https://doi.org/10.1117/12.2559239`

- Reinbacher-Köstinger et al. [134], Numerical simulation of various electrode configurations in impedance cardiography to identify aortic dissection - Published in: *17th International Conference on Electrical Bioimpedance, ICEBI 2019 - ICEBI 2019, Joinville, Santa Catarina, Brazil, 9-14 June 2019*, 2020
  `https://doi.org/10.1007/978-981-13-3498-6_7`

- Melito et al. [104], Sensitivity analysis of a hemodynamic-based model for thrombus formation and growth - Published in: *Proceedings of the 6th World Congress on Electrical Engineering and Computer Systems and Sciences (EECSS'20) - ICBES'20*, 2020
  `https://doi.org/10.11159/icbes20.127`

List of symbols

Greek alphabet

	Unit	Description
$\boldsymbol{\alpha}$	-	Multi-index of the PCE
α_i	-	Component of multi-index $\boldsymbol{\alpha}$
α_{FL}	rad	Angle of relative position between false and true lumen
β	rad	RBC deformation angle
β_{th}	m^2	Shear-enhancing coefficient for the diffusion of platelets
γ_d	-	Orthogonalization normalization constant in the degree d
$\gamma_{\boldsymbol{\alpha}}$	-	Orthogonalization normalization constant in multi-dimensional PCE
$\dot{\gamma}$	s^{-1}	Shear rate
Γ	-	Boundary of input domain
δ_{qd}	-	Kronecher delta in the indices q and d
Δ_{EE}	-	Distance between two sample points in the EE method
$\Delta\sigma_{\mathrm{bl}}$	%	Blood electrical conductivity change
ε	-	Error, or approximation error
$\varepsilon_{\mathrm{emp}}$	-	Empirical error for PCE coefficients
$\varepsilon_{\mathrm{LOO}}$	-	Leave-one-out error for PCE coefficients
$\varepsilon^{(e)}$	F m^{-1}	Electrical permittivity
ζ_{H}	-	Blood electrical conductivity variation per hematocrit level
η	Pa s	Blood viscosity
η_{pl}	Pa s	Blood plasma viscosity
η_0	Pa s	Zero-shear fluid viscosity
η_∞	Pa s	High shear rate fluid viscosity
Θ	-	Input sample
$\theta^{(k)}$	-	Input sample point
λ	s	Shape function parameter for Carreau viscosity model

	Unit	Description
μ_{RBC}	$\mathrm{N\,m^{-1}}$	Membrane shear modulus of RBC
μ_i	-	Mean of variable x_i
$\check{\mu}_i$	-	Mean of EE_i
$\check{\mu}_i^*$	-	Mean of $|EE_i|$
μ_y	-	Mean of output y
ξ	-	Percentile score
Ξ	-	Output sample
ρ	$\mathrm{kg/m^3}$	Fluid, or blood, density
ϱ_i	-	Pearson's product moment correlation coefficient
$\sigma^{(e)}$	$\mathrm{S\,m^{-1}}$	Electrical conductivity
σ_{bl}	$\mathrm{S\,m^{-1}}$	Bulk flowing blood electrical conductivity
σ_{cv}	$\mathrm{S\,m^{-1}}$	Blood electrical conductivity of a control volume
σ_i	-	Standard deviation of variable x_i
$\sigma(\blacklozenge)$	-	Standard deviation of quantity $\blacklozenge$
$\check{\sigma}_i$	-	Standard deviation of EE_i
σ_i^2	-	Variance, or partial variance, of variable x_i
σ_{ij}^2	-	Partial variance of variable x_i and x_j
$\sigma_{i_1,\dots,i_s}^2$	-	Generic partial variance of the model
σ_{pl}	$\mathrm{S\,m^{-1}}$	Plasma electrical conductivity of a control volume
σ_{st}	$\mathrm{S\,m^{-1}}$	Stationary blood electrical conductivity
σ_{th}	$\mathrm{S\,m^{-1}}$	Human thorax electrical conductivity
σ_y	-	Standard deviation of output y
τ_{EE}	-	Trajectory indicator of the EE method
$\boldsymbol{\tau}$	Pa	Shear, or deviatoric, stress tensor
τ_o	s	Time constant for parallel orientation of RBC
τ_d	s	Time constant for RBC from disoriented to aligned
υ	m	Azimuth in the cylindrical coordinate system
$\phi_d(\blacklozenge)$	-	Univariate, i.e., one-dimensional, basis function of degree d
ϕ_{th}	-	Degree of local thrombosis
$\Phi_{\boldsymbol{\alpha}}(\blacklozenge)$	-	Multivariate, i.e., multi-dimensional, basis function for the PCE
$\dot{\Phi}_{\mathrm{c}}$	$\mathrm{m^3/s}$	Thrombus characteristic growth rate
φ	-	Stationary to pulsating flow ratio
$\Psi(\blacklozenge)$	-	Vector of multivariate polynomials of the PCE

	Unit	Description
ω	$\mathrm{rad\,s^{-1}}$	Angular frequency
$\omega^{(e)}$	$\mathrm{rad\,s^{-1}}$	Phasor angular frequency
Ω	-	Spatial input domain

Latin alphabet

	Unit	Description
A	m^2	Cross-section area
a_0	m	Minor semi-axis ellipsoidal RBC
a_d	m	Deformed minor semi-axis ellipsoidal RBC
$\mathcal{A}^{M,d}$	-	Set of PCE indices for a surrogate of dimension M and degree d
$\mathcal{A}_i$	-	Set of PCE non-negative indices in i
$\mathcal{A}_{T,i}$	-	Set of PCE non-negative indices including all i combinations
b_0	m	Major semi-axis ellipsoidal RBC
b_d	m	Deformed major semi-axis ellipsoidal RBC
B	-	Model output dimension
b_i	-	Linear regression coefficient
$c,\ c'$	-	Polynomial coefficients
$\boldsymbol{c}$	-	Vector of polynomial coefficients
$\widetilde{\boldsymbol{c}}$	-	Estimated vector of polynomial coefficients from least-square method
$(c)_d$	-	Falling factorial Pochhammer symbol
$c_{\boldsymbol{\alpha}}$	-	Polynomial coefficients for multi-dimensional PCE
c_{AP}	$\mathrm{mol/m}^3$	Activated platelets concentration
c_{BP}	$\mathrm{mol/m}^3$	Bounded platelets concentration
c_{c}	$\mathrm{mol/m}^3$	Coagulant concentration
c_h	-	Polynomial coefficients for 1D PCE in the index h, s.t. $0 \leqslant h \leqslant d$
$C(r),\ C_{\mathrm{a}},\ C_{\mathrm{b}},\ C_{\mathrm{r}}$	-	Orientation and deformation terms for RBC
d	-	Generic polynomial degree

	Unit	Description
d	-	Differential operator
∂	-	Partial differential operator
$\boldsymbol{D}$	-	Rate-of-deformation tensor
D_b	m^2/s	Brownian diffusion coefficient of platelets
D_c	m^2/s	Diffusion coefficient of coagulant
$D_{\mathrm{c}\dot{\gamma}}$	m^2/s	Shear-enhanced diffusion coefficient of coagulant
$D_{\mathrm{p}\dot{\gamma}}$	m^2/s	Shear-enhanced diffusion coefficient of platelets
$D_{\mathrm{T_R}}$	m^2/s	Blood self diffusion coefficient
DF	-	Damage factor induced by AD
EE_i	-	Elementary effect of variable x_i
$\mathbb{E}\left[\blacklozenge\right]$	-	Mean operator
f	s^{-1}	Frequency
$f(r)$	-	Orientation function of the RBC in a cylinder
F	-	Deformation term of RBC
$g(\blacklozenge)$	-	Function, or computational model
$\widetilde{g}(\blacklozenge)$	-	Surrogate model of $g(\blacklozenge)$
g_0	-	Model constant as result of the ANOVA decomposition of $g(\blacklozenge)$
g_i	-	Univariate term as result of the ANOVA decomposition of $g(\blacklozenge)$
g_{ij}	-	Bivariate term as result of the ANOVA decomposition of $g(\blacklozenge)$
$g_{i_1,\ldots,i_s}$	-	Multivariate term as result of the ANOVA decomposition of $g(\blacklozenge)$
h	-	Generic polynomial degree
H	-	Blood hematocrit
i	-	Random variable index
j	-	Imaginary unit
k	-	Sample point index
k_1	m^3/s	Reaction rate constant
k_2	1/s	Reaction rate constant
K^M	-	Unit cube domain of dimension M
k_BP	mol/m^3/s	Bounded platelets reaction rate constant for production
k_c	mol/m^3/s	Reaction rate constant for coagulant production

	Unit	Description
k_{th}	kg/m^3/s	Constant coefficient for the sink term in Navier-Stokes equation
L	m	Length, or cylindrical length
$L^2_{p(x)}(S_{\mathcal{X}})$	-	Space of mean-square integrable functions defined in $S_{\mathcal{X}}$
m	-	Generalized Reynolds number coefficient
m_{r}	-	Aortic radius multiplier
m_{v}	-	Aortic blood velocity multiplier
M	-	Model input dimension
n	-	Period, or cycle, counter
$\boldsymbol{n}$	-	Normal vector
n_{η}	-	Shape function parameter for Carreau viscosity model
n_{RBC}	1/m^3	Total number of RBC per unit volume
$n_{\parallel}$	1/m^3	Number parallel RBC to the flow per unit volume
$\mathbf{N}$	-	Set of natural numbers
$\mathcal{N}(\bullet, \bullet)$	-	Gaussian, or normal, probability density function
N_c	-	Cardinality of the PCE space
N_q	-	Number of quadrature points
N_s	-	Sampling dimension
N_{EE}	-	Number of trajectories in the EE method
p_{EE}	-	Even number indicating grid level in EE method
p	Pa	Fluid pressure
p'	-	Quasi-norm degree
$p(\bullet)$	-	Probability density function
$P_d(\bullet)$	-	General polynomial formulation in the variable $\bullet$ of generic degree d
${}_rP_s$	-	Hypergeometric representation of orthogonal polynomial
$\mathbb{P}^M_d(\bullet)$	-	Space of all polynomials of dimension M and degree up to d in the variable $\bullet$
q	-	Quadrature point index
Q	m^3/s	Fluid flow rate
Q_{s}	m^3/s	Steady component of pulsating fluid flow rate
Q_{o}	m^3/s	Oscillating component of pulsating fluid flow rate
r	m	Radial, or axial, distance in the cylindrical coordinate system (r, υ, z) from the z-axis

	Unit	Description
R	m	Radius of a cylinder, lumen
R^2	-	Coefficient of determination, goodness-of-fit
R_A	m	Radius of the aortic arch
R_{FL}	m	Radius of the aortic false lumen
R_L	m	Reattachment length in BFS geometry
R_{TL}	m	Radius of the aortic true lumen
$\mathbb{R}$	-	Set of real numbers
$\mathbb{R}^M$	-	M-dimensional set of real numbers
$\mathbb{R}^{\blacklozenge,\diamond}$	-	Set of real matrices with $\blacklozenge$ rows and $\diamond$ columns
Re	-	Reynolds number
Re_{gen}	-	Generalized Reynolds number
$\mathcal{S}$	-	Set of indices composed by all combination of input indices
$S_\blacklozenge$	-	Support of the domain $\blacklozenge$
S_i	-	First Sobol index for the variable x_i
S_i^{T}	-	Total Sobol index for the variable x_i
SRC	-	Standard regression coefficient
t	-	Time variable
t_c	-	Thrombus characteristic growth time
T	s	Period or cycle
T_R	s	Residence time
$T_{i_1,\dots,i_s}$	-	Indices combination in a generic domain
$\boldsymbol{u}$	-	Fluid velocity field
u_z	-	Fluid velocity z component
u_r	-	Fluid velocity r component
u_υ	-	Fluid velocity υ component
$\mathcal{U}(\blacklozenge,\blacklozenge)$	-	Uniform probability density function
V	V	Electric potential
$\mathbb{V}[\blacklozenge]$	-	Variance operator
$w^{(i)}$	-	Quadrature weights for the point $x^{(i)}$
Wo	-	Womersley number
$\mathcal{X}$	-	Model input space, or domain
x	-	Generic random variable
x_i	-	Input random variable in the index i, s.t. $0 \leqslant i \leqslant M$

	Unit	Description
$\boldsymbol{x}$	-	Input random vector
$\mathcal{Y}$	-	Model output space, or domain
y	-	Output random variable
$\boldsymbol{y}$	-	Output random vector
Z	Ω	Electrical impedance
$\mathbb{Z}$	-	Set of integers
$\mathbb{Z}_0$	-	Set of non-negative integers
$\mathbb{Z}_0^M$	-	M-dimensional set of non-negative integers
z	m	Axial coordinate, or height, in the cylindrical coordinate system (r, υ, z)

Mathematical symbols

Symbol	Description
$\blacklozenge_{\sim i}$	complementary of. The quantity $\blacklozenge$ is considered without the i-th component
$\blacklozenge_{\mathrm{t}}$	Threshold value
$\blacklozenge_{\mathrm{w}}$	Value at the geometrical wall
:	defined as
$\approx$	Approximation operator
$\sim$	distributed, following
$\cdot$	Dot product
$>, \geqslant$	greater than, greater than or equal to
$<, \leqslant$	smaller than, smaller than or equal to
$\mathrm{cov}(\blacklozenge, \blacklozenge)$	Covariance operator
$[\blacklozenge, \ldots, \blacklozenge_i]$	i-dimensional vector components notation
$(\blacklozenge, \ldots, \blacklozenge_i)$	i-dimensional index components notation
$[\blacklozenge \vert \blacklozenge]$	Conditional variance
$\in$	is member of
$\rightarrow$	... to ..., mapping functional from domain to codomain
$\blacklozenge$	Generic quantity
∞	Infinity
$\mapsto$	maps ... to ...

Symbol	Description
min	minimum of
max	maximum of
∇	Nabla operator
∇^2	Laplace operator
$\nabla\blacklozenge$	Gradient operator
$\nabla\cdot$	Divergence operator
$\|\blacklozenge\|_p$	p-norm of the vector $\blacklozenge$
$\prod$	Product operator
$\{\blacklozenge\}$	Set definition notation
$\subseteq$	subset of ...
$\|$	such that
$\sum$	Sum operator
$\text{tr}(\blacklozenge)$	Trace of $\blacklozenge$
$\dot{\blacklozenge}$	Time derivative
$\tilde{\blacklozenge}$	Surrogate
$\hat{\blacklozenge}$	Amplitude
$\bar{\blacklozenge}$	Spatial average
$\underline{\blacklozenge}$	Complex number
$\langle\blacklozenge\rangle$	Temporal, or cycle, average

Acronyms

Acronym	Description
1D	One-dimensional
2D	Two-dimensional
3D	Three-dimensional
AAT	All at time
AD	Aortic dissection
ANOVA	Analysis of variance
AP	Activated platelets
bpm	meat per minute
BCA	Brachiocefalic artery
BFS	Backward-facing step

Acronym	Description
CFD	Computational fluid dynamics
CVD	Cardiovascular disease
CO	Cardiac output
DOE	Design of experiments
EE	Elementary effect method
FEM	Finite element method
FL	False lumen
FSI	Fluid-structure interaction
ICG	Impedance cardiography
LARS	Least-angle regression
LCA	Left common carotid artery
LHS	Latin hypercube sampling
LSCA	Left subclavian carotid artery
MC	Monte Carlo
OAT	Once at time
PCE	Polynomial chaos expansion
PDF	Probability density function
QoI	Quantity of interest
RBC	Red blood cell
RP	Resting platelets
SA	Sensitivity analysis
SV	Stroke volume
s.t.	such that
TAAD	Type A aortic dissection
TBAD	Type B aortic dissection
TEVAR	Thoracic endovascular aortic repair
TL	True lumen
UQ	Uncertainty quantification
WSS	Wall shear stress

xxx

Contents

Contents

List of Figures

List of Figures

List of Figures

List of Tables

Part I.

Introduction to aortic dissection and sensitivity analysis

1. Introduction

1.1. The medical problem

The human cardiovascular system is composed of the heart as its center and primary source of energy, veins, arteries, and capillaries. The aorta is the first blood conducting vessel that distributes blood into the whole organism from the heart. The aortic wall comprises three layers, namely the intima, the media, and the adventitia, see Fig. 1.1. The intima, i.e., the innermost layer, is formed by endothelial cells and, in physiological (healthy) conditions, it is in contact with the blood flow. The media owes its mechanical properties to the corrugated structure of collagen and smooth muscle cells layers, which gives elasticity and compliance to the whole structure of the aorta. Finally, the more collagen-rich adventitia protects the vessel from the outside and creates the interface to the surrounding tissues and vasa vasorum. The aorta is subdivided into different sections, see Fig. 1.2, to ensure accurate medical classification. The largest separation of the aorta occurs at the diaphragm height, where the thoracic and abdominal aorta are distinguished.

According to the World Health Organization [121], cardiovascular disease (CVD) is the number one cause of death in the human population, causing 17.9 million deaths each year. Some other CVDs included in the statistics are: coronary artery disease, congenital heart disease, deep vein thrombosis, and pulmonary embolism, to name the most prevalent. All of them are known in the medical field to be often lethal and require complex treatment [121]. The aorta itself is subjected to several diseases, of which aortic dissection (AD) is also classified as a CVD.

AD is a complex unsolved medical issue in the medical and biomechanics field. It is a pathological condition that affects the wall of the aorta. The wall is damaged so that a tear forms on the intima layer exposing the media layer to the blood flow. Here, the high velocity of the fluid, together with the presence of elevated shear stress on the collagen fibers, creates the perfect condition for the separation between the layers of the media. A new cavity, namely the *false lumen* (FL), is formed where the blood starts to flow. When AD occurs, the remaining healthy part of the aorta is also called *true lumen*. Single or multiple intimal tears grant the communication between the lumina [69], in which case the first tear along the flow direction is called proximal tear, and the following distal tears. The high mechanical force of the blood flow may impose continuous FL propagation. An illustration of AD initiation is provided in Fig. 1.1.

Different AD conditions have been categorized in two different classifications based on the need for surgical or medical management [42], namely the DeBakey [43] and the Stanford classifications [42]. The former considers the expansion of the disease besides the intimal tear location. The latter is used in the current text. The AD is classified by the Stanford classification system in

1. Introduction
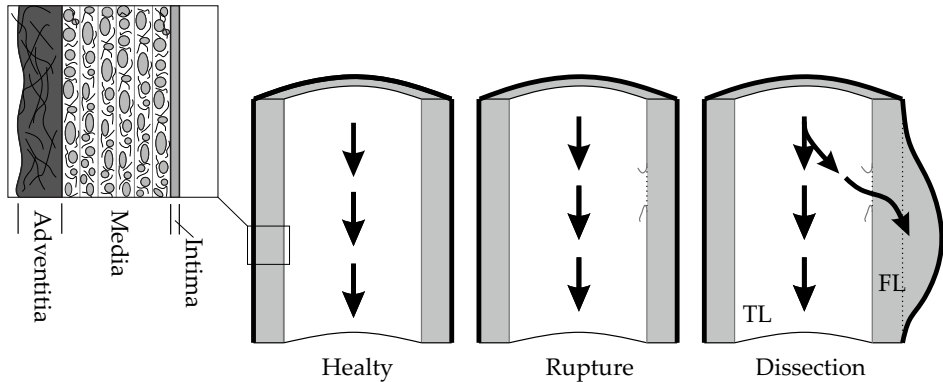
Figure 1.1.: Initiation of aortic dissection starting from a rupture of the intima layer. Dissection formation in the media layer causing separation of the layer separation and formation of true lumen (TL) and false lumen (FL). On the left, the adventitia, media, and intima layers of the aortic wall are shown. Image not in scale and inspired by Gasser et al. [61] and Surgery [159].
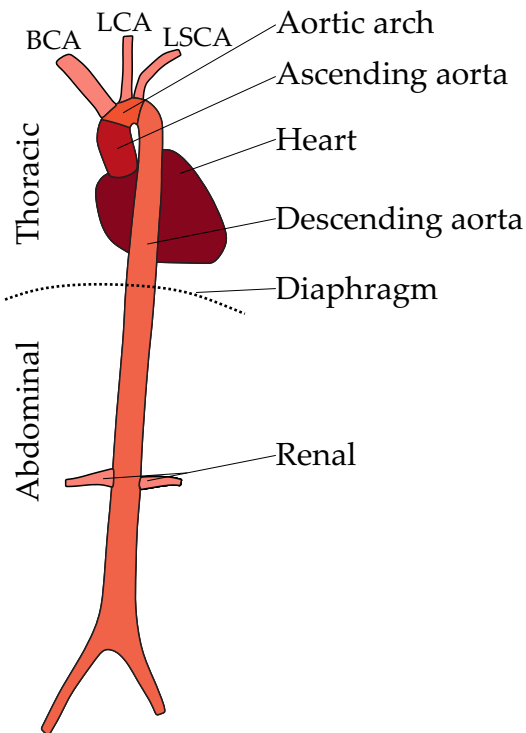
Figure 1.2.: Schematics of the aortic sections and arteries. The thoracic aorta is characterized by the presence of the brachiocefalic artery (BCA), the left common carotid artery (LCA), and the left subclavian artery (LSCA). The abdominal aorta is composed by many more artery other than the renal ones, however they are not represented here. Image not in scale and inspired by Šťásek et al. [183].

DeBakey I   DeBakey II   DeBakey IIIa   DeBakey IIIb

Stanford type A   Stanford type B
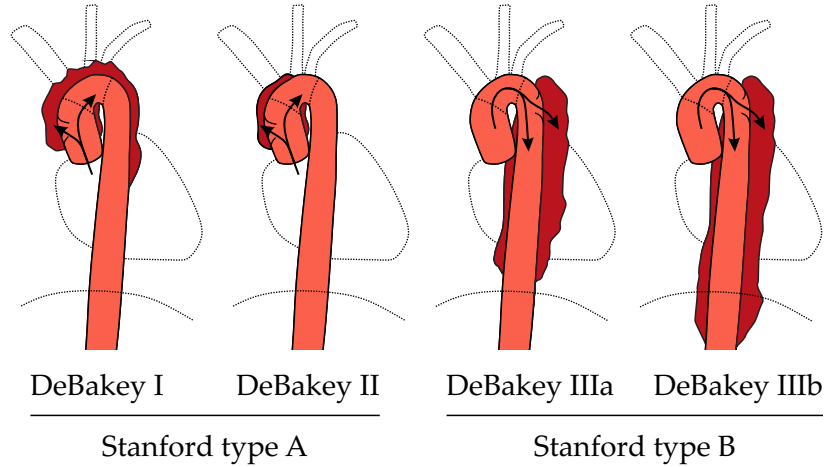
Figure 1.3.: Stanford and DeBakey classifications of Aortic Dissection: (left) Type A, or TAAD, that originates from the ascending aorta and (right) Type B, or TBAD, in which the aortic tear involves the descending aorta. Image not in scale and inspired by Murillo et al. [116].

Type A AD (TAAD) when the dissection enwraps the ascending aorta, or Type B AD (TBAD) when the tear is initiated in the descending thoracic aorta, see Fig. 1.3. The latter accounts for 25 % to 30 % of all AD, affecting primarily men. Both classifications do not include cases in which the dissection involves the aortic arch but not the ascending aorta. However, new classification systems are currently being developed [41]. TBAD can be further classified as complicated or uncomplicated. Complicated TBAD is characterized by several pathologies, of which malperfusion syndrome and aortic rupture are some [118]. Approximately 25 % to 40 % of TBAD are classified as complicated [4].

AD classification is also based on *chronicity*, i.e., the state of the disease to become chronic and have long duration. AD is defined as hyperacute when it lasts at most 24 h, acute when it continues for a week, subacute for a month, and chronic when its presence endures for more than a month. Acute AD usually requires urgent surgical repair [126]. However, type A patients have more chances of success when treated surgically, while type B dissection has a lower mortality rate with medical treatment [27, 69], see Fig. 1.4. From the Kaplan-Meier survival curves it is evident that TBAD has more chances of success compared to TAAD. In the late 1990s, the AD's death rate was about 3 to 4 cases per 100,000 persons [67, 110]. Lately, the yearly incidence was reported to be around 15 cases per 100 000 persons [93]. The reason of this discrepancy is given primarily by medical advances in diagnosis. AD management, either medical or surgical, is highly complex given the high uncertainty in diagnosis, treatment, and monitoring. In addition, the propagation speed and mode of the FL are also still unclear. The initiation event is also obscure; however, most AD patients present arterial wall abnormality or hypertension. Hypertension, which is high blood pressure, primarily chronic, is associated with aortic dissection as a primary cause [4, 136]. Connective tissue diseases are also considered as causes for AD. Examples are Marfan syndrome and Ehlers-Danlos syndrome [4]. An aortic aneurysm is considered both a cause
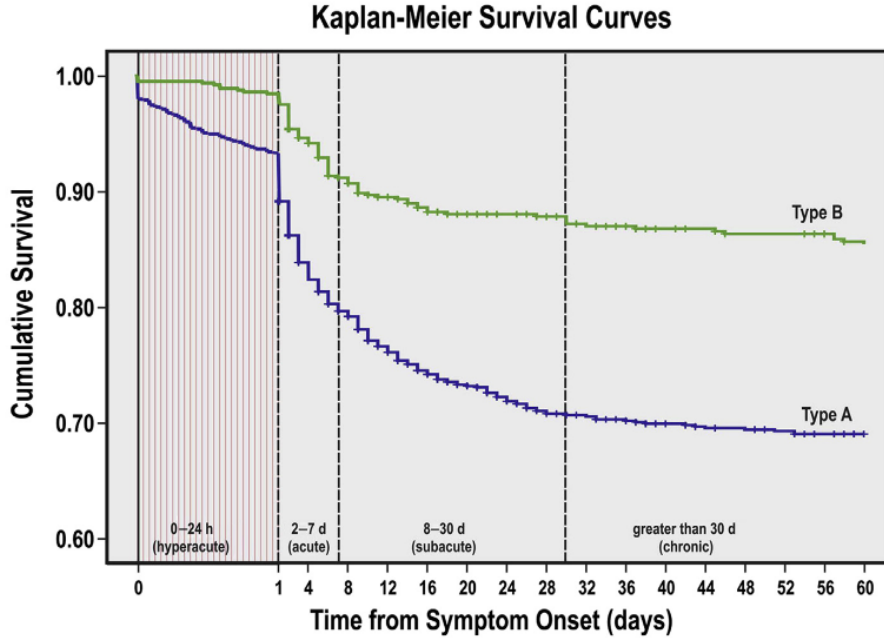
Figure 1.4.: Kaplan-Meier survival curves for Type A and Type B aortic dissection [27].

and a consequence of AD. Both are caused by the aortic wall weakening, particularly the intima or the media layers. Among the risk features, there is TL diameter larger than 40 mm [175] or FL diameter larger than 22 mm [152], patent or partially thrombosed FL [167], and proximal tear size greater than or equal to 10 mm [165]. Although beneficial to determine the gravity of the AD condition, the risk features are hardly collectible, requiring nonsimple diagnostic processes, e.g., computerized tomography or magnetic resonance imaging scan.

The medical field deals with extreme human variability: patients have different morphological characteristics, lifestyles, or habits. A patient's clinical history may also affect health characteristics in ways that are still not clear. Physicians have overcome this issue with the help of clinical expertise and statistics. Therapies, treatments, and protocols often come from statistical analysis on a large population to find the best available therapy. For example, a new surgical treatment requires a large study on new techniques and approaches, validation through the scientific literature, and final approval from the ethical committee. Same process is required for the case of new medical treatments. In addition, the choice of study population is subject to additional requirements to be met. In the case of CVD, the vascular surgeon has the duty to select the right sampling in order to initialize an innovative methodology. Therefore, the medical approach aims to find a clinical solution that may fit the highest number of individuals.

1.2. The engineering perspective

Over the past decades, engineering has increasingly aided the medical field with more elaborated computational models[1], particularly in the cardiovascular field; some examples are given in [89, 95, 96, 155, 156]. Engineers employ computational models to simulate a system, optimize it by input domain manipulation, and eventually extract decisions. However, the high human variability is often a complex issue hampering the modeling phase, especially when the transition from computational model to clinical phase is expected. Model uncertainties, both aleatory and epistemic, are common and unavoidable due to the dynamic and complex system in consideration. In addition, model errors add up to model uncertainties [79]. This situation makes it difficult to decide the model complexity that would describe the system the best.

The different approaches between the engineering world and the medical field in solving problems are the main obstacle repeatedly encountered when implementing computational models as a medicine-support tool. Sometimes, such implementation is even impossible due to various other reasons. Consequently, the creation of a strong link between the two disciplines should be encouraged. Achieving and solidifying such a link is possible by reducing model uncertainty and reducing the amount of medical measurement required of the patient.

As Hanha [70] anticipated and then confirmed by many others [53, 133], model development has to deal with finding the best compromise between model completeness and propagation error [141]. On the one hand, increasing the former would better describe the system, but a more significant number of uncertain variables in the input domain will increase the overall uncertainty. On the other hand, model assumptions and model dimension reduction ease the model computation, leading to an insufficient description of the physics and physiology of the system. The error, thus uncertainty, optimization is also known as the conjecture of O'Neil [120] and visualized in Fig. 1.5.

An uncertainty compromise is often complicated in the medical engineering field, and unsuccessful attempts lead to widespread model skepticism [86]. Increasing the number of measurements and tests on a patient translates into less induced uncertainty in the system. However, this will eventually burden the patients and require more time in the hospitalization process. Successful and mature computational models lead to a model-aided diagnosis, intervention planning, and risk stratification [25, 124, 153]. Model personalization, i.e., translating the model into patient-specific, is mandatory to make the model an effective clinical supporting tool. Model personalization means that boundary conditions, parameters, and initial conditions are extracted from the patient's condition. However, daily physiological variation and measurements uncertainty are common issues making data implementation hardly successful [45]. In the biomechanics field, modeling techniques such as finite element method (FEM), fluid-structure interaction (FSI), or computational fluid dynamics (CFD) have captured much attention in the past years. However, little focus has been spent on accurately estimating of model parameters and selecting the influential ones [91].

---

[1]The wording *computational model* it is intended, in this document, as any form of analytical or numerical formulation for the solution of engineering problems.
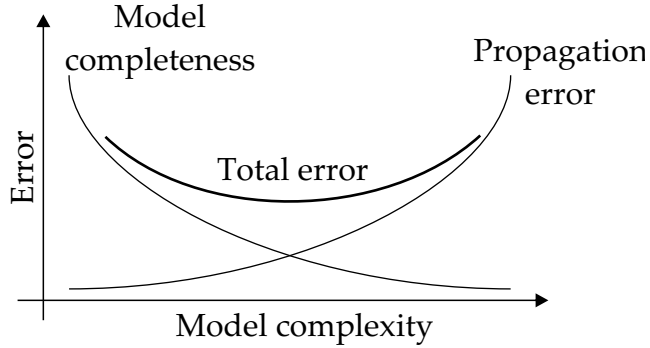
Figure 1.5.: Model error compromise between model completeness and propagation error. The figure has been re-adapted from the work of Razavi et al. [133].

Uncertainty estimation and parameter reduction are valuable and practical tools that must be considered to identify (non)valuable information before and during the modeling phase. For example, uncertainty quantification (UQ) is a well-known method that assesses the model uncertainty given by the model's input variation. UQ is vital in engineering and represents a necessary step in the modeling phase. Besides, sensitivity analysis (SA) focuses on studying how the uncertainty is generated and connected to the model's input variables.

The estimation of a sensitivity measure, as for the Sobol indices, can be an intensive task. The first developed approach consists of a Monte Carlo, or quasi-Monte Carlo, assessment of the indices. However, such techniques are computationally expensive due to the high number of model runs required to reach convergent results [81]. Alternatively, the use of surrogate models has been of great help for sensitivity measures estimation. In particular, the polynomial chaos expansion (PCE) is a valid substitute since the Sobol indices are easily assessed from the expansion coefficients. Therefore, the remaining computational effort is left to calculate a correct PCE.

In a medical engineering context, a recent trend towards patient-specific modeling is visibly becoming more decisive. Therefore, the prediction reliability of computational models is paramount [48]. As a result, SA represents a tool that cannot be neglected when the model is required to be suitable for decision-making. Furthermore, SA eases the process of model personalization. However, its use is restricted in science, particularly in the medical field, by several challenges. The more common challenges are a narrow vision of SA benefits, lack of communication between modelers, analysts, and physicians, or absence of models' uncertainties computation. An explicative work about the challenges of SA and its future in science is provided by Razavi et al. [133].

Applications of SA for the topic of AD are not yet prevailing. Many are found for several CVDs in the field of biomechanics. Quicken et al. [127] apply UQ and SA through a new formulation of adaptive PCE for abdominal aortic aneurysm and arteriovenous fistula. Their application is the closest to this thesis, although their scope was to demonstrate the utility of the new expansion

formulation for treating complex CVD models. Recently, Brandstaeter et al. [32] presented a fascinating analysis on the arterial wall model when subjected to AAA or hypertension. They also use a global SA to demonstrate a possible improvement in clinical measurements, even though it is still prohibitive in collagen growth measurement. Similar conclusions were drawn by Altamirano-Diaz et al. [6] when computing the sensitivity of input parameters for a 0D cardiovascular model affected by hypertension. Recently, Xu et al. [182] stressed the help of SA and surrogate modeling to assess the reliability of in-silico tools for clinical application. An example of how UQ and SA can improve the prediction of a well-known quantity of interest, namely the fractional flow reserve, in coronary stenosis is given by Sturdy et al. [157]. Outstanding work is performed by Eck et al. in [46] and successively in [47]. Initially, a 1D model of the whole cardiovascular system is created, and SA, through a PCE, is computed on two system variables. Successively, the model performance is compared with existing time-series clinical data, and the SA is applied to different model assumptions. In conclusion, they analyzed the reliability of the developed cardiovascular model through SA and model verification and validation.

In the context of AD, several aspects are still unclear and currently in research. Impedance cardiography (ICG) is rapidly emerging in the scientific and medical field, and it appears as a valuable method for AD detection and monitoring [5]. It involves injecting a low-amplitude alternating current into a selected part of the body, e.g., the thorax, from a pair of electrodes. Then, the changes of impedance are detected by measurement sensors in a cardiac cycle. However, different sensor positioning and physiological variations affect the outcome of electrical models predominantly. Furthermore, the theory of the electrical conductivity of flowing blood includes several limitations in the model assumptions. Usually, especially in the engineering field, assumptions are made to simplify the mathematical modeling of systems that are sometimes too complex to be described in their entirety. In the context of electrical conductivity of blood, fluid and flow models have often been highly simplified, e.g., Newtonian fluid or steady-state flow.

Blood clot, medically thrombus, is a coagulation of blood that forms under some particular conditions. When formed and then dislodged, the thrombus can be dangerous or fatal since it may decrease or stop the blood flow in the cardiovascular system [166]. However, the thrombus can be clinically beneficial in AD when it develops in the FL. The blood flow in the FL decreases, the thrombus develops, and if complete thrombosis occurs, the FL could be entirely re-absorbed by the organism. Eventually, the FL will disappear and the diseases with it.

The amount of thrombus in the FL is classified with the status of the FL, namely and ordered by thrombus extension, patent, partial, and complete thrombosed. The most dangerous condition occurs for partial thrombosed FL. Precisely, Tsai et al. [167] computed that this condition can be up to 2.7 times more dangerous than a patent FL due to the occlusion of the distal tear, which leads to FL volume increment and probable aneurysmal dilation or rupture. The latter phenomenon is also known as "blind-sac" FL. However, it is still uncertain whether the patent or partial FL can worsen AD. A complete thrombosis can also be induced by installing a thoracic endovascular aortic repair (TEVAR), which allows the occlusion of the proximal, and eventually, the distal tear, leading to a safe decrease of flow in the FL, and successively thrombosis.

All these uncertainties in understanding the mechanics of systems, particularly computational

models, are given by the lack of connection between computational models and applied medicine. Although this process may require a long ethical approval process, the models' verification, validation, and calibration are critical in research. It is common to analyze a natural phenomenon in minimal detail, thus formulating an accurate duplicate of the studied system. In other words, the spectrum of the analysis focuses and narrows on all the small details that increase model accuracy and complexity. This thesis, on the other hand, intends to broaden the point of view that is usually applied in constructing computational models, e.g., in solid mechanics. This choice is also motivated by the ease with which sensitivity analysis makes it possible to operate.

A very intriguing aspect of SA is the possibility of recreating pathological situations simply by creating an extensive sampling. Each point in the sampling space could be associated with a patient. This approach could be the basis of a new reinforcement to medicine, creating *virtual patients* to simulate different clinical conditions. This new strategy could be innovative given the significant variability that is characteristic of the human being. Each of us has particular and significantly different characteristics than any other individual. Therefore, creating samples that explore this wide human variability could be a starting point for further statistical and engineering studies. Unfortunately, the lack of large databases that can provide information about the probability distribution of specific quantities is always an obstacle in this field. Hypotheses of empirical distributions of system variables may temporarily overcome this challenge, but they are still hypotheses. Therefore, in order to create this technological advance, new data and experiments are preferable.

This thesis seeks to initialize broadening the engineering and medical point of view by laying the groundwork for such a definition of virtual patient, namely by creating and imposing variability in existing mathematical models that address AD-related issues. SA is an excellent tool for analyzing models, such as policy management, decision-making, and even industrial organizations. Therefore, it is believed that the power of SA in the field of medicine, particularly medical engineering, is fundamental and can become an essential cornerstone in the production of effective and transparent medical solutions.

This objective is approached following the example of the general UQ framework proposed by Marelli and Sudret [99]. The proposed approach involves an iteration process that starts from the description of the system through mathematical modeling and the introduction of variability in the input parameters. After analyzing the statistical values of the output produced, UQ, SA, and eventual Bayesian inversion are some of the tools that allow a deep understanding of the mathematical model in use. The procedure is repeated iteratively to reduce the uncertainty of the model as much as possible.

In this text, this framework is taken up, albeit slightly modified. Here, models related to AD are analyzed. At the same time, critical outputs involved in the mechanics of the disease are selected. The modeling process is iterated with the selection of system variables. These variables are selected to best express human variability, and their variation is identified in the available scientific literature and medical expertise. Subsequently, the outputs are analyzed by uncertainty analysis before starting the SA process. This last analysis allows identifying the system variables that do not induce output variation and allows identifying the mechanics of the models, so
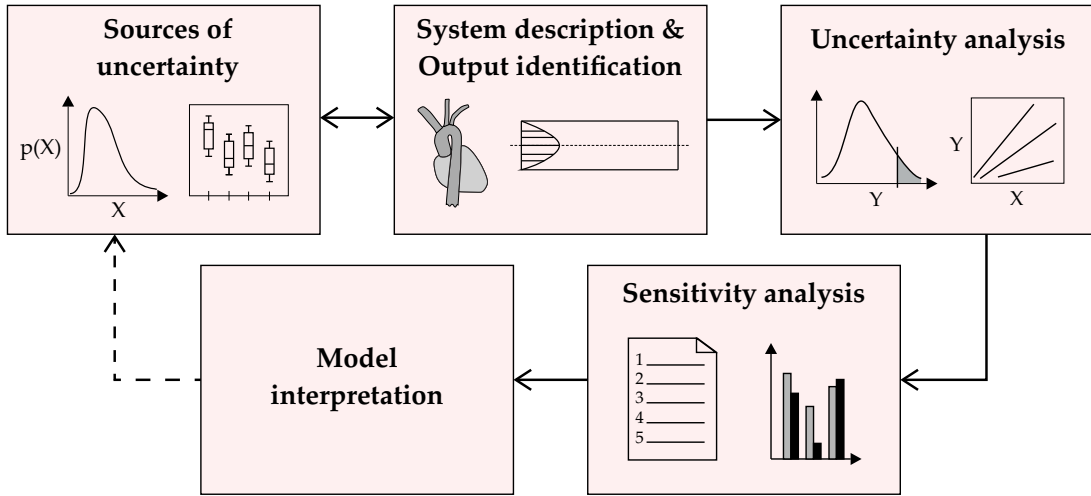
Figure 1.6.: The thesis' framework is here illustrated. First, the modeling and output selection phases iterate on the selection of the sources of uncertainty. Successively, the uncertainty and sensitivity analysis lead to model interpretation. Image inspired by Marelli and Sudret [99].

far obscure. Therefore, the proposed framework differs from Marelli's [99] since it does not deliberately iterate. This iteration is omitted in this text due to the nature of the subject matter. The original approach is very successful in the engineering field. Unfortunately, the situation is more complicated in the medical field as models and hypotheses require clinical validation. This thesis aims to initialize this theoretical process towards a future clinical application. The visualization of the framework of this manuscript is shown in Fig. 1.6.

This thesis is one of the outcomes of the LEAD Project "Mechanics, Modeling and Simulation of Aortic Dissection" at the University of Technology, Graz, Austria. The project aims to improve the understainding of AD description, detection, treatment, mechanics, and processes by looking at different scientific fields and approaches. The project is subdivided into several subprojects. The employment of SA in AD represents one of them. The purpose of this subproject is to glimpse the possibility of understanding the mechanism of AD, and therefore a broadening of views was necessary. The use of SA represents the focus of one of these subprojects and consequently is the cardinal topic of this thesis. The objective of this subproject was to use SA as a tool to better understand some of the dynamics involving AD, so far unexplored. Therefore, it was essential to create an infrastructure capable of analyzing complex computational models produced within the project efficiently and quickly as a requirement for the SA. This requirement is often not feasible due to the high complexity of the models in question, e.g., the case of FSI applications that require complex computational operations and not easy algorithmic solutions.

Consequently, SA has seen great ease of application in problems such as the decoding of mathematical formulations on the theory behind the electrical conductivity of blood, the optimization of sensor positioning in ICG, or the analysis of phenomenological models for the study of thrombus formation. These scientific investigations have been performed and published and

are reported in this manuscript.

However, the product of this subproject is far from complete. There are still many aspects that would require such a mathematical tool, i.e., SA, which will probably be further investigated in later stages of research. Therefore, this thesis aims to set the groundwork for SA in computational models dealing with AD. Here, the benefits and limitations of SA as a tool in biomedicine in analyzed and discussed. The ambition is to set a more common use of SA in this field and promote its use in the promising field of biomedicine, particularly AD. This work is based on the author's publications, listed at the beginning of the document.

1.3. Structure of the thesis

The thesis is divided into three parts. The first covers the motivation of the manuscript, given in this introduction, and the theoretical background needed to comprehend better the next part. The second section includes formulations and examples of sensitivity analysis and surrogate modeling through polynomial chaos expansion.

The second part covers the applications' methods and results that have been produced and published. Chapters 3 and 4 are based on the impedance cardiography (ICG) method, considered a valid candidate for AD detection. An initial analysis of the electrical conductivity of flowing blood, at the basis of the ICG method, is presented in Chapter 3. Here, the analysis focuses on the intrinsic model uncertainties of flow and fluid variables, together with model assumptions such as Newtonian or non-Newtonian formulation of the fluid. Later in Chapter 4, the application of the ICG method is considered. Here, a study is presented on the variation of the signal due to model uncertainties and different electrode positioning on the human thorax. In Chapter 5, the analysis focuses on an AD-related event, i.e., thrombus formation. A phenomenological model of thrombus formation and growth is analyzed, and the model's features are discovered through sensitivity analysis.

The third and last part will cover separately the conclusions produced for each application and, in addition, a more general overview of the role of SA in medical engineering is provided.

2. Fundamentals

The current thesis focuses on applying sensitivity analysis (SA) in several scientific fields, from electrical engineering to fluid dynamics and statistics. In this chapter, the theoretical formulations of these areas are provided in the appendix section. The fundamentals here described have the scope of describing the mechanics of SA to the reader. Initially, a brief introduction about the notation and terminology employed in the chapter is described. Further, starting from the initial idea behind this new scientific field, i.e., SA, its history is illustrated, referring to several available methods. The discussion will lead to the state-of-the-art tools that are used nowadays. In particular, the theory of surrogate modeling through the aid of polynomial chaos expansion (PCE) is primarily illustrated. Examples are also provided to show the difference among several selected methods to motivate the reader to understand the engaging nature of SA.

2.1. Notation and terminology

To enhance readability, the notation and terminology used in this work are introduced. The model g is considered as a mapping function between the inputs and the outputs. The model outputs, also referred to as Quantities of Interest (QoI), are chosen from the modeler and analyst to perform a correct SA study. The dimensionality of input space $\mathcal{X}$ is indicated with M, and the dimensionality of the output space $\mathcal{Y}$ is referred to as B. Thus, the model g is function of a vector $\boldsymbol{x}$ of dimension M, i.e., $\boldsymbol{x} = [x_1, \ldots, x_i, \ldots, x_M] \in \mathcal{X} \subseteq \mathbb{R}^M$, producing an output vector $\boldsymbol{y} = [y_1, \ldots, y_i, \ldots, y_B] \in \mathcal{Y} \subseteq \mathbb{R}^B$. Formulating these definitions, they results in

$$f : \mathcal{X} \to \mathcal{Y} \tag{2.1}$$

$$\boldsymbol{y} = f(\boldsymbol{x}) \ . \tag{2.2}$$

The model is here intended as both an analytical or a numerical problem. The model inputs are referred to as either factors or parameters. A generic input factor is denoted as x_i. To indicate all other factors of $\boldsymbol{x}$ but x_i, the $\sim$ sign is employed with the meaning 'complementary of', e.g., $\boldsymbol{x}_{\sim i} = [x_1, \ldots, x_{i-1}, x_{i+1}, \ldots, x_M]$. However, this sign will be used with this meaning only in subscript, not to be confused with the PDF description of a random variable, $x_i \sim \mathcal{N}(0, 1)$.

When dealing with stochastic, i.e., non-deterministic models, input and output are characterized by a random behavior. Their randomicity is captured and described by a probability density function $p(\bullet)$ (PDF). A random variable could be either continuous, e.g., aortic diameter or blood velocity, or discrete, e.g., age, the roll of a dice. Note that in this work, only the continuous type is taken into account. When a random variable is distributed following a Gaussian distribution, it

2. Fundamentals

can be fully described by the first two moments of $p(\bullet)$, namely the mean or expected value and the variance. Other PDF need more information to be described. However, the other statistical moments are not reported. For a random variable x_i, they are generally defined as

$$\mu_i = \mathbb{E}\left[x_i\right] = \int_{-\infty}^{+\infty} x p(x) \mathrm{d}x \ , \tag{2.3}$$

$$\sigma_i^2 = \mathbb{V}\left[x_i\right] = \int_{-\infty}^{+\infty} \left(x - \mu_i\right)^2 p(x) \mathrm{d}x \ . \tag{2.4}$$

The standard deviation of a PDF $p(x_i)$ is computed through the square root of Eq. 2.4 and referred to as $\sigma_i = \sqrt{\mathbb{V}\left[x_i\right]}$. An example of PDF is given in Fig. 2.1(left), where the random variable x_i is assumed to be Normal, or Gaussian, distributed with zero mean and unit variance $x_i \sim \mathcal{N}(\mu_i, \sigma_i) = \mathcal{N}(0, 1)$. A variable can also be distributed uniformly between a maximum and a minimum value, i.e., $x_i \sim \mathcal{U}(\min(x_i), \max(x_i))$. When not explicitly specified, the PDF refers to a one-dimensional function. In the case of $M > 1$, each system variable may be described by a PDF. If they are mutual independent, the construction of the joint density function $p(\boldsymbol{x}) = \prod_{i=1}^{M} p(x_i)$ is allowed. Note that the information about variable independence is often assumed when not enough data are available to suggest otherwise.

Another way for visualizing the variability of a random variable is with the use of a boxplot. Boxplots are largely employed in descriptive statistics due to their ability to show multiple properties of variation in a single image. An example boxplot use is given in Fig. 2.1, where the PDF of the random variable x_i (on the right) is compared with the new introduced visualization (on the left). The values illustrated in the boxplot percentiles. A percentile is a score at or below which a given percentage ξ of the data is found. A well-known percentile, namely the median, identifies the the score at or below which half of the data distribution is found, i.e., $\xi = 50\%$. The percentiles visible in a boxplot are the minimum ($\xi = 0\%$), the first quartile ($\xi = 25\%$), the median, the third quartile ($\xi = 75\%$), and the maximum ($\xi = 100\%$). The first and the last one are visualized as whiskers, while the others are extremes and the line of the central box.

In statistics, the support of a variable is defined as the set of all the values that the variable can have. It is formally expressed as

$$S_{\mathcal{X}} = \{x_i \in \mathcal{X} \mid p(x_i) > 0\} \ . \tag{2.5}$$

The concept of conditional variance is introduced by Saltelli et al. [145], and it is defined as $\mathbb{V}\left[y|x_i\right]$. It expresses the variance of the variable y given the fixed value of the random variable x_i. Examples can be found in the variance-based SA described in Sect. 2.3.

For a better understanding, an arbitrary model is taken as an example, with which the different SA tools will be applied and explained. The model with dimensionality $M = 3$ is as follows:

$$y = g(\boldsymbol{x}) = c_1 x_1 + c_2 x_2^2 + c_3 x_3 \ , \tag{2.6}$$
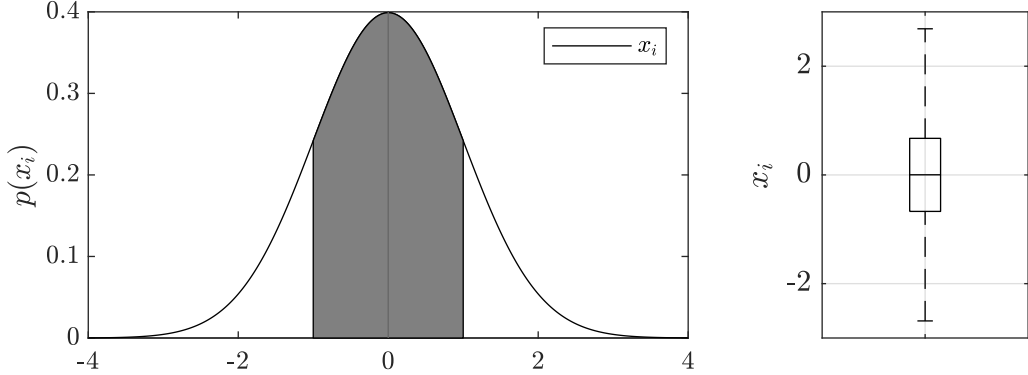
Figure 2.1.: Normal, or Gaussian, probability distribution function with zero mean and variance equal to 1, i.e., $x_i \sim \mathcal{N}(0,1)$. The gray area identifies the standard deviation of the variable x_i. The PDF is represented in its continuous form on the left side, and its boxplot representation is on the right side.

where the output y is a scalar and the coefficients values c_i, together with the probability distributions of the random variables x_i, $i = 1, 2, 3$, are given as

$$c_1 = 1, \quad c_2 = 0.5, \quad c_3 = 0.1 \tag{2.7}$$

$$x_1 \sim \mathcal{N}(1, 0.2) \quad x_2 \sim \mathcal{N}(0, 0.2) \quad x_3 \sim \mathcal{N}(0, 1) . \tag{2.8}$$

Equation (2.6) is computed with a Monte Carlo method by sampling the input space with a Latin Hypercube Sampling technique. The dimension of the sampling space is indicated as N_s.

When dealing with time-dependent variables, two different averaging operators are usually considered: the spatial $\overline{\blacklozenge}$ and the temporal average $\langle \blacklozenge \rangle$. The spatial average will require averaging in the dimension(s) of the system as in

$$\overline{\blacklozenge} = \frac{1}{\Omega} \int_\Omega \blacklozenge(\Omega, t) \mathrm{d}\Omega , \tag{2.9}$$

where Ω is the spatial domain. The temporal average of a field variable $\blacklozenge$, or else cycle-averaged variable, is defined as

$$\langle \blacklozenge \rangle = \frac{1}{T} \int_{nT}^{(n+1)T} \blacklozenge(\Omega, t) \mathrm{d}t \quad n \in \mathbb{N} , \tag{2.10}$$

where T is the period of the cardiac cycle and n the cycle counter. The time derivative of a field is visualized as $\dot{\blacklozenge}$. In the next sections, the use of surrogate models is described and employed. To distinguish between the computational model and the computed surrogate, the use of the symbol $\widetilde{\blacklozenge}$ is employed. Complex quantities are denoted as $\underline{\bullet}$, and for periodic quantities, the symbol $\hat{\blacklozenge}$ is employed to denote the peak-to-peak amplitude.

2.2. Sensitivity analysis

This section is based on the work published by Melito et al. [105], and mainly inspired by Borgonovo and Plischke [31], Razavi et al. [133], and Saltelli et al. [145].

SA is a relatively recent field of study that sees its origin from the known design of experiments (DOE) method. While DOE is directed at analyzing the effect of one or more variables in the context of laboratory experiments, SA originates with the progression of computational power in the field of engineering. SA is used to extract the information, rooted into computational models, about how much the uncertainty in the input factors affects the model output(s). Several methods are used to rank the most influential variables on a QoI and assess their interaction level [81, 82].

SA is classified as local when it focuses on the impact of one input random variable in its vicinity for a small perturbation. In other words, one input parameter at a time is varied while the others are kept fixed [142]. Some local SA examples are finite-difference computation [31], differential importance measure [29], elasticity measure [30], screening methods [31, 115].

Alternatively, the SA is global when multiple parameters are varied simultaneously, and the analysis is performed over the whole input space. Global SA quantifies the uncertainty of the QoI by looking at the uncertainty in all input parameters and their combination. It is also a powerful tool when used in calibrating the model to reproduce a physical process. Global SA is based on the assumption that the model inputs' probability distribution, joint or marginal, is provided [140]. Specifically, in a global setting, it is possible to assign a probabilistic distribution to the model's input factors, unlike the local method. The use of SA in the thesis is always referred to as the global method. Therefore a description of local SA is omitted here. However, for completeness, a good overview of the local method is provided in Borgonovo and Plischke [31]. Since local SA is never employed in this work, the author will refer simply to SA to express a global method.

A well-known and basic example of global SA use is to analyze the distribution of the points in a scatter plot where the input(s) are plotted against the output(s) data points. In this approach, the solution of the model is performed with a Monte Carlo method. Therefore it can result unpractical for a complex system. Considering the example given in Eq. (2.6), the scatter plot of $N_s = 1000$ samples is given in Fig. 2.2. The first element to notice is the way the points are distributed. The variable x_1 has more influence on the output y than variable x_2. Indeed, the correlation between input and output is linear and positively correlated for x_1, while the plot of x_2 highlights an ambiguous behavior in the model. Finally, the third variable, x_3, also shows some positive correlation with the output, but not as strong as the first variable.

Different other methods of SA have been developed. Their classification does not result in being uniform in literature. However, following the classification provided by Razavi et al. [133], SA may be categorized in four main approaches: derivative-based, distribution-based, variogram-based, and regression-based. The groups are described as follows:

- **derivative-based** approach is the simplest form of SA. Its core method is similar to a local SA, where input perturbations are imposed. Given an input base-point, a perturbation
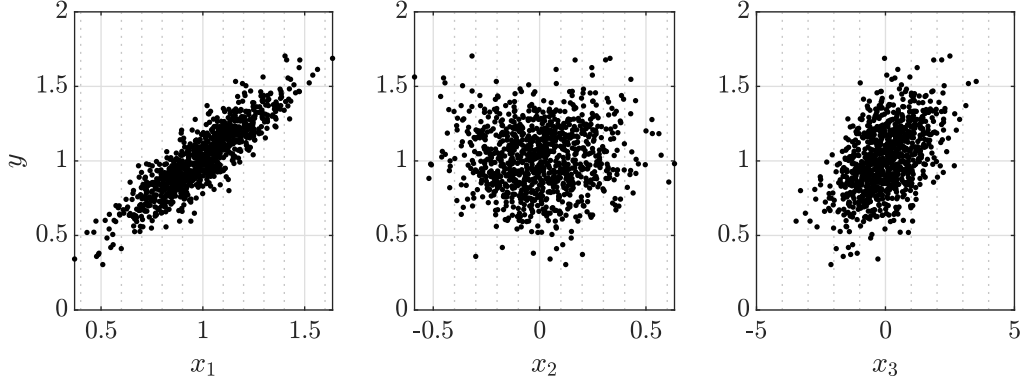
Figure 2.2.: Scatter plot of input versus output of the arbitrary model of dimensionality $M = 3$.

strategy, and a sampling method, the output variation is detected through derivatives, computed analytically or numerically. Derivatives are commonly considered as local sensitivity measures. However, they are averaged over the whole input space in this approach. Some examples are developed by Campolongo et al. [34], Sobol and Kucherenko [151], or Morris [115]. The latter is primarily used to detect the first sign of parameter sensitiveness in the case of many input variables.

- **distribution-based** approach bases the analysis on the probabilistic distribution of the model output. The variance-based approach, density-based approach, and regional sensitivity analysis (RSA) are the most known methods.

- **variogram-based** approach is the youngest category in SA [131, 132]. Variogram-based aims to identify a spatially-ordered structure that connects the input space to the output space.

- **regression-based** approach collects the information about the sensitiveness of model parameters from the coefficient of model regression. This widely used approach has also been disapproved due to prior assumptions on the model behavior, such as linearity or monotonicity. However, with the recent development of machine learning techniques, this method provides a new sensitivity measure called 'variable importance.'

A particular method that is controversially classified is the Elementary Effect (EE) method [115]. Although it is mainly a local SA, since it is based on the analysis of small input perturbations, it may be considered a global derivative-based method due to its ability to overcome many local methods' limitations. EE also belongs to the Once At Time (OAT) techniques, the tools that analyze models whose computations are given by a single factor input variation at a time. Given its low computational cost, it can efficiently analyze a high-dimensional input space, and it is easy to implement in any computational model. The algorithm imposes a p_{EE}-level discretization of the M-dimensional input space, with p_{EE} being an even number. The distance between two sample points in the grid is given by $\Delta_{EE} = p_{EE}/(2p - 2)$. Then, a starting point is chosen randomly in the p_{EE}-level grid, and N_{EE} trajectories are drawn so that each one will cover each dimension of the input space, see Fig. 2.3. The elementary effect for each input variable x_i on
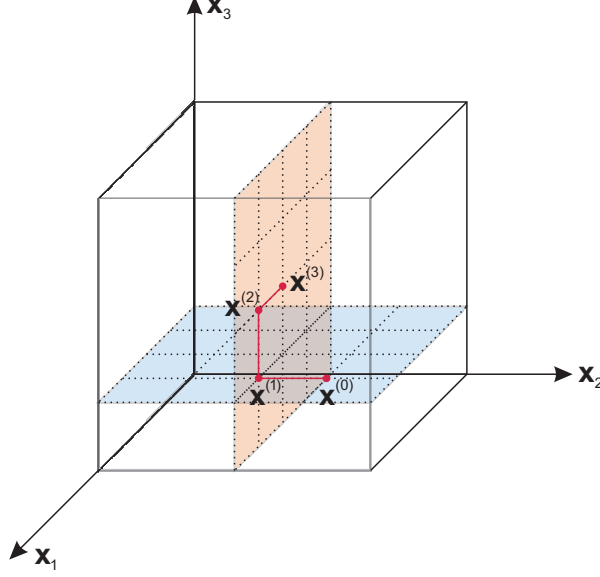
Figure 2.3.: Representation of the grid levels and trajectory techniques of the Elementary Effect method for a three dimensional problem ($M = 3$). Figure interpreted and redapted from Saltelli et al. [145].

the output y is EE_i, which is formulated as [115]

$$EE_i = \frac{y(x_1, \ldots, x_i + \Delta_{\mathrm{EE}}, \ldots, x_M)}{\Delta_{\mathrm{EE}}} \ . \tag{2.11}$$

The input perturbation is repeated for N_{EE} trajectories and the employed sensitivity measure is the sample mean $\check{\mu}_i$ and its standard deviation $\check{\sigma}_i$ as [115]

$$\check{\mu}_i = \frac{1}{N_{\mathrm{EE}}} \sum_{\tau_{\mathrm{EE}}=1}^{N_{\mathrm{EE}}} EE_i(\tau_{\mathrm{EE}}) \tag{2.12a}$$

$$\check{\sigma}_i = \frac{1}{N_{\mathrm{EE}} - 1} \sum_{\tau_{\mathrm{EE}}=1}^{N_{\mathrm{EE}}} \sqrt{(EE_i(\tau_{\mathrm{EE}}) - \mu_i)^2} \ . \tag{2.12b}$$

The two mentioned indices are not to be confused with the mean and variance of a variable x_i, as referred to in Eq.s (2.3) and (2.4). Their notation is intentionally left similar since their formulation is equivalent. However, the last two sensitivity indices are to be connected with the EE method only.

When the index $\check{\mu}_i$ is equal to zero, see Eq. (2.12a), a model factor can be either influential or not on the output. Suppose that $\check{\mu}_i = 0$, but the EE_i standard deviation $\check{\sigma}_i$ is large. In this case, the variable leads to both negative and positive EE_i effects due to interactions or nonlinearities that cancel each other. To overcome this phenomenon, another measure has been introduced by
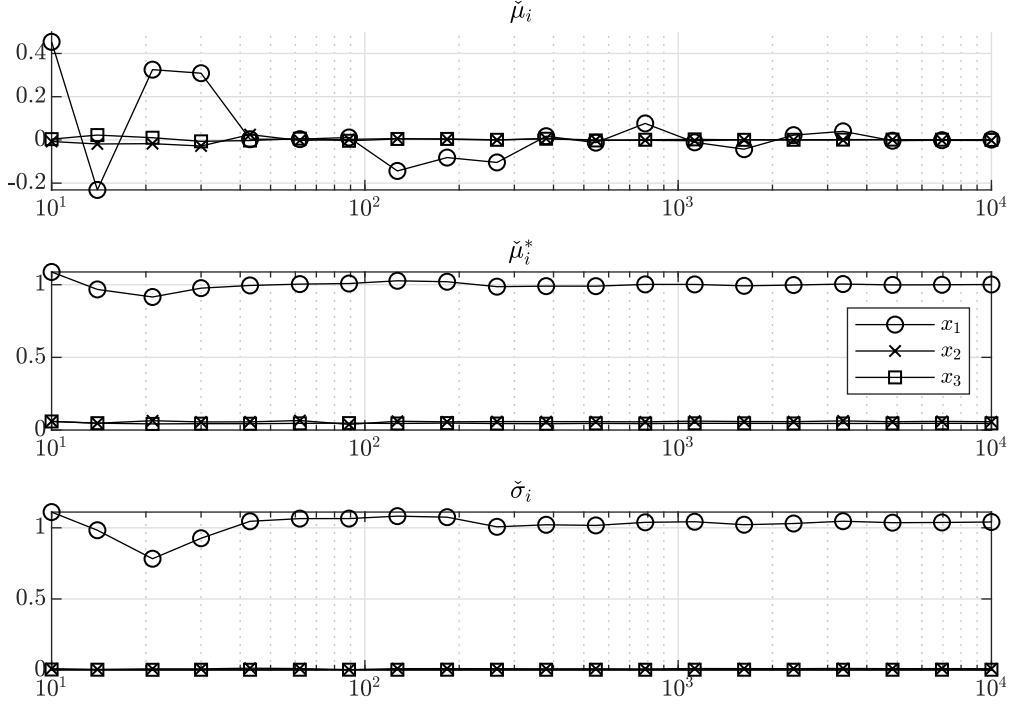
Figure 2.4.: Convergence of the EE sensitivity indices for different numbers of trajectories.

Campolongo et al. [34]

$$\check{\mu}_i^* = \frac{1}{N_{\text{EE}}} \sum_{\tau_{\text{EE}}=1}^{N_{\text{EE}}} |EE_i(\tau_{\text{EE}})| \; , \tag{2.13}$$

s.t. those effects are taken into account. In their work, Campolongo et al. [34] claim that $\check{\mu}_i^*$ is a valuable substitute for the Sobol indices, which will be discussed later. However, to reach that, many trajectories are needed, making the method computationally expensive for complex systems. As an example, the example model in Eq. (2.6) is employed for this particular method. As visible in Fig. 2.4, for an easy model, the convergence of the results is reached at $N_{\text{EE}} = 10^4$. An interesting excursus on this method has been published by Saltelli et al. [145], where a helpful strategy optimization is introduced to produce the needed number of trajectories N_{EE}.

In the regression-based approach, also classified as a non-parametric method [31], many sensitivity measures have been defined. They are largely used because of the possibility of using a Monte Carlo method for their computation. Therefore the computational cost is equal to the selected sample size. Consider N_s to be the sample size. Suppose that the input-output relationship follows a linear regression as

$$y = g(\boldsymbol{x}) \approx b_0 + \sum_{i=1}^{M} b_i x_i \; . \tag{2.14}$$

2. Fundamentals

where b_0 is the y-axis intercept and b_i are the variables slope coefficients. The standard regression coefficient (SRC), which enhances direct comparison without units, is defined as [72, 90]

$$\text{SRC}_i = b_i \frac{\sigma_i}{\sigma_y}, \qquad (2.15)$$

where the numerator is the standard deviation of the input model x_i, and the denominator is the standard deviation of the model output y. A second well-known coefficient is expressed by the Pearson's product moment correlation coefficient:

$$\varrho_i = \varrho(y, x_i) = \frac{\text{cov}(y, x_i)}{\sigma_i \sigma_y} \qquad (2.16)$$

where the numerator is $\text{cov}(y, x_i) = \sum_{j=1}^{N_s} (x_{ij} - \mu_i)(y_j - \mu_y)$, and $\text{cov}(\bullet)$ is the covariance operator.

Before computing the sensitivity coefficients, the goodness-of-fit coefficient, also known as the coefficient of determination, R^2 has to be considered. It is defined to include the square of the residuals between the data point and the regression line and it ranges from 0 to 1. The latter indicates a perfect regression match to the model data. A poor fit leads to an insufficient regression, thus an inaccurate sensitivity quantification. As a good practice, the model regression is considered inappropriate when $R^2 < 0.5$. Hence, the use of a regression-based approach is discouraged when model linearity is unknown [33].

Consider again the problem example illustrated in Eq. (2.6). Linear regression is imposed and shown in Fig. 2.5. As visible, the regression is very accurate for x_1, worse for x_3, but not acceptable for x_2. Such a conclusion could also be drawn by looking at the model formulation in Eq. (2.6). The second variable has a non-linear influence on the output and, therefore, cannot be represented by linear regression. The goodness-of-fit coefficient R^2 reported in Tab. 2.1 confirms such results. It has to be mentioned that the model formulation is explicit and known in this particular example. However, an explicit formulation is often rare in many engineering applications, and assumptions on model behavior are necessary.

Looking at the results in Tab. 2.1, an unintelligible difference among the sensitivity methods is visible. Although much confusion regarding the two coefficients is diffuse, they tend to equalize when the variables are independent. Their accuracy is dependent on the available number of sample points, which is a matter of model complexity. However, they fail to represent the influence of all the system variables, especially for what concerns x_2, given its non-linearity. To better understand model linearity, one can analyze the value of the goodness-of-fit R^2: if the coefficient values, say, 0.7, then the model is 70% linear, and the regression-based coefficients should be used carefully. Therefore, the model has a linear behavior only for x_1, but not in the remaining two dimensions.

The variance-based method is one of the density-based approaches. The analysis is based on the expected reduction in model output variance given the certainty of the model input factors. This method is built upon the ANOVA output variance decomposition (ANalysis Of VAriance), unique for independent input random variables [50, 119, 128]. From the variance decomposition, sensitivity measures can be developed [148].

20
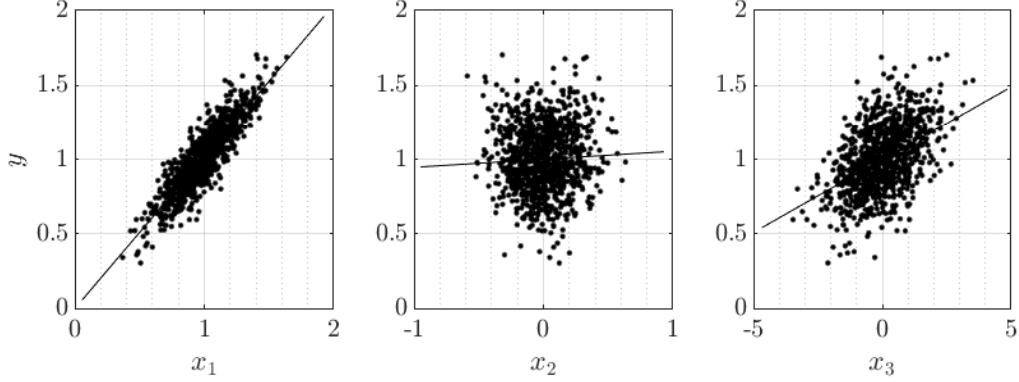
Figure 2.5.: Scatter plots of the 3 model variables and linear regression model for each of them.

Table 2.1.: Linear regression coefficients (b_i) and regression-based results (SRC_i, ϱ_i) of the example model are reported. In addition, the goodness-of-fit coefficient R^2 to the linear model is reported in column 3.

	b_i	R^2	SRC_i	ϱ_i
x_1	1.018	0.787	0.904	0.887
x_2	0.053	0.004	0.000	0.000
x_3	0.098	0.196	0.442	0.443

Initially, the indices were uniquely computed using the Monte Carlo method. Here, a deterministic model is evaluated for a large sample collected from the input space of the model, and finally, the conditional expectations expressed in Xiu and Karniadakis [180] and Ghanem and Spanos [66] are computed. This method becomes onerous and troublesome for computationally demanding models, e.g., FEM or fluid-structure interaction models. Recently, Sudret [158] introduced the Sobol indices' computation from the polynomial chaos expansion coefficient, which was previously used mainly in the stochastic finite element method. The current thesis uses the variance-based method and the polynomial chaos expansion as surrogate models and tools. Their description is given in the following sections.

Another standard SA method is the density-based approach. Contrary to the most common variance-based method, it considers the entire probability distribution of the quantity of interest; thus, it does not focus the analysis on one particular distribution moment, i.e., the variance [28, 122].

The advance of computational power has also promoted the diffusion of SA in many scientific fields. New software tools and toolboxes have been developed and are now available. Some examples include Dakota [1] in C++, SobolGSA [92] in C#, MATLAB and Python, the 'sensitivity' package [80] in R, and SAFE [123] in MATLAB, R, and Python. In the current work, the toolbox UQlab

developed by Marelli and Sudret [99] in MATLAB is used to compute the PCE formulations.

2.3. Variance-based approach

One of the most used techniques in SA is the variance-based method. Here, the output variance is apportioned in the sum of the contributions of each random variable. The mechanics of the variance-based method are initiated with the Sobol decomposition of the model [148]. Consider a mathematical model g as a function of an input random vector $\boldsymbol{x}$ of dimension M. In addition to the definition of Eq. (2.2), the input space is here defined in the unit cube $K^M = \{\boldsymbol{x} \mid 0 \leqslant x_i \leqslant 1\}$. The sum over all the combination of indices in K^M, without repetition, is $\sum T_{i_1,\ldots,i_s}$ and defined as [77]

$$\sum T_{i_1,\ldots,i_s} \equiv \sum_i^M T_i + \sum_{1 \leqslant i < j \leqslant M} T_{ij} + \ldots + T_{1,\ldots,M} \, , \tag{2.17}$$

where the indices are ordered as $1 \leqslant i_1 < \ldots < i_s \leqslant M$, and $s = 1,\ldots,M$. The indices belong to $\mathcal{S}$, which is the set of indices composed by all combination that include x_i, $\mathcal{S} = \{(i_1,\ldots,i_s) \mid \exists q, 1 \leqslant q \leqslant s \wedge i_q = i\}$ [77]. For example, for $M = 3$, the sum over all the combinations of indices is $\sum T_{i_1,\ldots,i_s} = 3 + 3 + 1 = 7$, since the number of summands follows the binomial coefficient

$$\sum_{i=1}^M \binom{M}{i} = 2^M - 1, \quad 1 \leqslant i \leqslant s \leqslant M \, . \tag{2.18}$$

The Sobol decomposition of the model $g(\boldsymbol{x})$ reads [148]

$$\begin{aligned}
g(x_1,\ldots,x_M) =& g_0 + \sum g_{i_1,\ldots,i_s}(x_{i_1},\ldots,x_{i_s}) = \\
& g_0 + \\
& + \sum_{i=1}^M g_i(x_i) + \ldots \\
& + \sum_{1 \leqslant i < i' \leqslant M} g_{ii'}(x_i, x_{i'}) + \ldots \\
& + g_{1,\ldots,M}(x_1,\ldots,x_M) \, ,
\end{aligned} \tag{2.19}$$

where g_0 is a constant and represents the average value of the model response

$$\mathbb{E}\left[y\right] = g_0 = \int_{K^M} g(\boldsymbol{x}) \mathrm{d}\boldsymbol{x} = \text{constant} \, . \tag{2.20}$$

Furthermore, the integral of each element of Eq. (2.19) over any of its independent variable is null Sudret [158],

$$\int_{K^M} g_{i_1,\ldots,i_s}(x_{i_1},\ldots,x_{i_s}) \mathrm{d}x_{i_k} = 0 \, , \quad 1 \leqslant k \leqslant s \, . \tag{2.21}$$

The uniqueness of the decomposition is granted by the orthogonality property of the model decomposition of the summands in Eq. (2.19) as

$$\int_{K^M} g_{i_1,\dots,i_s}(x_{i_1},\dots,x_{i_s})g_{i_1,\dots,i_t}(x_{i_1},\dots,x_{i_t})\mathrm{d}\boldsymbol{x} = 0 \; , \tag{2.22}$$

due to the definition of Eq. (2.21). Each term of (2.19) is expressed as constant (2.23a), univariate- (2.23b), bivariate- (2.23c), and multivariate-terms for more than two terms [77]

$$g_0 = \mathbb{E}\left[y\right] \tag{2.23a}$$

$$g_i = \mathbb{E}\left[y|x_i\right] - \mathbb{E}\left[y\right] \tag{2.23b}$$

$$g_{ii'} = \mathbb{E}\left[y|x_i,x_{i'}\right] - g_i - g_{i'} - \mathbb{E}\left[y\right] \; . \tag{2.23c}$$

After decomposing the model as in Eq. (2.19), quantitative statistical measures can be defined. The model variance is derived, by using Eq.s (2.20) and (2.23a), as

$$\sigma_y^2 = \mathbb{V}\left[g(\boldsymbol{x})\right] = \mathbb{E}\left[g^2(\boldsymbol{x})\right] - \mathbb{E}\left[g(\boldsymbol{x})\right]^2 = \int_{K^M} g^2(\boldsymbol{x})\mathrm{d}\boldsymbol{x} - g_0^2\mathrm{d}\boldsymbol{x} \; . \tag{2.24}$$

To decompose the model variance, the integral of the square of Eq. (2.19) is computed. Using the orthogonality property defined in Eq. (2.22), the variance can be decomposed as

$$\sigma_y^2 = \sum_{i=1}^{M} \sigma_i^2 + \sum_{1\leqslant i<i'\leqslant M} \sigma_{ii'}^2 + \dots + \sigma_{1,\dots,M}^2 \; , \tag{2.25}$$

where the σ_i^2 term identifies the partial variance imposed by the variable x_i, $\sigma_{ii'}^2$ the partial variance imposed by both variables x_i and $x_{i'}$. Else, in a more general formulation [77]

$$\sigma_{i_1,\dots,i_s}^2 = \int_{K^S} g_{i_1,\dots,i_s}^2(x_{i_1},\dots,x_{i_s})\mathrm{d}x_{i_1},\dots,x_{i_s} \; . \tag{2.26}$$

At this point, the computation of the sensitivity indices is made possible in a variance-based fashion. The first sensitivity measure is defined by computing the ratio between the partial and the total output variance as in [77]

$$S_{i_1,\dots,i_s} = \frac{\sigma_{i_1,\dots,i_s}^2}{\sigma_y^2} \; . \tag{2.27}$$

As expected, they quantify the amount of output variance that is produced given the uncertainty in the set of input factors $i_1,\dots,i_s$. Although, the number of computable sensitivity indices is $2^M - 1$, it is demonstrated that the first and total-order indices are enough to describe the system's overall sensitivity sufficiently [145]. Using the formulation expressed above, they are defined as first-order Sobol index

$$S_i = \frac{\sigma_i^2}{\sigma_y^2} \; , \tag{2.28}$$

and total-order Sobol index

$$S_i^{\mathrm{T}} = \sum_{\mathcal{S}} \frac{\sigma_{i_1,\dots,i_s}^2}{\sigma_y^2} \ . \tag{2.29}$$

Given the variance decomposition in partial variances and the uniqueness and orthogonality of the decomposition, it is demonstrable that the sum of all sensitivity indices equals 1. Consequently, an alternative formulation of the total-order index is $S_i^{\mathrm{T}} = 1 - S_{\sim i}$, in which $S_{\sim i}$ indicates all the indices that do not contain x_i [145].

The description of the Sobol indices can also have a less abstract description. Consider a scatter plot where the input data is plotted against the model output. Imagine dividing the input domain into a set of small slices, thin the slices as much as possible, and inspect the output data variation along the y-axis. This variation is also described as $\mathbb{V}\left[\mathbb{E}\left[y|x_i\right]\right]$, which expresses the variation of the expected value of y when the variable x_i is considered fixed in value. Consequently, the first-order sensitivity index S_i, see Eq. (2.28) [149, 150], can be derived not only by the ratio of the partial variance σ_i^2 and the model's total variance. By definition, it is also expressed as

$$S_i = \frac{\mathbb{V}\left[\mathbb{E}\left[y|x_i\right]\right]}{\mathbb{V}\left[y\right]} \ , \tag{2.30}$$

which represents the contribution of the random variable x_i to the change of the model output y, without considering the effect of its interaction with other input variables. Therefore, a random variable x_i is considered influential (non-influential) to the model output if the conditional variance $\mathbb{V}\left[\mathbb{E}\left[y|x_i\right]\right]$ is large (small) enough to the variance of the QoI. The first-order index identifies the level of influence of the single parameter on the output in the sensitivity analysis. It allows the use of the *Factor Prioritization* setting, which identifies the input factors that contain the most influence on the QoI, i.e., which one is the most responsible for the production of the model variation [145].

The total-order sensitivity index S_i^{T}, see Eq. (2.29), evaluates the total effect of an input variable. The conditional probability is then computed over the whole input space except the i-th random variable. This is described as $\boldsymbol{x}_{\sim i}$ and leads to the evaluation of Eq. (2.29) as [145]

$$S_i^{\mathrm{T}} = 1 - \frac{\mathbb{V}\left[\mathbb{E}\left[y|\boldsymbol{x}_{\sim i}\right]\right]}{\mathbb{V}\left[y\right]} = \frac{\mathbb{E}\left[\mathbb{V}\left[y|\boldsymbol{x}_{\sim i}\right]\right]}{\mathbb{V}\left[y\right]} \ . \tag{2.31}$$

The total-order sensitivity index shows the degree of the influence of the input random variable on the QoI together with the interactions with other input factors. The total-order index is used to produce the *Factor Fixing* setting. Here, the lower values of the total-order index are analyzed to decide which variable has no effect or low effect on the output, considering its collaborations. Consequently, they can be considered model constants, and the model output will not be affected by their change.

Together with the first- and total-order sensitivity indices, it is possible to compute the interaction terms for several degrees of interaction. However, the first and total indices together
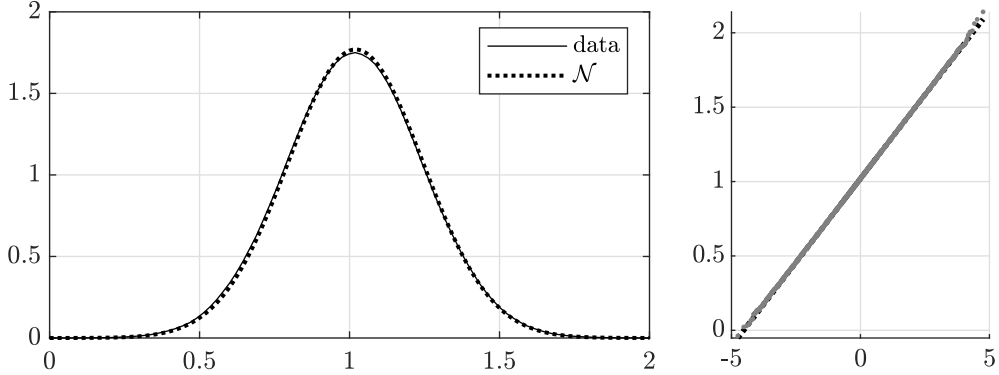
Figure 2.6.: Output probability distribution function. (left) comparison of the output data PDF and normal PDF, and (right) QQplot of the two distributions, where the dotted line represents the normal distribution and the data are plotted in gray dots.

express the influence relationship of the input domain on the QoI sufficiently and avoid the need of computing high-order sensitivity indices, which may be computationally expensive [140]. An intriguing feature of the first-order index is that it can identify the model's additivity by summing up all the first-order indices and checking if their sum is equal to one. Such a condition expresses that all the output variation is given only by the single input factors and that no interaction exists.

The model expressed in Eq. (2.6) can also be analyzed with the variance-based method. The method requires having an output PDF that can be described by the variance. Indeed, using a variance-based method is inaccurate in the case of multi-modal probability distributions. In Fig. 2.6 a QQplot test is performed to check if the model output follows a normal distribution. The test results are positive, therefore the model variance can be decomposed, and Sobol indices applied. Other tests are available to verify if empirical distributions can be described with a normal PDF. However, given the qualitative success produced by the QQplot, they are not considered hereafter.

The computation of the Sobol indices with a Monte Carlo technique has been widely improved over the years from the initial work of Homma and Saltelli [77]. Saltelli [140] introduced an algorithm for the computation of first and total-order Sobol indices with a Monte Carlo sampling, which is used in this text. The drawback of this technique is the computational burden needed to reach a result convergence. Further on, Saltelli et al. in [145] and later in [146] introduced an innovative approximation technique that additionally reduced the computation cost of the indices. For the indices computation, several runs of the model are needed, and the convergence of the indices is visible in Fig. 2.8. Even for an easy model as in Eq. (2.6), $N_s = 10^8$ simulations are needed to reach an accurate result. The computed indices and their standard deviation over 10 bootstrap evaluations are reported in Tab. 2.2. From the results, and because $\sum_i S_i = 1$, it is clear that the model is additive in the sense that no interaction is present among the input variables. An example of a nonadditive model can be made by transforming the model in Eq. (2.6) from $y = \sum_i c_i x_i{}^d$ to $y = \prod_i c_i x_i{}^d$, $\forall d \in \mathbb{Z}_0$.

Table 2.2.: Variance-based sensitivity analysis results of the example model. Final results of the Sobol indices in the first two columns and their standard deviation over ten bootstraps.

	S_i	S_i^{T}	$\sigma(S_i)$	$\sigma(S_i^{\mathrm{T}})$
x_1	0.7877	0.7871	0.0005	0.0012
x_2	0.0159	0.0151	0.0009	0.0019
x_3	0.1964	0.1967	0.0007	0.0017
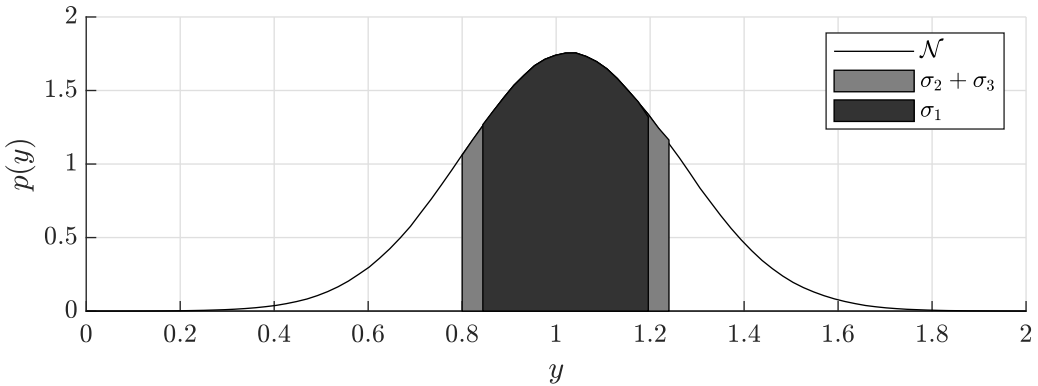
Figure 2.7.: Variance decomposition of the output distribution of the example model. The areas indicate the variation imposed by the input factors' uncertainties. The areas are the standard deviation imposed by x_2 and x_3 ($\sigma_2 + \sigma_3$), and x_1 (σ_1).

At this point of the analysis, it is clear that the model has a non-linear additive behavior. The input factor x_1 is the most important in the model since it drives the most uncertainty in the output, i.e., 78 % of the variation. Imagine that the model represents an experimental setup and that its formulation is known as in Eq. (2.6). Applying the Factor Prioritization setting suggests that x_1 is the primary source of uncertainty, and therefore its measurements require significant attention. On the other hand, with the use of Factor Fixing, it is possible to infer that the factor x_2 does not affect the output variation and, therefore, it could be considered a model constant.

The standard deviation of the example model is highlighted and then decomposed in Fig. 2.7 to better visualize the variance decomposition of this method. The three areas denote the influence imposed by the variation of the input parameters, and they are indicated as σ_i, for $i = 1, 2, 3$. The area of σ_2 is hardly detectable due to the low influence of x_2 in the model. The dominance of x_1 on the output variation is, however, evident.

The presented results are a clear example of the power of a variance-based sensitivity analysis. However, the Monte Carlo approach is expensive and tedious. In the shown example, only three sources of uncertainties are chosen. Nevertheless, the variable's coefficient c_i can also include uncertainty, leading to higher complexity of the model, a nonadditivity behavior, and the need for a larger input sample to create computational convergence. These are only some of the reasons
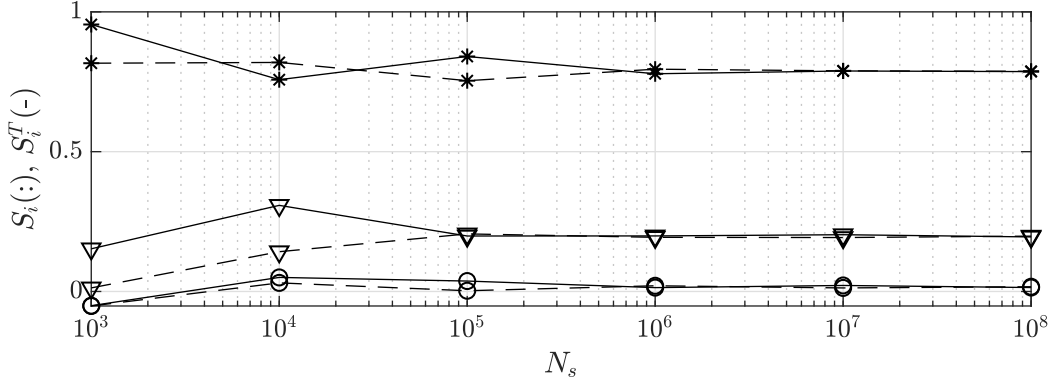
Figure 2.8.: First- and total-order Sobol indices computation with Monte Carlo sampling technique. The markers indicate ($*$) x_1, ($\circ$) x_2, and ($\bigtriangledown$) x_3. The dashed line refers to first-order index and the continuous line refers to the total-order index.

that brought to the use of a surrogate model to compute the Sobol indices, namely the PCE.

2.4. Polynomial Chaos Expansion

The polynomial chaos expansion aims at representing random fields in a polynomial expansion based on orthogonal polynomials of probability measures, i.e., the input random space [180]. The PCE was introduced by Wiener [174] in the pioneer study on Gaussian stochastic processes. It was first developed to use only Hermite polynomials, and the word *chaos* comes from the variability induced by the normal distribution of the variables. Later, it was implemented in the engineering world by Ghanem and Spanos [66], but the expansion could still represent processes driven only by Gaussian variables. Hence the use of Hermite polynomials made its characteristic name: *homogeneous chaos*. This limitation has restricted the use of the expansion in non-Gaussian applications. Lately, Xiu and Karniadakis [181] introduced the use of other polynomials, of which Laguerre and Jacobi polynomials are some examples. From here, the expansion takes the name *generalized* PCE. However, the author will refer to PCE in the text, considering the latter and generalized formulation. To sum it up, PCE can be seen as a spectral representation of the solution domain when it is affected by fluctuations given by randomicity.

For the definition of the PCE, the introduction and definition of orthogonal polynomials are necessary. The formulation used in the following has been inspired by Xiu [179].

One-dimensional formulation   A general polynomial formulation in the variable $x \in \mathcal{X}$ has the form

$$P_d(x) = c_d x^d + c_{d-1} x^{d-1} + \ldots + c_1 x + c_0 = \sum_{h=0}^{d} c_h x^h \ . \tag{2.32}$$

2. Fundamentals

The degree of the polynomial is d, and c_h are the polynomial coefficients. Consider $\{P_d(x), d \in \mathbb{Z}_0\}$ to be a system of polynomials, where $\mathbb{Z}_0 = \{0, 1, 2, \ldots\}$ is the set of nonnegative integers. The system is defined to be orthogonal when [179]

$$\int_{S_\mathcal{X}} P_q(x) P_d(x) p(x) \mathrm{d}x = \gamma_d \delta_{qd} \ , \tag{2.33}$$

for any $q, d \in \mathbb{Z}_0$, and $p(x)$ is a continuous PDF. The Kronecker delta δ_{qd} is null when $q \neq d$, equal to one otherwise, and $S_\mathcal{X}$ is the support of the variable x. The term γ_d is referred as normalization constant and it is defined as

$$\gamma_d = \int_{S_\mathcal{X}} P_d^2(x) p(x) \mathrm{d}x \ . \tag{2.34}$$

Orthogonal polynomials have the possibility to be described by following the Askey scheme [8, 9], which uses a hypergeometric series formulation. Thus, defining the falling factorial Pochhammer symbol $(c)_d$ as [125]

$$(c)_d = \begin{cases} c & d = 0 \\ c(c+1)\ldots(c+d-1) & d \in \mathbb{N} \ , \end{cases} \tag{2.35}$$

the hypergeometric series representation $_rP_s$ of an orthogonal polynomial of degree d is given by

$$_rP_s(c_1, \ldots, c_r; c_1', \ldots, c_s'; x) = \sum_{h=0}^{d} \frac{(c_1)_h \ldots (c_r)_h}{(c_1')_h \ldots (c_s')_h} \frac{x^h}{h!} \tag{2.36}$$

for $r, s \in \mathbb{Z}_0$ being the number of polynomial coefficients in the numerator and denominator, respectively, and $c_j' \in \mathbb{N}$ for $j = 1, 2, \ldots, s$.

Given the definition of orthogonal polynomials, the next step consists of defining the PCE's basis for a probability density function of a generic random variable x. Assuming that x follows a continuous PDF $p(x)$, e.g., uniform distribution, and has finite moments as in [179]

$$\mathbb{E}\left[|x|^{2r}\right] = \int |x|^{2r} p(x) \mathrm{d}x < \infty \quad r \in \mathbb{Z}_0 \ . \tag{2.37}$$

The formulation of an orthogonal basis, as in Eq. (2.33) and by using Eq. (2.3), is given as

$$\mathbb{E}\left[\phi_q(x)\phi_d(x)\right] = \gamma_d \delta_{qd} \ , \tag{2.38}$$

where ϕ_q and ϕ_d are two generic functions of degrees q and d, respectively. The previous equation can be rewritten as

$$\mathbb{E}\left[\phi_q(x)\phi_d(x)\right] = \int \phi_q(x)\phi_d(x) p(x) \mathrm{d}x \ . \tag{2.39}$$

The set of polynomials $\{\phi_d(x)\}$ is orthogonal to the weight function p; therefore, the polynomials are chosen to be orthogonal to the PDF of the variable. Naturally, the construction of orthogonal

2.4. Polynomial Chaos Expansion

Table 2.3.: Some example of hypergeometric represention of known orthogonals polynomials to continuous random variable.

Notation	Expansion	$p(x)$	Distribution
Legendre	$L_0(x) = 1$	$\frac{1}{2}$	Uniform
$_2P_1(-d, d+1; 1; \frac{1-x}{2})$	$L_1(x) = x$		
	$L_2(x) = \frac{3}{2}x^2 - \frac{1}{2}$		
	$\ldots$		
Hermite	$H_0(x) = 1$	$\frac{1}{\sqrt{2\pi}}e^{-x^2/2}$	Normal
$(\sqrt{2}x)^d \; _2P_0(-\frac{d}{d}, -\frac{d-1}{2}; 0; -\frac{2}{x^2})$	$H_1(x) = x$		
	$H_2(x) = x^2 - 1$		
	$\ldots$		

polynomials to the variable's density functions is not limited to only continuous variables. However, their formulation is not needed here (see [179]). Some examples of PCE basis polynomials for normal and uniform random variables are illustrated in Tab. 2.3.

Given the orthogonality definition, the polynomials can be used as the basis to approximate a function of x. If the model function g is integrable and belongs to the mean-square integrable function space

$$L^2_{p(x)}(S_{\mathcal{X}}) = \left\{ g : S_{\mathcal{X}} \to \mathcal{Y} \mid \mathbb{E}\left[g^2\right] < \infty \right\} \;, \tag{2.40}$$

then it is possible to define the PCE $\tilde{g}(x)$ of the model $g(x)$ as

$$\tilde{g}(x) \approx \sum_{h=0}^{d} c_h \phi_h(x) \;, \tag{2.41}$$

where the polynomial coefficients c_h are

$$c_h = \frac{\mathbb{E}\left[g(x)\phi_h(x)\right]}{\gamma_h} \;, \tag{2.42}$$

and γ_h is the normalization constant as in Eq. (2.34). The approximation sign in Eq. (2.41) is due to the truncation of the sum to a certain degree d. The relation is exact for $d \to \infty$. This approximation is also called "strong PCE approximation" when the model function is known as a priori. The counter approximation is known as "weak PCE approximation", which occurs when the output's probability distribution is given [179]. The demonstration of the latter approximation is omitted.

Multi-dimension formulation   So far, only the one-dimensional case has been analyzed, i.e., when $M = 1$. In this case, the orthogonal polynomials ϕ_d are univariate basis functions since they include only one random variable. In multiple dimensions systems, the uncertainty is driven by a generic random vector $\boldsymbol{x} = [x_1, \ldots, x_M]$. In this other case, the derivation of a multivariate basis for the expansion is needed. Given the variable independence, their joint PDF is $p(\boldsymbol{x}) = \prod_i^M p(x_i)$. Each component x_i of the random vector $\boldsymbol{x}$ is represented by the univariate PCE basis function ϕ_d of degree up to d [179].

Before proceeding with the construction of a multivariate basis of the PCE, the multi-index definition is necessary. The new basis has to include as many univariate basis functions as the dimensionality of the problem M and degree up to d. The multi-index is employed to identify all these characteristics. Thus, the multi-index $\boldsymbol{\alpha} = (\alpha_1, \alpha_2, \ldots, \alpha_M)$ is defined in the set $\mathcal{A} \subseteq \mathbb{Z}_0^M$, and $||\boldsymbol{\alpha}||_1 = \alpha_1 + \ldots + \alpha_M$. The formalization used in the text refers to the *graded lexicographic order*, and it is visualized in Tab. 2.4 for the case of $M = 3$. Consider that the notation employed in $||\boldsymbol{\alpha}||_1$ refers to the p-norm definition for $p = 1$, and defined as

$$||x||_p := \left(\sum_{i=1}^M |x_i|^p \right)^{1/p} \qquad p \in \mathbb{R}. \tag{2.43}$$

The multivariate basis functions, with generic degree d and dimension M are constructed by the univariate functions of degree up to d, i.e., $1 \leqslant ||\boldsymbol{\alpha}||_1 \leqslant d$, as

$$\Phi_{\boldsymbol{\alpha}}(\boldsymbol{x}) = \prod_{i=1}^M \phi_{\alpha_i}(x_i) \ . \tag{2.44}$$

As for the one-dimensional case, by defining the space of all mean-square integrable function of $\boldsymbol{x}$ as [179]

$$L_{p(\boldsymbol{x})}^2(S_{\mathcal{X}}) = \left\{ g : S_{\mathcal{X}} \to \mathcal{Y} \ \middle| \ \int_{S_{\mathcal{X}}} g^2(x) p(x) \mathrm{d}x < \infty \right\} \ , \tag{2.45}$$

then the multi-variate PCE projection of degree up to d for a model $g(\boldsymbol{x})$ is given by

$$\widetilde{g}(\boldsymbol{x}) = \sum_{\boldsymbol{\alpha} \in \mathcal{A}} c_{\boldsymbol{\alpha}} \Phi_{\boldsymbol{\alpha}}(\boldsymbol{x}) \ . \tag{2.46}$$

The span of the multivariates space has the same dimension of $\mathcal{A}$, which is

$$N_c = \binom{M + d}{d} \ . \tag{2.47}$$

To ease the notation, the set $\mathcal{A}$ of the expansion indices can also be referred to as

$$\mathcal{A} = \mathcal{A}^{M,d} \equiv \left\{ \boldsymbol{\alpha} \in \mathbb{Z}_0^M \ \middle| \ ||\boldsymbol{\alpha}||_1 \leqslant d \right\} \ . \tag{2.48}$$

Naturally, increasing the degree of the expansion, as in $d \to \infty$, would eventually lead to [179]

$$||g(\boldsymbol{x}) - \widetilde{g}(\boldsymbol{x})||_{L_{p(\boldsymbol{x})}^2(S_{\mathcal{X}})} \to 0 \ . \tag{2.49}$$

Table 2.4.: Graded lexicographic order formalization of the multi-index $\boldsymbol{\alpha}$, for the case of $M = 3$.

$\|\boldsymbol{\alpha}\|_1$	$\boldsymbol{\alpha}$	Index
0	(0 0 0)	1
1	(1 0 0)	2
	(0 1 0)	3
	(0 0 1)	4
2	(2 0 0)	5
	(1 1 0)	6
	(1 0 1)	7
	(0 2 0)	8
	(0 1 1)	9
	(0 0 2)	10
3	(3 0 0)	11
	(2 1 0)	12
	$\ldots$	$\ldots$

The coefficients $c_{\boldsymbol{\alpha}}$ in the expansion are computable as in Eq. (2.42), i.e.,

$$c_{\boldsymbol{\alpha}} = \frac{\mathbb{E}\left[g(\boldsymbol{x})\Phi_{\boldsymbol{\alpha}}\right]}{\gamma_{\boldsymbol{\alpha}}} \ . \tag{2.50}$$

In conclusion, it is possible to define the linear space $\mathbb{P}_d^M(\boldsymbol{x})$ of all polynomials of degree up to d and dimension M as [179]

$$\mathbb{P}_d^M(\boldsymbol{x}) = \left\{ g : S_{\mathcal{X}} \to \mathbb{R} \ \middle| \ g(\boldsymbol{x}) = \sum_{1 \leqslant \|\boldsymbol{\alpha}\|_1 \leqslant d} c_{\boldsymbol{\alpha}} \Phi_{\boldsymbol{\alpha}} \right\} \ , \tag{2.51}$$

whose dimension is N_c. In the following part, the multi-dimensional formulation will be used as a basis for describing PCE characteristics since its particular one-dimensional case is easily derivable, e.g., $M = 1$.

2.4.1. PCE statistics

The PCE plays a vital role also in the computation of model statistics, assuming that a strong approximation is available and that the error in Eq. (2.49) is proximal to zero. Thus, assume a surrogate $\widetilde{g}$ for a model $y = g(\boldsymbol{x})$, as previously mentioned. The expected value of the model is

given by [48]

$$\mathbb{E}\left[y\right] = \mathbb{E}\left[\widetilde{g}(\boldsymbol{x})\right] = \int_{\mathcal{X}} \left(\sum_{\boldsymbol{\alpha} \in \mathcal{A}} c_{\boldsymbol{\alpha}} \Phi_{\boldsymbol{\alpha}}(x) \right) p(x) \mathrm{d}x = c_0 \; , \tag{2.52}$$

where c_0 is the first expansion coefficient for $||\boldsymbol{\alpha}||_1 = 0$. Similarly, the variance of the system can be easily computed from

$$\mathbb{V}\left[y\right] = \mathbb{V}\left[\widetilde{g}(\boldsymbol{x})\right] = \mathbb{E}\left[\left(\widetilde{g}(\boldsymbol{x}) - \mathbb{E}\left[\widetilde{g}(\boldsymbol{x})\right]\right)^2\right] = \sum_{0 < ||\boldsymbol{\alpha}||_1 \leqslant d} \gamma_{\boldsymbol{\alpha}} c_{\boldsymbol{\alpha}}^2 \; . \tag{2.53}$$

2.4.2. Sensitivity analysis from PCE

The estimation of the two variance-based sensitivity indices in Eq.s (2.30) and (2.31) is performed from the expansion coefficients $c_{\boldsymbol{\alpha}}$ [39, 46]. As visible from their formulation, the indices are a function of the variance $\mathbb{V}\left[y\right]$ and conditional variance $\mathbb{V}\left[y|x_i\right]$ of the model output. As visible in Eq. (2.52) and (2.53), the mean and variance of the system are assessable from the expansion coefficient. Two additional sets of indices are introduced, namely $\mathcal{A}_i$

$$\mathcal{A}_i = \left\{ \boldsymbol{\alpha} \mid \alpha_i > 0 \wedge \alpha_{i'} = 0 \quad \forall i' \neq i \right\} \; , \tag{2.54}$$

and $\mathcal{A}_{T,i}$

$$\mathcal{A}_{T,i} = \left\{ \boldsymbol{\alpha} \mid \alpha_i > 0 \right\} \; . \tag{2.55}$$

The first includes all the multi-indices in which the polynomials in the only variable x_i have a non-zero degree, while others have zero degrees. For example, $\boldsymbol{\alpha} = (0\ 2\ 0)$ indicates the second degree polynomial of the variable x_2, for $M = 3$ and $||\boldsymbol{\alpha}||_1 = 2$. The second set includes all the multi-indices in which the polynomials in the variable x_i have a non-zero degree, e.g., $\boldsymbol{\alpha} = (2\ 1\ 0\ 0)$, for $M = 4$ and $||\boldsymbol{\alpha}||_1 = 3$. Consequently, $\mathcal{A}_i \subseteq \mathcal{A}_{T,i}$ [45].

Therefore, the first Sobol indices can also be assessed from the PCE coefficient as in [158]

$$S_i \approx \frac{1}{\mathbb{V}\left[\widetilde{g}(\boldsymbol{x})\right]} \sum_{\boldsymbol{\alpha} \in \mathcal{A}_i} \mathbb{V}\left[c_{\boldsymbol{\alpha}} \Phi_{\boldsymbol{\alpha}}(\boldsymbol{x})\right] = \frac{\sum_{\boldsymbol{\alpha} \in \mathcal{A}_i} c_{\boldsymbol{\alpha}}^2}{\sum_{\boldsymbol{\alpha} \in \mathcal{A}} c_{\boldsymbol{\alpha}}^2} \; , \tag{2.56}$$

and the total Sobol index as

$$S_i^{\mathrm{T}} \approx \frac{1}{\mathbb{V}\left[\widetilde{g}(\boldsymbol{x})\right]} \sum_{\boldsymbol{\alpha} \in \mathcal{A}_{T,i}} \mathbb{V}\left[c_{\boldsymbol{\alpha}} \Phi_{\boldsymbol{\alpha}}(\boldsymbol{x})\right] = \frac{\sum_{\boldsymbol{\alpha} \in \mathcal{A}_{T,i}} c_{\boldsymbol{\alpha}}^2}{\sum_{\boldsymbol{\alpha} \in \mathcal{A}} c_{\boldsymbol{\alpha}}^2} \; . \tag{2.57}$$

These formulations are very convenient from a computational point of view, meaning that once the PCE of a system is built, the assessment of the Sobol indices comes with almost no effort. They are computed by collecting the needed coefficients of the expansions, squaring, summing, and normalizing them by the expansion total variance.

For the case of dynamic processes, i.e., the model output is dependent on time, a new formulation has been adapted from the proposed work of Alexanderian et al. [3]. In these cases, the generalized sensitivity indices read as

$$S_i = \frac{\int_T \sum_{\boldsymbol{\alpha} \in \mathcal{A}_i} c_{\boldsymbol{\alpha}}^2(\tau) \mathrm{d}\tau}{\int_T \sum_{\boldsymbol{\alpha} \in \mathcal{A}} c_{\boldsymbol{\alpha}}^2(\tau) \mathrm{d}\tau} \; , \tag{2.58}$$

$$S_i^{\mathrm{T}} = \frac{\int_T \sum_{\boldsymbol{\alpha} \in \mathcal{A}_{T,i}} c_{\boldsymbol{\alpha}}^2(\tau) \mathrm{d}\tau}{\int_T \sum_{\boldsymbol{\alpha} \in \mathcal{A}} c_{\boldsymbol{\alpha}}^2(\tau) \mathrm{d}\tau} \; . \tag{2.59}$$

The only complication that is left regards the computation of such expansion coefficients.

2.4.3. Coefficients estimation

Historically, when PCE was implemented by Ghanem and Spanos [66], the expansion solution was mainly performed with the Galerkin method. This method's deterministic procedure consists of finding an approximate solution in a Hilbert space H s.t. the error generated by the approximation is orthogonal to the H space. In the case of a PCE, the Galerkin approach becomes stochastic so that the approximate solution belongs to $\mathbb{P}_d^M(\boldsymbol{x})$ defined in Eq. (2.51). For example, consider a general PDE system represented by the following scalar equation

$$y(s, t, \boldsymbol{x}) : \overline{\Omega} \times [0, T] \times \mathbb{R}^M \to \mathbb{R} \; , \tag{2.60}$$

where y could be considered as any system unknown, e.g., displacement. $\overline{\Omega}$ is the closure of the space domain, as in $\overline{\Omega} = \Omega + \Gamma$, $T > 0$ denotes the time domain, and $\boldsymbol{x} \in \mathbb{R}^M$ is the random vector. A PCE projection of the problem, says $\widetilde{y}(s, t, \boldsymbol{x})$ of degree up to d, requires the implementation of such expansion in the PDE system, resolving in a system of coupled deterministic equations, whose dimension is again $N_c = \binom{M+d}{d}$. This method requires a complex implementation in the problem, and it is therefore classified as an *intrusive* technique. Given this motivation, the Galerkin procedure is disregarded for the assessment of a model PCE [179].

Alternatively, other techniques were developed, known as *non-intrusive*, since no implementation is required and the PCE solution is drawn from selected model solutions. This category is further divided into two main classes, the projection, and the regression methods.

Projection methods The projection method involves the definition of orthogonality, as expressed in Eq. (2.39), from which the coefficients are computed by simply solving for $c_{\boldsymbol{\alpha}}$. However, the solution of such an integral requires quadrature techniques, where the integral is approximated through a weighted sum

$$c_{\boldsymbol{\alpha}} = \int_{\mathcal{X}} g(x) \Phi_{\boldsymbol{\alpha}}(x) p(x) \mathrm{d}x \approx \sum_{q=1}^{N_q} w^{(q)} g(x^{(q)}) \Phi_{\boldsymbol{\alpha}}(x^{(q)}) \; , \tag{2.61}$$

where $w^{(q)}$ are the weight, $x^{(q)}$ the quadrature points, and N_q are the number of integration points. The first ones are defined as the roots of the polynomials orthogonal to the joint distribution

function $p(\boldsymbol{x})$. The accuracy of the approximation strictly depends on the number of integration points. Their amount is $N_q = (d+1)^M$. Consequently, for large models, that is for $M \gg 1$, this number increases rapidly, leading to the well-known *curse of dimensionality.*

While the Gaussian quadrature is based on a tensor-product of univariate integration rule, the more recent sparse quadrature method developed by Smolyak allows reaching the same numerical accuracy with less needed points. An alternative to the quadrature method would be a Monte Carlo approach to solve Eq. (2.61). However, considering the typical complexity of many engineering applications, this last technique is usually discarded a priori [179].

Regression methods   The regression approach initiates from the PCE approximation of the original model. As already mentioned, the discrepancy, or error, between the two decreases for an expansion degree $d \to \infty$. However, this is impractical in engineering applications. Therefore, the approximation error ε can be included in Eq. (2.46) as [46]

$$\widetilde{g}(\boldsymbol{x}) = \sum_{\boldsymbol{\alpha} \in \mathcal{A}} c_{\boldsymbol{\alpha}} \Phi_{\boldsymbol{\alpha}}(\boldsymbol{x}) + \varepsilon \ . \tag{2.62}$$

The minimization of the error can be performed through a least-squares minimization problem. A matrix formulation of the above expression is given as

$$g(\boldsymbol{x}) = \widetilde{g}(\boldsymbol{x}) \equiv \boldsymbol{c}^{\mathrm{T}} \Psi(\boldsymbol{x}) + \varepsilon \ , \tag{2.63}$$

where $\boldsymbol{c}$ is the vector of the coefficients, and $\Psi(\boldsymbol{x})$ is the vector of the multivariate polynomials. The least-square minimization problem formulation is

$$\widetilde{\boldsymbol{c}} = \arg \min \mathbb{E}\left[\left(\boldsymbol{c}^{\mathrm{T}} \Psi(\boldsymbol{x}) - g(\boldsymbol{x}) \right)^2 \right] \ . \tag{2.64}$$

The solution of this problem is usually approached with an ordinary least-square (OLS) approach by assuming that a sampling of the input and output is available. Indeed, assume $\Theta = (\theta^{(1)}, \dots, \theta^{(N_s)})^T$ to be the input sample of dimension N_s of the input $\boldsymbol{x}$. Equally, Ξ is the output sample computed from the model's solution for each $\theta^{(k)}$. The OLS is

$$\widetilde{\boldsymbol{c}} = \left(\boldsymbol{A}^{\mathrm{T}} \boldsymbol{A} \right)^{-1} \boldsymbol{A}^{\mathrm{T}} \Xi \ , \tag{2.65}$$

where $A_{ij} = \phi_j(\theta^{(k)})$ is the regression matrix composed of the expansion basis polynomial ϕ_j computed in the sampling point $\theta^{(k)}$, thus $\boldsymbol{A} \in \mathbb{R}^{N_s,(d+1)}$. Although this approach is more affordable than the projection method for estimating the expansion coefficients, it does include one critical challenge. The choice of N_s has to be s.t. Eq. (2.65) can be overdetermined, i.e., $N_s > N_c$. In practice, for good approximation is suggested to have $N_s = 2N_c$ [48, 78], although the rule of *the more, the merrier* always applies. In Fig. 2.9, the number of unknown coefficients N_c and needed samples N_s is displayed for different model dimensions and PCE degrees.

Recently, Blatman and Sudret [23] introduced an adaptive sampling technique to reduce the required model simulations for the regression approach. By comparing the accuracy of the
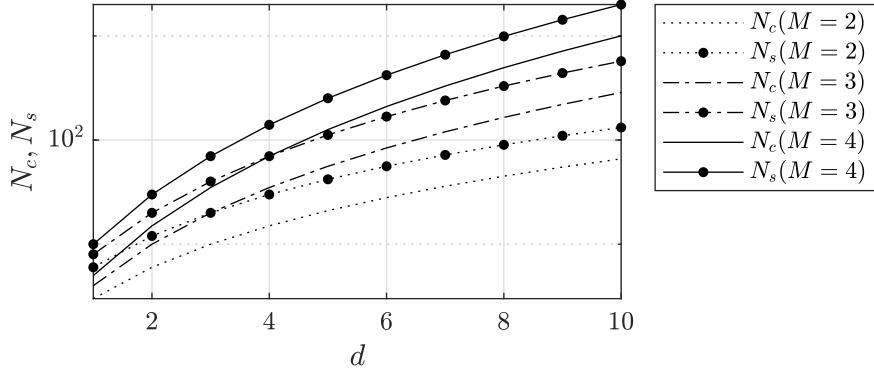
Figure 2.9.: Relationship between number of unknown coefficients N_c and sampling points N_s per model dimension M and PCE degree d.

PCE, they were able to reduce the number of required computational simulations radically. Then, they introduced in [24] another improvement to reduce the number of necessary model simulations, namely the hyperbolic scheme. Here, they introduce a quasi-norm truncation of the computable coefficients, penalizing the high interactions terms in the expansion, i.e., those where all random variables are included. Specifically, it is called quasi-norm since it does not satisfy the triangular inequality property of the common mathematical norm. Such truncation derives from the principle of sparsity-of-effects, which assumes that high-order interactions are often negligible since systems variations are due to main-effects or low-order interaction at most [114]. In other words, consider the set $\mathcal{A}$ of the multi-index $\boldsymbol{\alpha}$ defined as in Eq. (2.48). The hyperbolic truncation scheme with a p'-quasi-norm is given by [24]

$$\mathcal{A}_{p'} \equiv \left\{ \boldsymbol{\alpha} \in \mathbb{Z}_0^M \,\big|\, ||\boldsymbol{\alpha}||_{p'} \leqslant d \right\} \,, \tag{2.66}$$

where

$$||\boldsymbol{\alpha}||_{p'} = \left(\sum_{i=1}^{M} \alpha_i^{p'} \right)^{1/p'} \quad \text{for} \quad 0 < p' < 1 \,. \tag{2.67}$$

The p'-quasi-norm does not have to be confused with the p-norm introduced earlier. As a matter of fact, the lack of the absolute value in Eq. (2.67) does not satisfy the triangular inequality property of the p-norm. The number of unknown coefficients to compute in the PCE is substantially reduced. An example is given in Fig. 2.10, where the comparison is made for different PCE degrees d and model dimension $M = 10$.

Blatman and Sudret [24] also introduced a new method for computing the PCE coefficients based on least angle regression (LARS). In this method, several PCE are computed s.t. their model predictability is as accurate as possible. The algorithm starts with the computation of a basic PCE, i.e., all polynomial coefficients are set to zero but the first one. A surrogate and its discrepancy to the model are computed. This procedure is repeated iteratively by incrementing the number of coefficients to solve, and it is stopped when the discrepancy error is stable or converges.
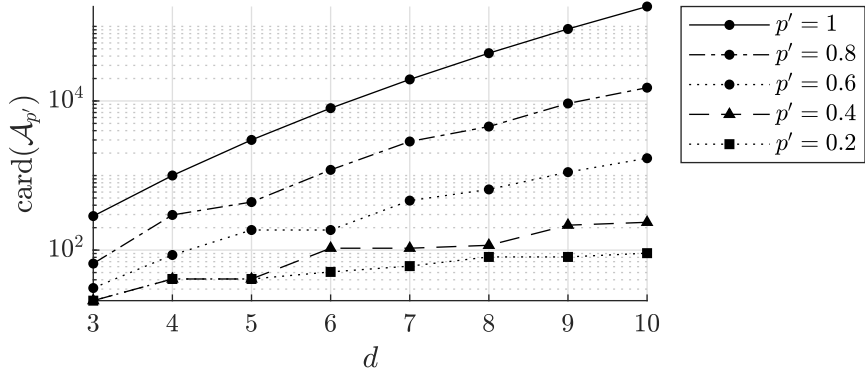
Figure 2.10.: Number of unknown coefficients for a PCE of various degree d and model dimension $M = 10$. The number of unknowns are truncated through the hyperbolic truncation scheme, for different values of p'-quasi-norm values.

Error estimation   The error estimation of the PCE is computable in several ways [99]. A general formulation is given by ε, where the variance of the computed output normalizes the discrepancy between the model and the surrogate. Its formulation is

$$
\varepsilon = \frac{\mathbb{E}\left[(g(\Theta) - \widetilde{g}(\Theta))^2\right]}{\mathbb{V}\left[\Xi\right]} \; . \tag{2.68}
$$

Other formulations are also available [99]. The normalized empirical error ε_{emp} considers the surrogate's accuracy in the available experimental design realizations, as in

$$
\varepsilon_{\text{emp}} = \frac{\sum_k^{N_s} \left(g(\theta^{(k)}) - \widetilde{g}(\theta^{(k)})\right)^2}{\sum_k^{N_s} \left(g(\theta^{(k)}) - \mathbb{E}\left[g(\Theta)\right]\right)^2} \; , \tag{2.69}
$$

where $\theta^{(k)}$ is a generic input sample realization. The problem of this formulation is that it is affected by the over-fitting problem, i.e., the error does not reduce by increasing N_s, but by increasing the degree d of the surrogate $\widetilde{g}(\Theta)$. Blatman and Sudret [23] introduced the leave-one-out error ε_{LOO} based on a cross-validation procedure to overcome this issue, which was developed for machine-learning problems. For the evaluation of ε_{LOO}, several surrogates are built, each from a reduced experimental design $\Theta \backslash \theta^{(k)}$ that excludes the i-th observation from the training set Θ. Therefore, ε_{LOO} is given as

$$
\varepsilon_{\text{LOO}} = \frac{\sum_k^{N_s} \left(g(\theta^{(k)}) - g_{PCE \backslash i}(\theta^{(k)})\right)^2}{\sum_k^{N_s} \left(g(\theta^{(k)}) - \mathbb{E}\left[g(\Theta)\right]\right)^2} \; , \tag{2.70}
$$

where $g_{PCE \backslash i}$ is the surrogate model built from the reduced experimental design $\Theta \backslash \theta^{(k)}$. When a least-square minimization procedure is employed, the computation of ε_{LOO} is easily computable from the regression matrix $\boldsymbol{A}$, see Eq. (2.65).

Part II.

Applications and results

3. On electrical conductivity of flowing human blood

The scientific outcome presented in this chapter mainly focuses on the theory at the base of a detecting method for aortic dissection, namely impedance cardiography (ICG). This method involves injecting electrical current into a body and measuring the impedance from sensors. The idea is based on this signal being able to detect volume changes in the body, particularly the AD disease. However, physiological and geometrical uncertainties make the simulations pretty insecure. The electrical conductivity of blood is at the base of the ICG method. This property of the fluid allows the computation of the ability of the fluid to conduct electrical current. On this topic, the scientific publication by Melito et al. [105] is here presented. It is based on a sensitivity analysis study on the effect of fluid and mechanics assumptions on the electrical conductivity of flowing blood.

3.1. Introduction

Blood is a heterogeneous suspension of several components, consisting of plasma as the carrier fluid, as well as erythrocytes (red blood cells), leukocytes (white blood cells) and thrombocytes (platelets) as the cellular content. The fluid is physically complex and, due to its physiological importance, its chemical and physical properties have been studied in numerous scientific fields, [38, 54, 57, 108, 109, 164, 171, 173].

It is generally assumed that the physical properties of whole blood, such as the viscosity, i.e., its resistance to rates of deformation, and the electrical conductivity, are mainly determined by the properties of the red blood cells (RBCs) and the surrounding blood plasma. Furthermore, the electrical conductivity of blood is a crucial factor for electrical bioimpedance measurement applications in clinical settings [13, 134, 168].

The electrical properties of stationary blood depend mainly on the volume fraction of RBCs in the blood plasma, namely the hematocrit [55], RBCs' shape and orientation, and the temperature of the blood. In Maxwell [101], the research on electrical conductivity began from a dilute suspension of spherical and ellipsoidal isolating particles in an electrolyte. From there, the findings produced the Maxwell-Fricke theory, which allows accurate calculation of the conductivity of stationary blood with randomly oriented RBCs as a function of hematocrit.

To study electrical properties on flowing blood, Edgerton [49] elaborated the theory quantitatively by introducing a Couette and successively a Poiseuille flow, and adding probability

distributions for the orientation angles of RBCs. While the Couette flow is characterized by a shear-induced flow, the Poiseuille one is a pressure-induced flow. Within the Couette flow, the distribution of RBCs' orientation angles are dependent on the flow's shear rate until an orientation equilibrium is reached; the equilibrium of orientation distribution appears at low shear stress for high hematocrit values. Furthermore, after equilibrium is reached, the viscosity decreases continuously due to deformation of the RBCs. The reduction of viscosity is also confirmed at the breakup of rouleaux at low shear rates, a phenomenon leading to viscosity change. Regarding the Poiseuille flow, it is concluded that the RBCs orientation is crucial for blood conductivity.

Years later, the Maxwell-Fricke theory was tested for human blood in Poiseuille flow [170]. It was concluded that the cell orientation is the dominant cause of the electrical conductivity changes of blood, although large deformations of the RBCs occur. However, Sakamoto and Kanai [139] and Fujii et al. [56] showed that if only the orientation of RBCs is considered, the conductivity changes do not depend on the shear rate for higher hematocrit levels (above 20 %). Therefore, since an equilibrium orientation of the RBCs is reached at a low shear rate, for higher shear rates the conductivity changes are due to deformation of RBCs.

In Hoetink et al. [76], the Maxwell-Fricke theory was used to explain the dependency of the electrical conductivity of blood on its flow condition in a cylindrical tube. For this setup, the authors assumed a shear-rate independent viscosity fluid in a steady flow, in which RBCs are oblate ellipsoids that get deformed and oriented, given the flow condition. Since the conductivity of RBCs is very low at frequencies below 3 MHz, the current distribution in the suspension and thus the mean conductivity of this domain changes with the altered RBCs condition and configuration. This study leaves the electrical conductivity change of blood through the aorta due to its pulsatile flow condition unexplored.

To overcome this issue, Gaw et al. [62–64] introduced a study on the impact of pulsatile blood flow on the electrical conductivity of blood in a cylindrical tube with rigid walls, using the flow theory developed by Womersley [178]. In this case, it was visible, both theoretically and experimentally, that during the acceleration phase of the fluid, i.e., the systolic phase of the cardiac cycle, a robust linear relationship between the average velocity and the conductivity of blood exists. The computed impedance shows differences in both systole and diastole related to the same average velocity. The latter phenomenon introduced a significant new insight into the physiological origins of impedance variations in bioimpedance methods. Developments performed by Shen et al. [147] include an elastic tube instead of a rigid one for the domain of the model. It results in highlighting the strong influence of the centre-line velocity value and the low impact of the wall elasticity on the electrical conductivity of blood.

Blood exhibits non-Newtonian behavior dominated by shear thinning, which must be accounted for in simulating blood flows of the human body. Many models for blood flow, including the sources mentioned above, however, are subject to basic assumptions which may differ from the physical reality. Examples relate to the state of flow and the fluid dynamic behavior upon deformation. For example, the flow is modelled either steady or pulsating.

The rheological behavior of blood is highly complex because its exact composition is more or less unique for each person. Broken down to the most important influencing factor regarding

viscosity, the hematocrit value varies from person to person in a certain range for average women and men (adult males: 42 % to 54 %; adult women: 38 % to 46 % [172]). However it may differ by 4 % to 7 % due to pregnancy [117] or exceed 60 % for professional athletes [169].

The present work focuses on analysing the electrical conductivity of flowing blood through a variance-based global sensitivity analysis (SA) [146] by considering different flow situations (steady or pulsating) and rheological behavior (Newtonian or non-Newtonian). Variance-based SA can be performed with Monte Carlo method, which requires a high number of model simulations [48]. However, when dealing with complex model structure, surrogate models are usually preferred. Herein, the polynomial chaos expansion is used as surrogate model for the assessment of the sensitivity indices [158].

The uncertainty in computational models can originate from two different sources: in the model's input parameters and in the model selection. To reduce the first, a well-known uncertainty and sensitivity analysis is performed based on the assessment of the sensitivity indices from the PCE, see [94]. As for the model selection analysis, a discrete variable, namely the *trigger*, is added in the input space of the surrogate model. To the knowledge of the authors, the latter approach is innovative and not found in the literature.

The uncertainty quantification of the model selection was introduced with a Bayesian approach by Kass and Raftery [87], where the posterior probabilities of all competing models are computed. The method, named Bayesian model averaging [75], highlights the need for considering the uncertainty in the model selection to avoid over-confident inference and decision. A latest application of Bayesian model averaging can be found in Jia et al. [85] where the best model choice is compared with the computed posterior probability. Lately, the approach was illustrated in Saltelli et al. [143] for the scope of sensitivity analysis and then applied in Saltelli et al. [145]. Other applications of model selection are found in countries composite indicators [138, 144, 160], geological analysis of potential oil basins [140], and CO_2 storage ability [85]. However, they all use Monte Carlo method to asses the sensitivity of several competing models. Therefore, a trigger variable in the input space of the surrogate model is introduced in this paper.

In the current study, different flow properties are studied by the trigger variable that simulates the change in the model assumption, i.e. emulating a switch behavior. Differences between steady and pulsating flow with different fluid types (Newtonian or non-Newtonian) are predicted. The input space will also include different properties of the blood, distinguishing different patient-specific cases. In the pulsating case, the SA will focus on the computation of the conductivity of blood in one cardiac cycle as a model output. The study aims to provide a more profound understanding of the mechanisms governing the value of the conductivity of flowing blood. The differences in the conductivity of blood due to the varied model parameters will lead to conclusions on the model sensitivity for this study case.

3.2. Methods

In this section, the methods used to carry out and analyze the illustrated problem will be analyzed. First, the model for calculating the electrical conductivity of blood will be presented.

The method introduced by Hoetink et al. [76], conceived for steady-state flows, will be presented, followed by the method introduced by Gaw et al. [63], which assumes a pulsating flow type. Both of these methods were designed for Newtonian fluids. Consequently, to amplify the method to non-Newtonian-type fluids, the formulation of the latter is described. Ultimately, the fluid domain models for both cases, Newtonian and non-Newtonian, are presented. Similarly, the cases of stationary and pulsating flow will be described for both types of fluid.

Particular attention is given to the representation of non-dimensional quantities that can fully describe the introduced systems. As will be shown later, these quantities are the famous Reynolds number and Womersley number. In addition, a new non-dimensional quantity is introduced, which describes the relationship between the pulsating and stationary flow.

Finally, the uncertainty quantification and sensitivity analysis used in this application will be briefly described, as more details about them are provided earlier in Part I of the text. A representation of the schematic of the present chapter and the coupled model is visualized in Fig. 3.1.

3.2.1. Electrical conductivity of blood

The electrical conductivity of the blood is computed by assuming the fluid to be a dilute suspension of ellipsoidal particles [55, 101]. The fluid flows in a straight and rigid pipe, where the RBCs, surrounded by plasma, are considered at the center of each control volume [76]. The control volumes are given by the fluid domain discretization. The RBCs are oriented and deformed due to the shear stress induced by the fluid.

The conductivity of flowing blood was initially modeled by Hoetink et al. [76] for a Newtonian fluid in steady laminar flow through a rigid tube of cylindrical shape. This model extends the Maxwell-Fricke theory by introducing orientation and deformation terms of RBCs in the flow. Here, different shear stress thresholds exert different orientation conditions of the RBCs. This work is based on the early findings of Visser [170] on the study of electrical conductivity of stationary and flowing human blood. The system formulation kept improving over the time, and in Gaw et al. [64], the model was extended by incorporating a pulsatile flow and different orientation effects. Therefore, the assumptions taken in Gaw et al. [64] for the computation of electrical conductivity of blood are herein considered and applied [105].

Orientation and deformation of RBCs RBCs are subject to orientation and deformation in flowing blood due to shear rate. Only two states of orientation for the RBCs are considered: a random orientation, as in flipping disk behavior, and a stable orientation, as in liquid drop behavior. In the latter, given that the RBCs are aligned with their major $2b_0$ axis, see Fig. 3.2, within $\pm 20°$ from the axial and dominant flow direction, RBCs are assumed to be parallel to the flow direction [22].

When a pulsation of the flow is present, the time delay in the alignment of the RBCs to the flow field has to be accounted for. Such effect depends highly on the shear rate experienced by the cells and the acceleration of the flow [21, 171]. To tackle the orientation rate as a function of
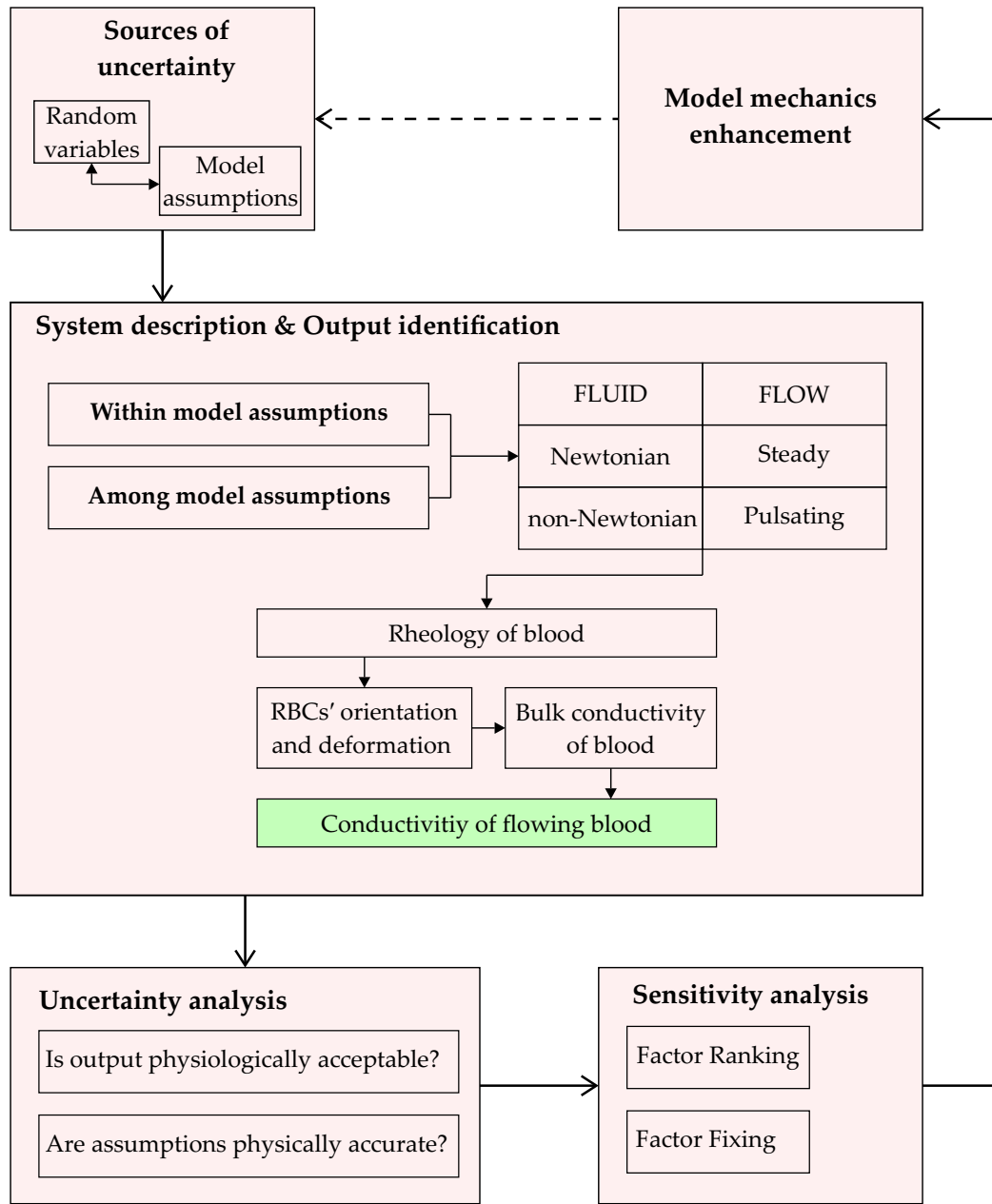
Figure 3.1.: Schematic description of the current chapter and visualization of the diagram of the computational model. The quantity of interest of the model is highlighted in green.

3. On electrical conductivity of flowing human blood
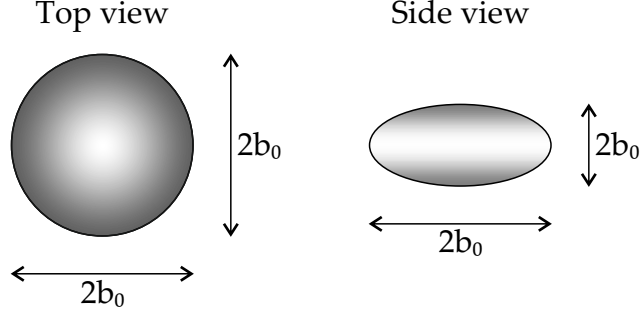
Figure 3.2.: Top and side view view of a red blood cell (RBC) modeled as an ellipsoidal particle.

the shear rate, the function $f(r)$ at a distance r from the pipe axis, as introduced by Bitbol and Quemada [22], is shown as

$$f(r) = \frac{n_{\|}}{n_{\mathrm{RBC}}} = \frac{\tau_{\mathrm{o}}^{-1}(r)}{\tau_{\mathrm{d}}^{-1}(r) + \tau_{\mathrm{o}}^{-1}(r)} \;, \tag{3.1}$$

where n_{RBC} is the total number of RBCs per unit volume, of which $n_{\|}$ are parallel to the flow, τ_{o} is the time constant for parallel orientation of cells, and τ_{d} is the time constant for the aligned cells to disorient in randomly oriented cells. The formulations of τ_{o} and τ_{d} are expressed in Bitbol and Quemada [22] as proportional to the inverse of the shear rate for τ_{o} and as proportional to the inverse of the square root of the shear rate for τ_{d}.

Consider the RBCs as ellipsoidal particles with one symmetry axis of length $2a_0$ and two axes of equal length $2b_0$, s.t. $a_0 < b_0$, see Fig. 3.2. An erythrocyte with initial axes ratio a_0/b_0 is deformed into $a_{\mathrm{d}}(r)/b_{\mathrm{d}}(r)$ due to shear stress present in a pipe flow. This deformation is inversely proportional to the membrane shear modulus μ_{RBC} of the cells [76], and it is described as

$$\frac{a_{\mathrm{d}}(r)}{b_{\mathrm{d}}(r)} = \frac{a_0}{b_0} \left[1 + \frac{||\boldsymbol{\tau}||_2(r) b_0}{4\mu_{\mathrm{RBC}}} \right]^{-3} \tag{3.2}$$

where $\boldsymbol{\tau}$ is the shear, or deviatoric, stress tensor.

This quantity depends on the position in the flow field and relates the state of deformation of the RBCs to the state of flow.

Conductivity of blood   The conductivity of blood is then computed from the Maxwell-Fricke theory, with the formulation introduced by Hoetink et al. [76], in which the conductivity of blood of a control volume $\sigma_{\mathrm{cv}}(r)$ is given by

$$\frac{\sigma_{\mathrm{cv}}(r)}{\sigma_{\mathrm{pl}}} = \frac{1 - H}{1 + (C(r) - 1) H} \;, \tag{3.3}$$

where σ_{pl} is the conductivity of the blood plasma measured in $\mathrm{S\,m}^{-1}$, H is the hematocrit level of the blood, and $C(r)$ is the term accounting for the orientation and the deformation of RBCs

at a radial location r in the pipe. In particular, the RBCs are considered impermeable to the electrical field for frequencies in the range of several hundred kHz, and therefore their amount in the blood volume is particularly significant. The following formulation gives the calculation of $C(r)$ [64]

$$C(r) = f(r)C_{\mathrm{b}} + (1 - f(r))\, C_{\mathrm{r}} \;, \tag{3.4}$$

where $f(r)$ is the function for the orientation of RBCs from Eq. (3.1), and C_{b} and C_{r} are terms that account for the alignment of RBCs. C_{r} is the average of the C values for each axis alignment to the flow as in:

$$C_{\mathrm{r}} = \frac{1}{3}(C_{\mathrm{a}} + 2C_{\mathrm{b}}) \;, \tag{3.5}$$

where $C_{\mathrm{a}} = 1/F$, $C_{\mathrm{b}} = 2/(2 - F)$, and F is the deformation term computed as

$$F(a_0 < b_0) = \frac{\beta - \frac{1}{2}\sin{(2\beta)}}{\sin^3 \beta}\cos\beta \;, \tag{3.6a}$$

$$\cos\beta = \frac{a_{\mathrm{d}}(r)}{b_{\mathrm{d}}(r)} \;. \tag{3.6b}$$

The RBC orientation and deformation is coupled with the Maxwell-Fricke theory by substituting Eq. (3.2) in Eq.s (3.6a) and (3.6b). The bulk conductivity of blood is computed as the integral of the control volume's conductivity over the pipe's cross-sectional area of radius R as

$$\sigma_{\mathrm{bl}} = \frac{2}{\mathrm{R}^2}\int_0^{\mathrm{R}} \sigma_{\mathrm{cv}}(r)r\mathrm{d}r \;. \tag{3.7}$$

Finally, given the conductivity of stationary blood σ_{st} in which RBCs' orientation and deformation do not occur [170], the conductivity change of blood against its stationary value, expressed in percent, is computed as [105]

$$\Delta\sigma_{\mathrm{bl}} = \left(\frac{\sigma_{\mathrm{bl}} - \sigma_{\mathrm{st}}}{\sigma_{\mathrm{st}}}\right)100 \;. \tag{3.8}$$

where the electrical conductivity of stationary blood is computed as proposed by Visser [170].

3.2.2. Rheology of blood

The fluid model of the blood is collected and re-adapted from Melito et al. [105]. For the present illustration, blood flow through a cylindrical vessel with a circular cross-section is simulated, comparing the steady and unsteady blood flow modeled as a Newtonian or a non-Newtonian liquid. The study is based on an analytical description of the Newtonian and numerical simulations of the non-Newtonian flows.
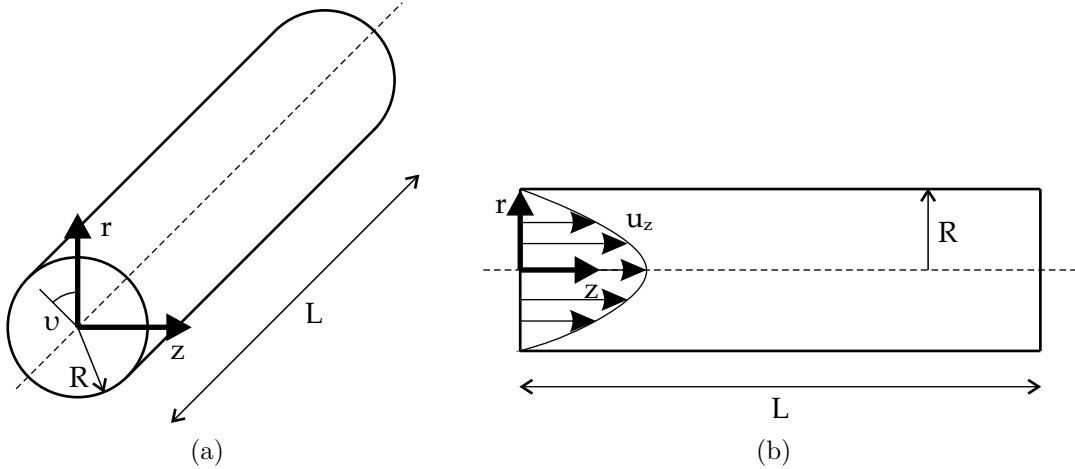
Figure 3.3.: (a) Geometry characterization of the flow domain and reference system, and (b) flow domain representation with inlet velocity profile at $t = 0$. Image re-adapted from Melito et al. [105].

The flow domain is a section of a straight pipe with a circular cross-section of constant diameter $2R = 25\,\text{mm}$. The section is 200R long. The symmetry axis of the pipe is the z-axis of a cylindrical coordinate system, as sketched in Fig. 3.3(a). The domain and the flow field are axisymmetric around the z-axis, i.e., there is no dependency on the polar angular coordinate denoted with the Greek letter υ. Numerically, the flow is nonetheless treated as three-dimensional.

3.2.3. Governing equations

The fluid flowing through the pipe is assumed to be incompressible, i.e., its density ρ is treated as constant. For this case, the mass balance is reduced to the requirement that the velocity field $\boldsymbol{u}$ is solenoidal, i.e.,

$$\nabla \cdot \boldsymbol{u} = 0 \; , \tag{3.9}$$

where ∇ is the nabla operator, $\nabla\cdot$ is the divergence operator. The vectorial momentum balance, or Navier-Stokes equation, reads

$$\rho \left[\frac{\partial \boldsymbol{u}}{\partial t} + (\boldsymbol{u} \cdot \nabla)\boldsymbol{u} \right] = -\nabla p + \nabla \cdot \boldsymbol{\tau} \; , \tag{3.10}$$

where body forces are neglected, $\boldsymbol{\tau}$ is, again, the shear, or deviatoric, stress tensor, and p is the pressure. The material derivative is expressed in the square brackets.

The rheological constitutive equation relates the deviatoric stress to the velocity field. In this formulation, two types of rheological behavior of the liquid are considered: a non-Newtonian inelastic and shear-thinning, on the one hand, and the Newtonian one on the other.
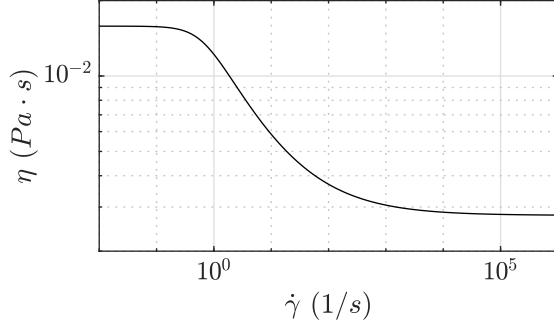
Figure 3.4.: Relationship between viscosity η and shear rate $\dot{\gamma}$ imposed by the Carreau model [35]

non-Newtonian inelastic shear-thinning - the Generalized Newtonian model   As the rheological constitutive equation for the non-Newtonian liquid, we select the Generalized Newtonian model given by Bird et al. [19] as

$$\boldsymbol{\tau} = 2\eta(\dot{\gamma})\boldsymbol{D}, \quad \dot{\gamma} = \left(2\mathrm{tr}(\boldsymbol{D}^2)\right)^{1/2} . \tag{3.11}$$

The shear rate $\dot{\gamma}$ is determined from the second invariant of the rate-of-deformation tensor $\boldsymbol{D}$ [26]

$$\boldsymbol{D} = \left(\nabla\boldsymbol{u} + (\nabla\boldsymbol{u})^{\mathsf{T}}\right)/2 , \tag{3.12}$$

with the velocity gradient $\nabla\boldsymbol{u}$. The dynamic viscosity $\eta(\dot{\gamma})$ as a function of the shear rate is represented by the Carreau model [35]

$$\eta(\dot{\gamma}) = \eta_{\infty} + (\eta_0 - \eta_{\infty})\left[1 + (\lambda\dot{\gamma})^2\right]^{(n_\eta-1)/2} , \tag{3.13}$$

which is known to represent shear-thinning liquid behavior well, see Fig. 3.4. In the model, η_0 represents the zero-shear viscosity, the first Newtonian plateau, and η_{∞} the limiting value of the viscosity for high shear rates, the second Newtonian plateau. λ and n_η are parameters determining the shape of the function $\eta(\dot{\gamma})$. In the specification of this function for the computational analysis, the four parameters are determined by fitting Eq. (3.13) to experimental data from blood rheometry and displayed in Tab. 3.1.

Special case of shear rate-independent viscosity - the Newtonian model   A Newtonian fluid has a shear rate-independent dynamic viscosity. Therefore its rheological constitutive equation reduces from Eq. (3.11) to

$$\boldsymbol{\tau} = 2\eta\boldsymbol{D} , \tag{3.14}$$

where η is the dynamic viscosity of the blood treated as Newtonian. A model well-established in the literature for determining the viscosity of blood as a function of the hematocrit for a

Table 3.1.: Model parameters of the rheological Carreau model.

	Value	Unit
η_0	1.581×10^{-2}	$\mathrm{Pa\,s}$
η_∞	2.779×10^{-3}	$\mathrm{Pa\,s}$
λ	1.561	s
n_η	0.475	-
ρ	1.060×10^3	$\mathrm{kg/m^3}$

Newtonian rheological model is due to Merrill [108] as

$$\eta = \eta_{\mathrm{pl}}\left[1 + 2.5H + 7.35H^2\right] \ , \tag{3.15}$$

where η and η_{pl} are the dynamic viscosity of blood and plasma, respectively, and H is the hematocrit represented as the volume fraction of red blood cells.

3.2.4. Initial and boundary conditions

Pulsating flow   In the numerical simulations, the flow is determined by a prescribed time-dependent volumetric flow rate and the corresponding velocity profile at the inlet of the pipe in Fig. 3.3(b). This profile is set parabolic at the inlet and evolves hydraulically in the flow direction z. The pipe section is long enough to ensure a fully developed state at the outlet $z = L$.

The corresponding heart rate is computed in beats per minute (bpm) by converting the frequency f from s^{-1} to min^{-1}. The boundary conditions for the velocity components $\boldsymbol{u} = [u_z, u_r, u_v]$ at the inlet are imposed in the following forms

$$u_z(r, z = 0, t) = \frac{2Q(t)}{A}\left(1 - \frac{r^2}{\mathrm{R}^2}\right) \quad r \in [0, \mathrm{R}] \tag{3.16a}$$

$$u_r(r, 0, t) = u_v(r, 0, t) = 0 \quad r \in [0, \mathrm{R}] \ , \tag{3.16b}$$

where A is the cross-section area of the pipe. The boundary conditions at the pipe wall represent the no-slip condition

$$u_z(\mathrm{R}, z, t) = u_r(\mathrm{R}, z, t) = u_v(\mathrm{R}, z, t) = 0 \quad \forall z, t \ . \tag{3.17}$$

The flow rate of the pulsating flow is composed of a steady component Q_{s} and a time-dependent component $Q_{\mathrm{o}}(t)$. The time dependence is sinusoidal, i.e.,

$$Q(t) = Q_{\mathrm{s}} + Q_{\mathrm{o}}(t) = Q_{\mathrm{s}} + \widehat{Q}_{\mathrm{o}} \cdot \sin(\omega t) \ , \tag{3.18}$$

where $\omega = 2\pi f$ is the angular frequency of the pulsation with frequency f for the period $T = 2\pi/\omega$, and $\widehat{Q}_{\mathrm{o}}$ is the flow rate pulsation amplitude. The volumetric flow rate equivalent velocity is given

as u_s and $\widehat{u}_\mathrm{o}$ is the volumetric flow rate equivalent pulsation amplitude given as

$$u(t) = \frac{Q(t)}{A} = u_\mathrm{s} + u_\mathrm{o}(t) = u_\mathrm{s} + \widehat{u}_\mathrm{o} \cdot \sin(\omega t) \ . \tag{3.19}$$

Steady flow The steady flow is the special case where all the properties of the flow are time-independent. The boundary conditions for the velocity components at the pipe inlet read

$$u_z(r, 0) = \frac{2Q_\mathrm{s}}{A} \left(1 - \frac{r^2}{\mathrm{R}^2} \right) \quad r \in [0, \mathrm{R}] \tag{3.20a}$$

$$u_r(r, 0) = u_v(r, 0) = 0 \quad r \in [0, \mathrm{R}] \tag{3.20b}$$

The steady-state no-slip conditions at the pipe wall are analogous to Eq. (3.17). For both the unsteady and the steady simulations, the pressure at the outlet $z = L$ was set to zero. The inlet pressure was obtained as a part of the solution to the flow problem.

3.2.5. Non-dimensional parameters

Sets of non-dimensional parameters govern the mechanical behavior of flowing fluids. The parameters are defined as quantities characterizing the flow and the fluid, such as characteristic velocities, length scales, and fluid material properties. For the present physiological context, the values of such parameters are known from the literature, such as flow velocity, pulsation frequency (heartbeat), vessel diameter, and blood viscosity. Successively, the values of the non-dimensional parameters are characterized in the uncertainty analysis.

The current flow is governed by the six parameters u_s, $\widehat{u}_o$, ω, R, ρ, and η. Given the three dimensions kg, m and s involved, these parameters form the three non-dimensional groups [105]

$$\mathrm{Re} = \frac{\rho u_\mathrm{s} 2\mathrm{R}}{\eta}; \quad \mathrm{Wo} = 2\mathrm{R}\sqrt{\frac{\omega \rho}{\eta}}; \quad \text{and} \quad \varphi = \frac{\widehat{u}_\mathrm{o}}{u_\mathrm{s}} \ , \tag{3.21}$$

where φ may be interpreted as the ratio of the corresponding flow rates, $\widehat{Q}_\mathrm{o}/Q_\mathrm{s}$, also.

The first non-dimensional group is the Reynolds number Re. It represents the ratio of convective to diffusive transport of momentum, with the volumetric flow rate equivalent velocity u_s, the diameter 2R of the pipe, and the density and dynamic viscosity of the fluid, ρ, and η, respectively. Defining the Reynolds number for fluids with variable viscosity requires special treatment. The form of the generalized Reynolds number in non-Newtonian flow proposed by Metzner and Reed [111] for a power-law fluid was re-derived for the present Carreau fluid to yield

$$\mathrm{Re}_\mathrm{gen} = \frac{u_\mathrm{s}^2 \rho}{\frac{3m+1}{4m} \left(\frac{u_\mathrm{s}}{2\mathrm{R}} \right)} \cdot \left[\eta_\infty + (\eta_0 - \eta_\infty) \left[1 + \left(\lambda \frac{3m+1}{4m} \left(8\frac{u_\mathrm{s}}{2\mathrm{R}} \right) \right)^2 \right]^{\frac{n-1}{2}} \right]^{-1} \ . \tag{3.22}$$

The coefficient m, which represents a logarithmic derivative of the pressure gradient to a representative shear rate, is calculated as

$$m = \frac{\eta_\infty + (\eta_0 - \eta_\infty)\left[\left[1 + (\lambda\dot{\gamma}_w)^2\right]^{(n-1)/2} + (\lambda\dot{\gamma}_w)^2(n-1)\left(1 + (\lambda\dot{\gamma}_w)^2\right)^{(n-3)/2}\right]}{\eta_\infty + (\eta_0 - \eta_\infty)\left[1 + (\lambda\dot{\gamma}_w)^2\right]^{(n-1)/2}} \; , \tag{3.23}$$

with the wall shear rate

$$\dot{\gamma}_{\mathrm{w}} = \frac{3m+1}{4m}\left(8\frac{u_{\mathrm{s}}}{2\mathrm{R}}\right) \; . \tag{3.24}$$

For each value of the generalized Reynolds number, m was iteratively calculated, starting from an initial value, calculating the wall shear rate from this value, and using this wall shear rate to calculate a new m, and so forth. This process was repeated until the difference between two successive values of m was below 1×10^{-4}.

The second non-dimensional group in Eq.s (3.21) is the Womersley number, representing the ratio of the time scale for diffusive momentum transport to the pulsation period. In the case of the non-Newtonian fluid model, the dynamic viscosity varies in the flow field. Therefore, for calculating the Womersley number, the kinematic viscosity is expressed using the generalized Reynolds number as [105]

$$\mathrm{Wo} = \sqrt{\frac{2\mathrm{R}\omega}{u_{\mathrm{s}}}\mathrm{Re}_{\mathrm{gen}}} \; . \tag{3.25}$$

The pulsating nature of the flow is represented by the non-dimensional group φ in Eq.s (3.21). Using this group, Eq. (3.18) transforms into [105]

$$Q(t) = Q_{\mathrm{s}}\left[1 + \varphi\sin(\omega t)\right] \; . \tag{3.26}$$

Different magnitudes of φ determine the flow as

$$\varphi = \frac{\widehat{u}_{\mathrm{o}}}{u_{\mathrm{s}}} \begin{cases} \ll 1 & \text{steady flow rate dominating} \\ \gg 1 & \text{oscillating flow rate dominating} \end{cases} \tag{3.27}$$

3.2.6. Models solutions

The solutions of the models are necessarily different depending on their linearity. In the case of a Newtonian fluid, which is linear, the solution is determined analytically. In addition, the symmetry of the geometry used is exploited in this formulation for both cases of flow, i.e., stationary and pulsating. The pressure in the system is determined by the volumetric flow rate imposed by the input domain. The equation for analytically calculating the velocity in the flow direction component u_z is determined following the work of Womersley [177] and is illustrated as follows

$$\frac{u_z}{u_{\mathrm{s}}}\left(\frac{r}{\mathrm{R}}, \frac{t}{T}\right) = 2\left(1 - \frac{r}{\mathrm{R}}^2\right) + \Re\left\{e^{j2\pi t/T}\frac{32j\widehat{p}^*}{\mathrm{Wo}^2}\left[1 - \frac{J_0\left(\frac{r}{\mathrm{R}}\sqrt{-j}\frac{\mathrm{Wo}}{2}\right)}{J_0\left(\sqrt{-j}\frac{\mathrm{Wo}}{2}\right)}\right]\right\} \; , \tag{3.28}$$

where $\Re$ represents the real part of the complex following term, J_0 is the Bessel function of the first kind and 0-th order, and $\widehat{p}^* = \widehat{p}/(\rho u_{\mathrm{s}}^2)$ is the normalized pressure amplitude.

In the case of non-linear material behavior, i.e., non-Newtonian fluid, the model requires a numerical solution. The model is solved in the open-source software OpenFOAM. Given the system's symmetry, the problem is solved on a cylinder wedge with an angular aperture of 5 degrees in the polar direction, see Fig. 3.3. After a sensitivity study on the convergence mesh, the wedge is formed by 1500 hexahedral and prism cells. The result is considered valid when the flow at the outlet is developed, i.e., its values do not change in subsequent time cycles. The flow is always laminar [105].

3.2.7. Uncertainty quantification and sensitivity analysis

Uncertainty and sensitivity analysis are fundamental steps in model building and they represent an important role in the decision making process that results from model simulations [31]. Sensitivity analysis is used to extract the information, rooted into computational models, about how much the uncertainty in the input factors affects the model output(s). Several methods are used to rank the most influential variables on a quantity of interest and to assess their level of interactions [81, 82]

A variance-based approach is used for the current study. In this case, the variance of the output is decomposed into a sum of contributions of the input space [158]. Since knowledge regarding the model is limited, in the sense that it is unknown whether its behavior can be linear, additive, monotonic, or none of them, the choice of a variance-based approach is suitable.

For the estimation of the Sobol indices as quantitative measures for the SA, a surrogate model construction is employed, namely the polynomial chaos expansion. Alternatively, the use of Monte Carlo sampling or quasi-Monte Carlo sequences are adopted, but the cost of this computation is still affected by the high number of model calls [81, 105].

3.3. Application

SA is applied to the coupled model that solves the rheology of blood first, as described in Sect. 3.2.2, and the electrical conductivity of flowing blood. as mentioned in Sect. 3.2.1. The uncertainty sources in the present study are generated by both the physiological variability of the human body and the variation of data collected from model assumptions. Physiological parameters, such as aortic flow rate Q_{s} and corresponding flow rate ratio φ, blood hematocrit H and density ρ, and heart rate f, present significant probability distribution variation [64, 73, 74, 88, 108, 113]. Moreover, through literature research on the models that emulate the electrical conductivity of blood, it has been noticed that some of the input parameters vary substantially among different authors, i.e., the RBCs axes ratio a_0/b_0, the electrical conductivity of plasma σ_{pl} [64, 65, 170], and viscosity of plasma η_{pl} [64, 88]. A uniform probability distribution function for all random variables is considered, due to the lack of prior information on their real probability distributions.

Table 3.2.: Input parameters of the model and their probability distribution properties used for sensitivity analysis.

	Notation	$p(x_i)$	Unit	Reference
Volumetric flow rate	Q_{s}	$\mathcal{U}[0.000\,032, 0.000\,182]$	$\mathrm{m^3/s}$	[113]
Flow rate ratio	φ	$\mathcal{U}[0.1, 1]$	-	[113]
Blood density	ρ	$\mathcal{U}[1050, 1060]$	$\mathrm{kg/m^3}$	[64, 73, 74, 88]
Hematocrit level	H	$\mathcal{U}[0.30, 0.70]$	-	[108]
RBCs axes ratio	a_0/b_0	$\mathcal{U}[0.11, 0.40]$	-	[64, 65, 170]
Plasma conductivity	σ_{pl}	$\mathcal{U}[1.12, 1.57]$	$\mathrm{S\,m^{-1}}$	[64, 65, 170]
Viscosity of plasma	η_{pl}	$\mathcal{U}[0.0011, 0.001\,55]$	$\mathrm{Pa\,s}$	[64, 88, 108]
Heart rate	f	$\mathcal{U}[50, 100]$	$\mathrm{min^{-1}}$	[100, 163]
Trigger	trigger	[1, 2 or 3]	-	[62, 64, 76, 170]

Furthermore, this assumption allows to better emphasize the randomicity of different patient-specific cases. The ranges of the distributions, shown in Tab. 3.2, highlight the uncertainty that afflicts medical research. Their variation aims at producing different responses of the models and at analysing their influence through such models using a sensitivity analysis technique.

Different model assumptions are the basis of the sensitivity analysis to understand the importance of such hypotheses when computing the conductivity of blood. One of the questions that arose in the development of this study is: how complex should the fluid model be to give a reliable output of electrical conductivity change of flowing blood? Often models tend to simplify the fluid mechanics of the problem to avoid complexity and to reduce the computational effort. Therefore, it is the interest of this study to evaluate and quantify the importance of such choices concerning the evaluation of the conductivity of blood. The last random variable in Tab. 3.2, discretely distributed and referred to as the *trigger*, is used to analyse the differences in the output considering different model assumptions:

1. Newtonian fluid and steady flow
2. Newtonian fluid and pulsating flow
3. non-Newtonian fluid and pulsating flow

The experimental design is built so to explore the model's input space. The variability of the input space is also meant to simulate the randomicity of everybody's health condition and characteristics. It is therefore essential to analyse the functioning of different model assumptions in relation to the randomness of their corresponding input domain, see Tab. 3.2. In order to assure the physiological ranges of the flow parameters with respect to the rheological parameters of the human body in modelling hemodynamics [154], the ranges of non-dimensional numbers characterising the flow are calculated and depicted in Fig. 3.5, namely the Reynolds and the
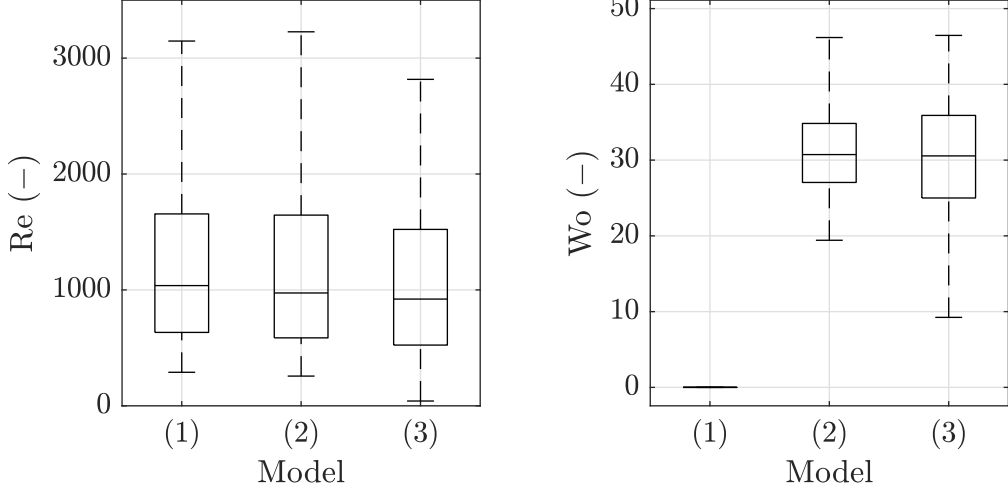
Figure 3.5.: Boxplot visualization of the distributions of (left) Reynolds Re and (right) Womersley Wo numbers computed for each model assumption: 1 Newtonian-steady, 2 Newtonian-pulsating, and 3 non-Newtonian-pulsating.

Womersley number.

Due to the Reynolds number distributions, see Fig. 3.5 left, the flows could be considered, with good approximation, to be laminar for all the three model assumptions. Blood flow generally exhibits laminar flow under ideal conditions [40]. To confirm such an assumption, different values are found in the literature regarding the Reynolds number's threshold value that confirms the laminar behavior of blood. However, Re values below 2000 confirm, in general, the laminar flow of blood [52, 112]. Thus, given that most of the distribution is below such value, the flow is considered laminar. Higher values of Re, up to 3000, denote a transient flow, which is easily detectable in the aorta [12]. In the aorta, Re is usually higher due to the vicinity of the heart (pump). Hence, Re average values is 2500, and peaks values are up to 7500 [112]. The Womersley number distribution, see Fig. 3.5 right, also shows good agreement with the usual variation of values detected in the physiology of the cardiovascular system [68], although slightly higher due to imposed model variation.

The conductivity change relative to stationary blood, as in Eq. (3.8), was determined to assess the QoI, as expressed next. In particular, given its variability over one cardiac cycle, its average value in time over the period is taken into account

$$\langle \Delta\sigma_{\mathrm{bl}} \rangle = \frac{1}{T} \int_0^T \Delta\sigma_{\mathrm{bl}} \mathrm{d}t \ . \tag{3.29}$$

where T is the assumed heart cycle.

The reason for this choice is that such output holds more useful information about the behavior of conductivity of blood over time. More importantly it is mostly used in the related scientific literature, instead of considering the conductivity of blood per se. The peak-to-peak amplitude of

(a) ε_{LOO} of the PCE for model assumptions 2 and 3.

(b) ε_{LOO} of the PCE for SA among the three model assumptions.
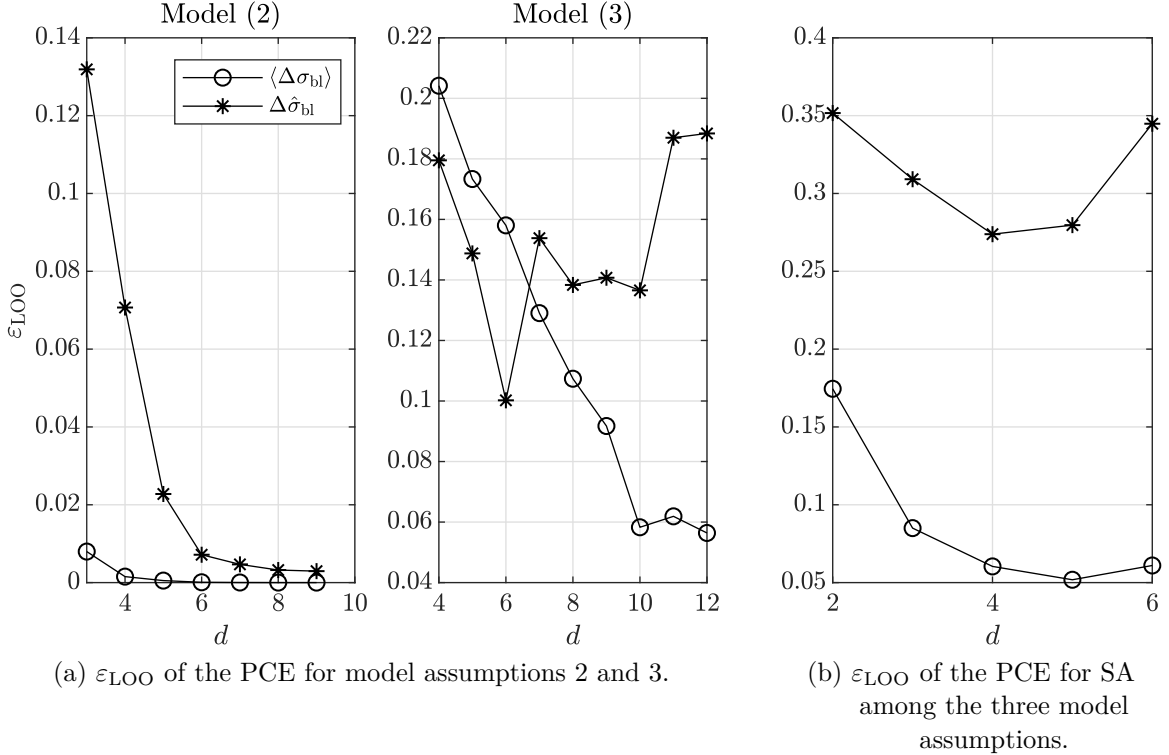
Figure 3.6.: The leave-one-out error for the $\langle \Delta \sigma_{\text{bl}} \rangle$ is indicated with the star marker (*), while for $\Delta \hat{\sigma}_{\text{bl}}$ with the circle marker (o).

such signal over one cardiac cycle, referred as $\Delta \hat{\sigma}_{\text{bl}}$, is also considered to be of interest to analyse the models' mechanics.

Two different sensitivity analyses have been performed. The first one is a sensitivity analysis *within* each model assumption, i.e., model 1, 2 or 3, to better understand their functioning and mechanics. This analysis is performed with a different sample size N_s of the input space, with the dimension $M = 8$, given that the trigger variable is considered constant for such computation. The high computational expenses of model assumption 3, i.e., non-Newtonian fluid and pulsating flow, constrains the number of performed simulations to $N_{s_3} = 500$. For trigger equal 1 or 2, the sample size is $N_{s_{1,2}} = 10\,000$ due to the availability of the analytical formulation for the fluid mechanics, which reduces the computational costs.

The second sensitivity analysis is then performed *among* the model assumptions and with the input space of dimension $M = 9$, since the last factor in Tab. 3.2 is assumed as a random variable. For this analysis, the number of simulations is $N_s = 1500$, so that each model assumption is run an equal amount of times.

The two sensitivity analyses, are computed from two different polynomial chaos expansions. The surrogate for the analysis within each model assumption is resolved with ordinary least square method (OLS) [17, 18] for the models 1 and 2, given the low computational costs. For

model 3, due to the limited resources, the least-angle regression (LARS) method [24] is selected. The degree of each expansion is selected at the minimum of the Leave-One-Out error ε_{LOO} [23, 94] produced for different polynomial degrees. Therefore, as visible in Fig. 3.6(a), degree 7 is chosen for both QoIs in model 2. Although ε_{LOO} already reach a good value for $d = 6$, the degree 7 will increase the quality of the surrogate and does not affect the computational burden. As for model 3, PCE is truncated at degree 10 for the cycle average $\langle \Delta\sigma_{\text{bl}} \rangle$, and at degree 6 for the amplitude $\Delta\hat{\sigma}_{\text{bl}}$. OLS method is selected for the sensitivity analysis among the model assumptions and the polynomial is truncated at degree 4, see Fig. 3.6(b). A PCE degree smaller than M suggests the exclusion in the PCE of some interaction terms. However, the employed basis-adaptive strategy detects and deletes negligible high-order interaction terms, reducing the dimensionality of the truncated polynomial expansion [24, 98].

The *trigger* variable is included in the construction of the polynomial chaos expansion upon transformation into a uniformly distributed variable. Nonetheless, such transformation does not affect the accuracy of the surrogate model. By evaluation of the accurate PCE, a Monte Carlo method is chosen for the estimation of the Sobol indices among the model assumptions, see Eq.s (2.30) and (2.31).

3.4. Results and discussion

Uncertainty analysis After performing the simulations for each model assumption, a first check on the reliability of the results was performed. In Fig. 3.7, the box plots of the cycle average of the conductivity change of blood $\langle \Delta\sigma_{\text{bl}} \rangle$ (left) and its amplitude $\Delta\hat{\sigma}_{\text{bl}}$ (right) are shown.

An overview of the distribution of the results of the QoIs is necessary to analyse the behavior of different model assumptions and differences in their mechanics. Here, the distribution of the cycle average of the blood conductivity change of the model assumption 1 (see Fig. 3.7 left, model 1) shows inaccurate results. Its distribution is characterised by a median value slightly larger than zero and by a prolonged negative tail. As visible, such results are inaccurate in expressing the increment of conductivity of flowing blood. Theoretically, during the flow condition, RBCs are oriented and deformed by the shear rate. The steady flow assumption has been developed for the computation of the electrical conductivity of blood, given its simplicity and easiness in implementation. Results of its use are also compared to experimental results [76]; however, those comparisons stand only for a few particular cases and combinations of the input domain. Thus, since most of the distributions of the conductivity change $\Delta\sigma_{\text{bl}}$ are below the zero value, model 1 indicates the inability of the steady flow assumption in computing such QoI, given the variability of the input parameters. Furthermore, due to the steadiness of the flow, the amplitude of the conductivity change of blood is absent, which stresses the inability of such assumption in emulating the nature of such measurement. As a consequence, the steady flow model assumption is not considered for the following sensitivity analysis.

The results for model assumptions 2 and 3 are not only comparable, but also more realistic when compared to the real behavior of the $\Delta\sigma_{\text{bl}}$ signal. In previous deterministic models [62–64], $\Delta\sigma_{\text{bl}}$ is shown to oscillate between $10\,\%$ and $20\,\%$. Lack of previous studies on the variation of
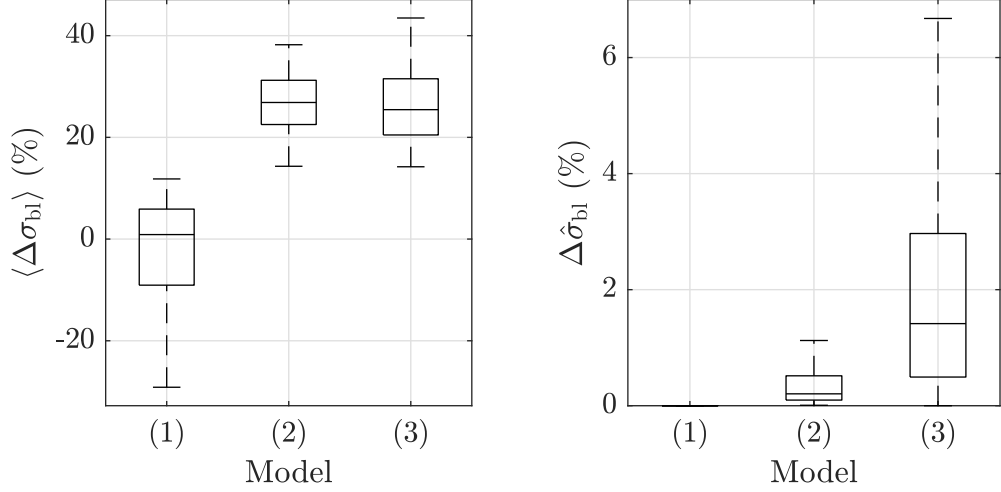
Figure 3.7.: Box plots of the cycle average of conductivity change of blood (left) and its peak-to-peak amplitude (right) for the three model assumptions: (1) Newtonian-steady, 2 Newtonian-pulsating, and 3 non-Newtonian-pulsating.

such outputs for different fluid and flow assumptions lead to the the conclusion that the present results are valid. The distributions of $\langle\Delta\sigma_{\mathrm{bl}}\rangle$ show good agreement both in the median value and the tail of the distributions. Regarding the distribution of the amplitude of conductivity change $\Delta\hat{\sigma}_{\mathrm{bl}}$, see Fig. 3.7(right), the assumption of a non-Newtonian fluid highly increases the variability of this QoI. Such a phenomenon has to be further investigated through a sensitivity analysis among the models, with a particular interest in the output $\Delta\hat{\sigma}_{\mathrm{bl}}$. Nonetheless, both distributions show good agreement with the nature of the $\Delta\sigma_{\mathrm{bl}}$ signal, and are therefore considered as reliable results [62–64].

For the sake of completeness, the results of the pulsating flow models are shown in Fig. 3.8. Here, the average trends over the simulations of the conductivity change of blood, both for the Newtonian and non-Newtonian fluid in pulsating flow, are plotted over a normalized cardiac period. Noticeable is the similarity of expressing the delay in decelerating when compared to the input sinusoidal wave of the volumetric flow rate (3.2.4), as researched in [64].

Sensitivity analysis Before proceeding with the sensitivity analysis, an investigation of the behavior of the model is performed with the use of a scatter plot, see Fig. 3.9, where the input parameters are projected in turn against the two QoIs. Here, the grey color represents the use of the model 2 assumption, while the black one refers to model 3. Furthermore, the input space is normalised with respect to their input domain and $\Delta\hat{\sigma}_{\mathrm{bl}}$ is represented in log scale for better visualisation.

The scatter plots show that $\langle\Delta\sigma_{\mathrm{bl}}\rangle$ is more sensitive to the variables hematocrit H and the RBCs axes ratio a_0/b_0, which display a strong linear relationship in both model assumptions. In
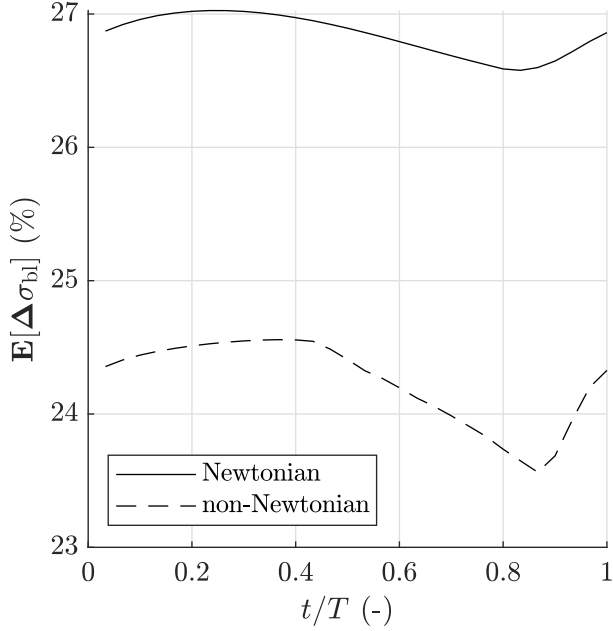
Figure 3.8.: Conductivity change of blood in time averaged over the simulations for a Newtonian (continuous line) and non-Newtonian fluid (dashed line), both in a pulsating flow model assumption.

addition, the volumetric flow rate Q_s for model 2 also shows a linear trend, but all the other input factors do not exhibit particular influence. As for the amplitude of the conductivity change of blood $\Delta\widehat{\sigma}_{bl}$, a clear difference behavior between the two model assumptions is visible. In model 2, variables such as hematocrit H, volumetric flow rate Q_s and flow rate ratio φ demonstrate a higher influence on $\Delta\widehat{\sigma}_{bl}$. In model 3 however, while H seems to maintain its impact on this output, Q_s influence decreases. Instead, the flow rate ratio φ shows a new strong linear trend. The output $\Delta\widehat{\sigma}_{bl}$ is also equally influenced by the RBCs axis ratio a_0/b_0 for both model assumptions.

The difference in output domain coverage for $\Delta\widehat{\sigma}_{bl}$ when switching from model 2 to model 3 is significant, see Fig. 3.9 bottom row. All the input variables show an exponential behavior, apart from φ in model 3, which suggest the presence of a higher level of interactions than for the output $\langle\Delta\sigma_{bl}\rangle$. The use of scatter plots aids in identifying influential parameters, however it can be deceiving and lead to refutation of influential parameters [143]. This motivates the use of a variance-based sensitivity analysis and the computation of Sobol' indices.

Sensitivity analysis results are plotted in Fig. 3.10. The top two figures refer to the first- and total-order Sobol' indices on the cycle average of the blood conductivity change $\langle\Delta\sigma_{bl}\rangle$ for models 2 and 3. In contrast, on the bottom, the indices refer to the amplitude of blood conductivity change $\Delta\widehat{\sigma}_{bl}$.

Regarding the first-order sensitivity indices S_i of the output $\langle\Delta\sigma_{bl}\rangle$ (top figures in Fig. 3.10), the ranking of the most influential factors is similar for both model 2 and 3 having the hematocrit value of blood H as the most important one, followed by the RBCs axes ratio a_0/b_0 and the volumetric flow rate Q_s. The hematocrit value is the volume fraction of RBCs in the blood, thus
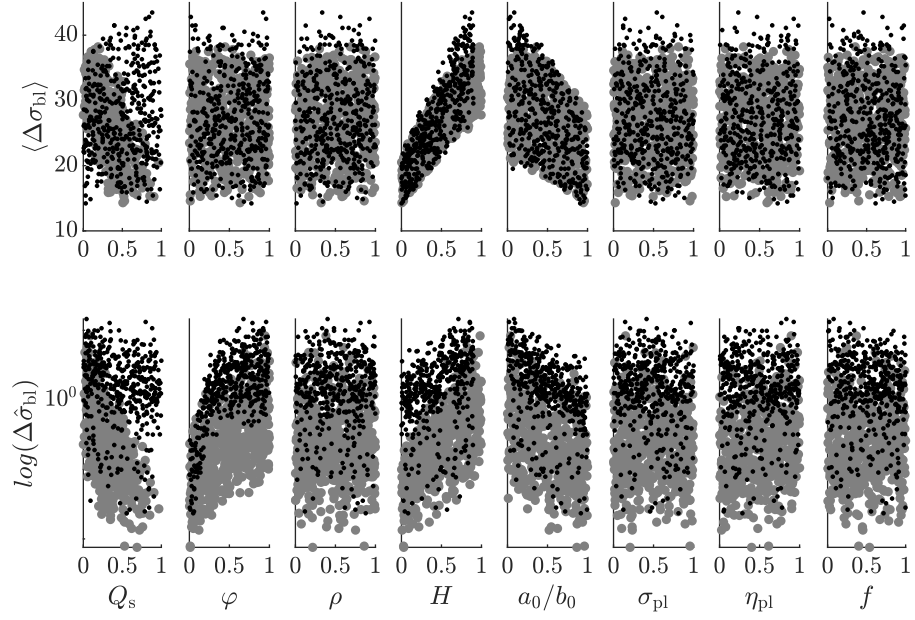
Figure 3.9.: Scatter plot of the two quantities of interest, cycle average of change of blood conductivity $\langle\Delta\sigma_{\mathrm{bl}}\rangle$ and its amplitude $\Delta\hat{\sigma}_{\mathrm{bl}}$, versus the model input parameters, normalised in their domain (Tab. 3.2). The third dimension, the color, represents different model assumptions: grey for model 2 and black for model 3.

proportional to the number of RBC, which are considered to be non-conductive for the electrical signal. The electrical signal follows the path with less resistance; indeed, it is eased by fewer RBCs or by many oriented and deformed cells. This result confirms the influence on the mean value in time of the $\Delta\sigma_{\mathrm{bl}}$ of both the hematocrit value H and the RBCs axes ratio a_0/b_0 before the deformation of such cells takes place.

The interaction effect is estimated by the difference between the first- and total-order sensitivity indices. An analysis of the total-order Sobol indices S_i^{T} of the same output, highlights the presence of low interactions between the parameters; thus, the model could be considered additive in the output $\langle\Delta\sigma_{\mathrm{bl}}\rangle$. Secondly, S_i^{T} drives the discussion in considering variables as constant values for the model, i.e., applying the Factor Fixing setting, since any variation in their value will not affect the considered model's response. Such variables are the viscosity of plasma η_{pl}, the conductivity of plasma σ_{pl}, the flow rate ratio φ, the heart rate f, and the blood density ρ.

Different behavior is shown for the sensitivity analysis on the amplitude of blood conductivity change $\Delta\hat{\sigma}_{\mathrm{bl}}$, see Fig. 3.10 bottom figures. Model 2 (left picture) confirms that the hematocrit value H gives the principal influence on the output, followed by the volumetric flow rate Q_{s}. Such influence is explained by the presence of H in Eq. (3.15) for the computation of the viscosity of blood, and in Maxwell-Fricke theory Eq. (3.3). Both equations form the basis for calculating the blood conductivity and the fluid mechanical model, so affecting the shear rate of the flow and then the RBCs deformation. To be noticed is also the increment in interaction terms in the model
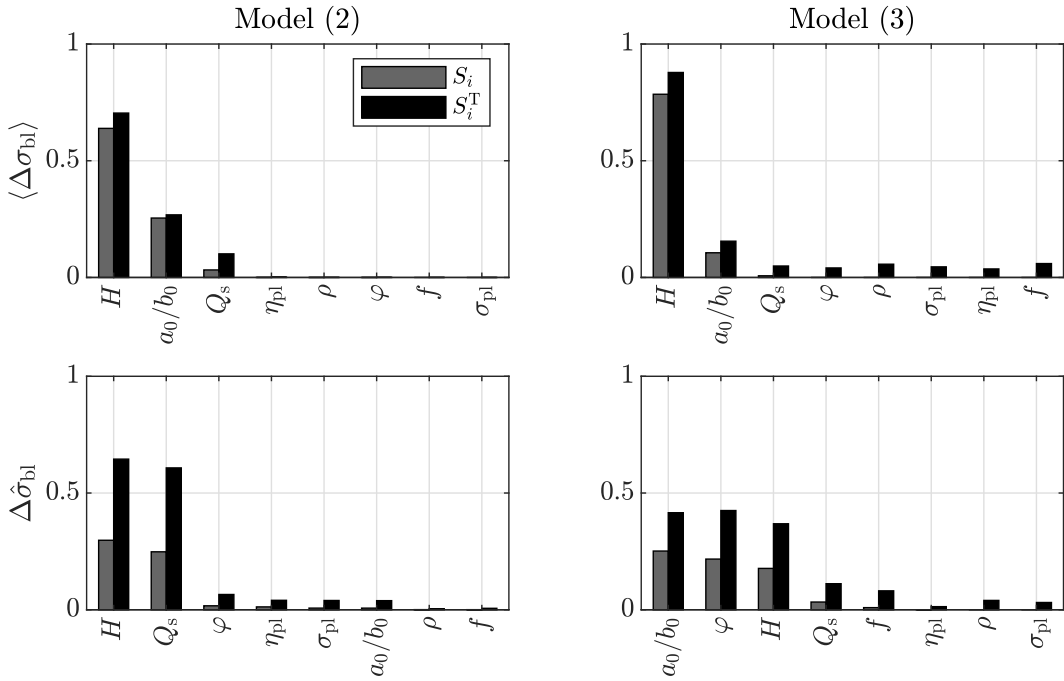
Figure 3.10.: Sensitivity indices on the cycle average value (top) and amplitude (bottom) of the conductivity change of blood $\Delta\sigma_{\mathrm{bl}}$ for model 2 (Newtonian-pulsating) and model 3 (non-Newtonian-pulsating). The grey bars represent the first-order sensitivity index; the black bars the total-order sensitivity index. The variables, listed in Tab. 3.2, are sorted by first-order sensitivity index.

3. On electrical conductivity of flowing human blood
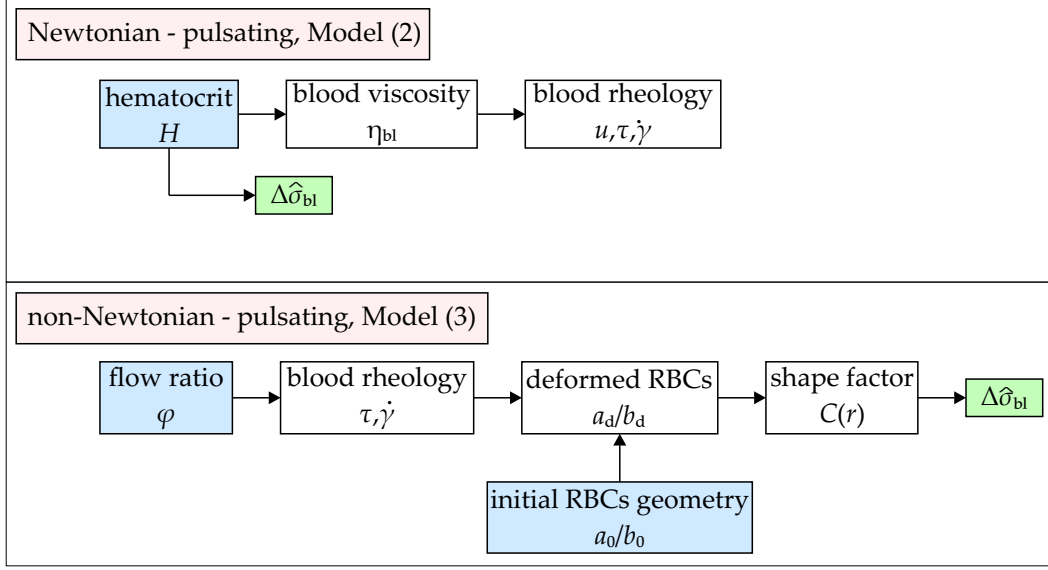
Figure 3.11.: Visualization of the models mechanics in computing the amplitude of the conductivity of flowing blood for Model(2) and Model(3), respectively Newtonian-pulsating and non-Newtonian-pulsating assumptions. The input variables are highlighted in blue and the output in green. It is evident that the non-Newtonian formulation introduces significant changes.

for this particular output, contrary to what was discussed for $\langle\Delta\sigma_{\mathrm{bl}}\rangle$, see Fig. 3.10 left-top.

By looking at the sensitivity analysis results for the non-Newtonian fluid model, Fig. 3.10 right-bottom, it is clear how the mechanics for the computation of the electrical conductivity is altered. Here, the highest first-order sensitivity indices are recorded in the flow rate ratio φ, and in the RBCs axes ratio a_0/b_0. Also, the hematocrit level H shows a high influence on the model's QoI, but its value is not the highest recorded. The reason for such change of mechanics has to be found in the change of formulation between the Newtonian and the non-Newtonian fluid models. In the non-Newtonian formulation, the viscosity model of Merrill et al. [109] of Eq. (3.15) is not implemented, given the non-linearity of the viscosity model. Therefore, other factors act on the variation of the flow shear rate $\dot{\gamma}$ and resulting shear stress τ. In particular, the flow rate ratio φ, as defined in Eq. (3.27), directly influences the shear rate in the flow, and further affects the RBCs deformed configuration in Eq. (3.2). Besides, the undeformed configuration of the RBCs a_0/b_0 is as crucial as φ in the final computation of the amplitude of blood conductivity change $\Delta\hat{\sigma}_{\mathrm{bl}}$. Finally, once the deformation of the RBCs has taken place, the $C(r)$ factor of Eq. (3.3) is consequently affected. This change in model mechanics is shown in Fig. 3.11 for both models (2) and (3).

The sensitivity analysis among the model assumptions is presented in Fig. 3.12. Again, the left part of the figure represents the first- and total-order sensitivity indices of the cycle average of the blood conductivity change $\langle\Delta\sigma_{\mathrm{bl}}\rangle$. In contrast, the right picture refers to the amplitude of blood conductivity change $\Delta\hat{\sigma}_{\mathrm{bl}}$. As expected, the change of the model assumptions affects both
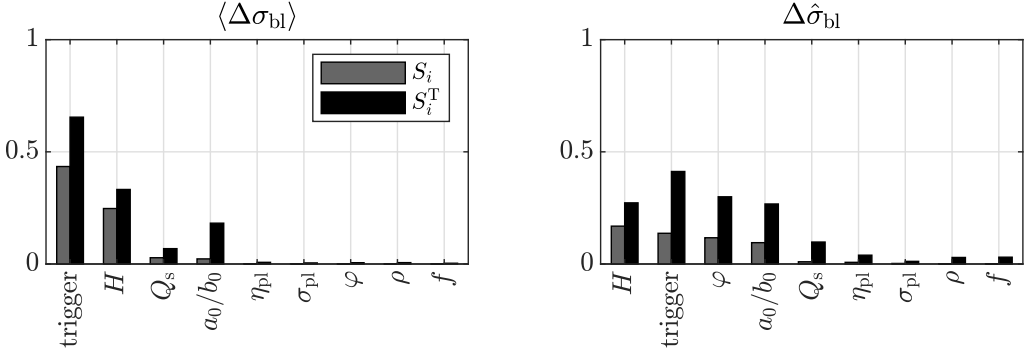
Figure 3.12.: Sensitivity indices of the global analysis between different model assumption on the mean value of blood conductivity change (left) and on its amplitude (right). The variables, listed in Tab. 3.2, are sorted by first-order sensitivity index.

outputs largely, since the trigger factor has the highest first-order sensitivity index. These results stress the need for a clear identification of the model that is used for the computation of both QoIs. However, although the trigger's first-order sensitivity index S_i is dominant on the other indices for the computation of $\langle \Delta\sigma_{\mathrm{bl}} \rangle$, the first Sobol' index of the same input random variable has a much lower value for the amplitude of $\Delta\sigma_{bl}$. Furthermore, its value shares a similar value to the indices of the blood hematocrit level H.

When computing the amplitude of blood conductivity change, the model shows a high interaction between the input random variables, as it is visible by the higher values of S_i^T in Fig. 3.12(right) with respect to the S_i. This translates in non-additive model behavior, besides being non-linear. However, such high interaction effect seems to disappear when it is about the QoI $\langle \Delta\sigma_{\mathrm{bl}} \rangle$.

4. On configuration optimization of simulated thoracic bioimpedance

In this chapter, a study on impedance cardiography (ICG) is employed. ICG, also known as thoracic bioimpedance, is a standard tool that measures volumetric changes in the thorax by applying alternate current injected through sensors in contact with the patients. It is a noninvasive technique, and therefore convenient for both patients and physicians. Nowadays, its use in cardiology is advanced since it allows the measurement of cardiac output (CO), stroke volume (SV), heart rate, and many more parameters. NASA initially developed it in the 1960s, but modern technological advances allow its use on many more applications [36].

As analyzed in the previous chapter, the variation of electrical conductivity of flowing blood σ_{bl} is easily obtained. Indeed, different model assumptions and input variations lead to highly different scenarios. However, the work presented in this chapter anticipates such conclusions and examines the effect of electrical conductivity uncertainties on ICG applications, in particular, when AD develops.

Here, ICG is employed as a tool for the detection of AD. Given the human variability of physiological parameters discussed in the previous chapters, the configuration of the electrical sensor for an ICG measurement is uncertain. Therefore, a study on geometrical optimization of the position of the sensors based on surrogates and sensitivity analysis is produced.

The ICG model described here has been the subject of many studies so far [10, 11, 134, 135]. Preliminary work was conducted by Melito et al. [102], in which two different SA methods were applied to deal with high dimensional computational model. This work will serve as an introduction to Badeli et al. [10], which will be the main focus of this chapter. In summary, the reported work is mainly based on the works of Melito et al. [102], and Badeli et al. [10].

4.1. Introduction

The formation of TBAD is commonly initiated by the dilatation of the aorta or high blood pressures that tear the intima, allowing blood to flow into the aortic wall. The pulsatile pressure of the circulation then drives the blood. It separates the aortic wall layers, resulting in a true lumen TL and a false lumen FL.

Detecting TBAD can be difficult because the symptoms are similar to those of various health problems. Ultrasound scanning (sonography), magnetic resonance imaging, and computerized tomography are expensive techniques currently used for this purpose, with experts needed to

4. On configuration optimization of simulated thoracic bioimpedance

read and interpret the images. Nevertheless, an easy-to-use and still reliable method for pre-identification of TBAD would be beneficial. Furthermore, tracking the development of the disease, such as FL expansion and FL thrombosis, can be very helpful for the medical management of TBAD.

The presence of a FL alters the aortic hemodynamics and changes the thorax tissue distribution. These changes can be identified and quantified by bioimpedance techniques such as ICG. In ICG, a current field longitudinally across a thorax segment is applied using a constant low magnitude and high-frequency alternating current. It is a non-invasive, safe, easy to use, and low-cost method for measuring several cardiodynamic parameters (e.g., the stroke volume and the cardiac output) continuously [5]. Besides, this method is portable, and the analysis could be automated.

Impedance changes can be evaluated during a cardiac cycle by injecting a low-amplitude alternating current into the thorax and measuring the voltage drop ΔV on the thorax. The negative of the first-time-derivative impedance signal $-|\mathrm{d}\underline{Z}/\mathrm{d}t|$ is known as the impedance cardiogram. Since the conductivity of the blood-filled aorta is much higher than that of the surrounding tissue types, the measured impedance changes are strongly related to changes in the aorta. An alteration of blood volume and flow occurs in TBAD, leading to an irregular impedance cardiogram. Thus, ICG results to be a good candidate for diagnosis and monitoring purposes [11, 134, 135]. A 3D numerical simulation model is used to compute the impedance changes on the thorax surface in the case of the TBAD.

4.2. Preliminary assessment of sensitivity parameters

A proof of concept study is illustrated here to assess the method's validity and optimize the electrode configuration. However, the amount of encountered uncertainties in the construction of the model is significant. A visualization of the model geometry is represented in Fig. 4.1(a).

The first question that arise in the construction of this model is the geometrical configuration. The aortic system is different for each human. Therefore the aortic arch and TL radii, namely R_A and R_{TL}, may vary significantly among the population. Other geometrical uncertainties included the radius of the FL R_{FL}, which fluctuates depending on TBAD progression, and the position of such secondary volume with respect to the TL. The latter uncertainty is included as the angle between the x-axis and the center of the idealized FL cross-section and named α_{FL}, see Fig. 4.1(b). A radius multiplier models the variation of the TL radius so that the radius enlargement in time is as in Fig. 4.3. These factors are therefore grouped s.t. their variation affects only the geometrical configuration of the model.

The second group of uncertainties regards the physical and electrical fields. First, the blood velocity is considered with a 50% variation from the reference assumption, as in Fig. 4.4. Next, the hematocrit of the blood H and the electrical conductivity of flowing blood σ_{bl} and thorax σ_{th} are also considered as system variables. All the parameters lack enough knowledge regarding their mean value and PDF. So, they are assumed to be distributed uniformly, see Tab. 4.1, whose values are found in the literature.

The analysis of eight input parameters is performed on a 3D FEM model developed in COMSOL
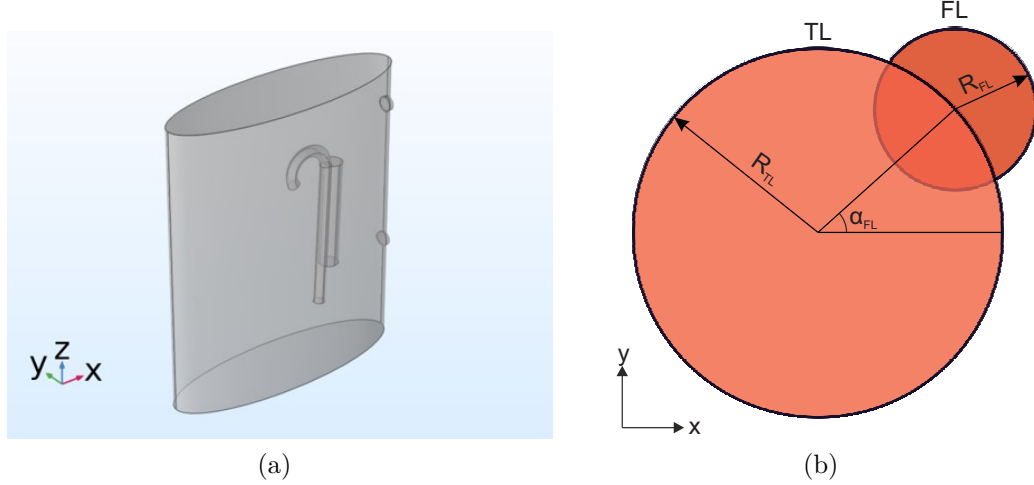
Figure 4.1.: (a) Aortic system in the thorax modeled in COMSOL$^{\text{TM}}$ and (b) schematic positioning of the FL with respect to the TL. Figure readapted from Badeli et al. [10].

Multiphysics$^{\text{TM}}$, which will be described in the following sections and by Reinbacher-Köstinger et al. [134]. Two sensitivity analysis methods have been applied: the EE and the variance-based methods with PCE as surrogate models. Such choice is motivated by the struggle that the PCE brings when dealing with many input variables. Therefore, a first screening of the input space is performed by the EE method. The result will highlight the most sensitive factors of the model. A PCE is then built for those factors, and the sensitivity indices in Eq.s (2.56) and (2.57) are computed. This work has been inspired by the work of Donders et al. [45].

In the EE method, the input parameters are divided into geometric (rows 1 to 4 in Tab.4.1) and physical parameters (rows 5 to 8 in Tab.4.1). The first group is made of the radius of the aortic arch R_A, the radius of the FL R_{FL}, a multiplier for the radius of the aorta m_r, and the relative position of the dissection with respect to the TL α_{FL}. The second group includes the multiplier of the blood velocity in the aorta m_v, the hematocrit percentage in the blood of the patient H, the conductivity of the blood σ_{bl} and the conductivity of the thorax σ_{th}. The computed output for the analysis is the impedance cardiogram signal $-|\mathrm{d}\underline{Z}/\mathrm{d}t|$ between the measurement sensors, as visualized in Fig. 4.1(a). The output formulation is left to the later sections.

The EE evaluation, based on $N_{EE} = 80$ trajectories and therefore $N_s = 720$ simulations, shows that parameters 2, 3, 4, and 8 have the most significant value of $\check{\mu}^*$ and $\check{\sigma}_i$. Consequently, they are considered for the surrogate model construction. The latter has been performed from $N_s = 1000$ sampling generated from LHS technique. The metamodel is truncated up to degree 6. From the PCE construction, the Sobol indices S_i and S_i^{T} are computed.

In conclusion, coupling the two methods allows a better and simplified construction of the metamodel. Furthermore, more investigation should be performed on the conductivity of the thorax σ_{th} given its high value of S_i among the second input parameter group. The geometry of the FL is shown to be more influential than the geometry of the TL. By reducing the number of a

Table 4.1.: Sensitivity analysis results of the model's input random variables. Inputs variables names are in column (1) and their variability is shown in column (2). Results from the EE method are shown in columns (3) to (5); Sobol sensitivity indices are in columns (6) and (7). Table readapted from Melito et al. [102].

	$p(x_i)$	$\breve{\mu}_i$	$\breve{\mu}_i^*$	$\breve{\sigma}_i$	S_i	S_i^{T}
(1)	(2)	(3)	(4)	(5)	(6)	(7)
$\mathrm{R_A}$	$\mathcal{U}[38, 42]$	-4.33×10^{-6}	3.34×10^{-5}	1.75×10^{-9}	-	-
$\mathrm{R_{FL}}$	$\mathcal{U}[0, 30]$	-2.84×10^{-3}	2.88×10^{-3}	4.63×10^{-4}	0.650	0.676
m_{r}	$\mathcal{U}[0.95, 1.25]$	8.80×10^{-7}	4.57×10^{-5}	3.41×10^{-9}	0.005	0.002
α_{FL}	$\mathcal{U}[\text{-}\pi/3\ \pi/3]$	5.19×10^{-7}	4.60×10^{-5}	3.88×10^{-9}	0.174	0.274
m_{v}	$\mathcal{U}[0.5, 1]$	1.19×10^{-8}	1.85×10^{-8}	7.92×10^{-15}	-	-
H	$\mathcal{U}[0.37, 0.54]$	-3.85×10^{-9}	8.75×10^{-9}	1.83×10^{-15}	-	-
σ_{bl}	$\mathcal{U}[0.5, 0.7]$	-2.86×10^{-9}	6.04×10^{-9}	3.82×10^{-16}	-	-
σ_{th}	$\mathcal{U}[0.08, 0.13]$	1.43×10^{-2}	1.11×10^{-1}	1.27×10^{-2}	0.168	0.047

random variable, the model still appears to represent a noticeable difference in the measurement in the presence of TBAD. Indeed, from the results illustrated in the table, $\mathrm{R_{FL}}$ appears to be extremely sensitive to the results, confirming the validity of the model in detecting variation in blood volumes.

This analysis highlighted four parameters as the most sensitive for the illustrated model. In the following sections, model complexity is increased by including lungs and heart in the thoracic geometry. The analysis of this second model aims to identify the optimal configuration of electrodes for ICG measurements. The system variables selected are those resulting from this preliminary study. However, the thoracic conductivity will be considered constant and the hematocrit as a variable. This choice is motivated by the difficulty encountered in defining the exact variation of the thoracic conductivity. This process is visualized the schematics in Fig. 4.2.

4.3. Methods

Model complexity increases due to modeling new elements in the thorax, such as the heart and lungs. This section will illustrate the methods and assumptions assumed in this new modeling phase. After illustrating the methods considered in modeling thoracic impedance, the use of SA as a tool to determine the optimal electrode configuration will be motivated.

A global sensitivity analysis technique is applied to investigate different electrode configurations in the simulation model with different input parameters to cover as many patient-specific cases as the dimension of the input space. The final aim is to find the desired electrode configuration, which gives the highest difference between the impedance cardiograms of the healthy condition
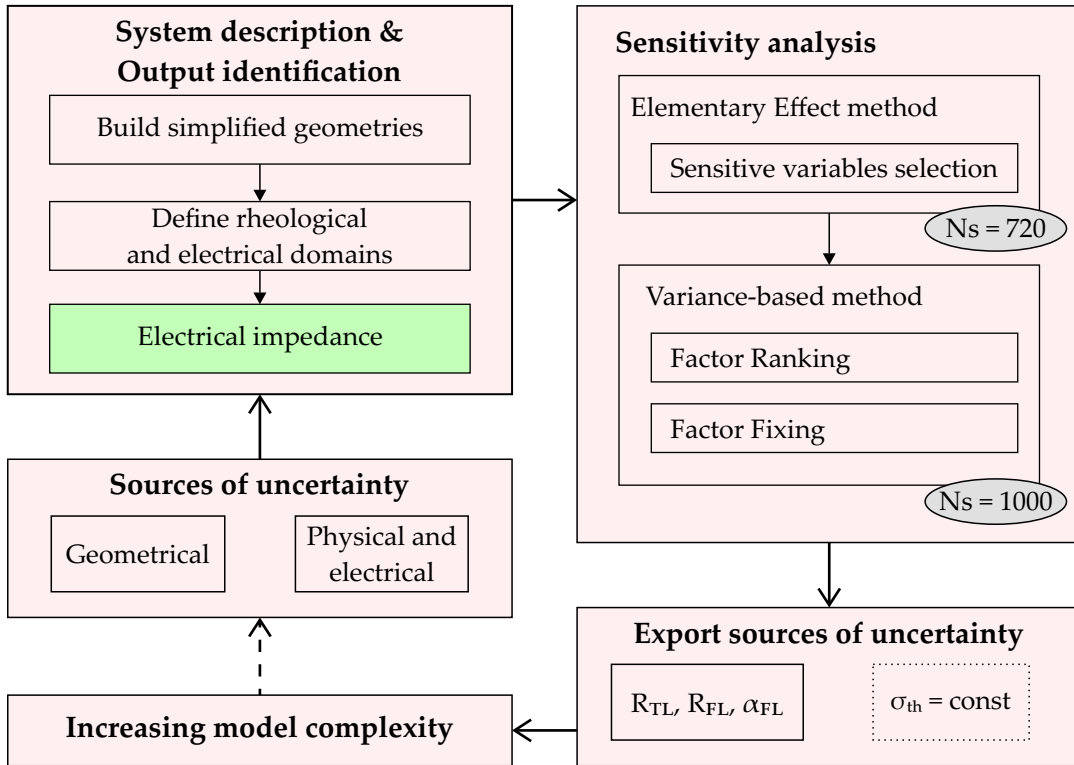
Figure 4.2.: Schematics of the preliminary assessment of the sensitive parameters. The geometrical, physical and electrical variability is imposed onto the thoracic model from where the impedance is computed. The sensitivity analysis includes an initial screening with Elementary Effect method and a successive variance-based method. In gray are the number of simulations performed for these tasks. The results are exported to the more complex model described in the next sections.

and those with the TBAD.

Sources of impedance changes during a cardiac cycle   The measured electrical impedance without respiratory or cardiac activity is known as static thoracic base impedance Z_0. Upon ventricular ejection, a time-dependent pulsatile impedance change $\Delta \underline{Z}(t)$ is obtained. When $\Delta \underline{Z}(t)$ is super-imposed on Z_0 the time variable total transthoracic impedance $\underline{Z}(t)$ is registered. By eliminating the oscillating cardiac-asynchronous respiratory component, $\underline{Z}(t)$ comprises a static DC component Z_0 (from $22\,\Omega$ to $45\,\Omega$) and a dynamic AC component $\Delta \underline{Z}(t)$ (from $0.1\,\Omega$ to $0.2\,\Omega$), synchronous to cardiac activity [15, 168]. In many studies, sources of the thoracic impedance changes have been investigated, and a consensus is lacking in the origins of cardio-synchronous impedance changes due to different model assumptions. Hereof different approaches are listed in De Sitter et al. [44]. Of course, simulation of transthoracic bioimpedance signals considering all possible time-dependent sources is impossible. Also, comparing experimental results obtained from dissected patients with earlier measurements in healthy states is practically
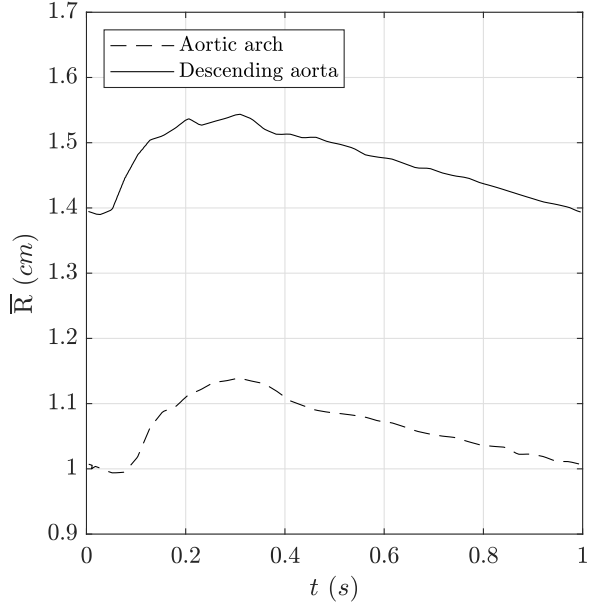
Figure 4.3.: Spatial average time-dependent cross-sectional radius of the aortic arch and the descending aorta during one cardiac cycle of 1 s. Figure readapted from Badeli et al. [10].

infeasible. Nevertheless, the focus of this work is to compute the discrepancy between the healthy and the dissected state and not the evaluation of absolute measurement values. Therefore, only the velocity-induced blood conductivity variation and the aorta's volumetric changes are considered as sources of $\Delta \underline{Z}(t)$ in a healthy case. The magnitude of Z_0 not only varies among individuals and the frequency of the applied current, but also depends on the electrode configuration used for signal acquisition.

Volumetric changes of the blood-filled aorta   The volumetric expansion of the blood-filled aorta changes corresponding to the cardiac pulse wave. For the sake of simplicity, a spatial average time-dependent cross-sectional radius of the aorta has been used in the simulation model for two sections separately, the aortic arch and the descending aorta, see Fig. 4.3. The spatial average radius $\overline{R}$ is collected from real aortic measurements for different aortic sections, namely the aortic arch and the descending aorta. The data are based on measurements provided in Alastruey et al. [2] from a young, healthy male volunteer at rest.

Velocity induced blood conductivity variation   The electrical properties of resting blood mainly depend on the volume fraction of RBCs, namely hematocrit H, the temperature, and the cell shape. However, the electrical properties of flowing blood are found to be influenced by the flow rate [105, 171]. A spatial average time-dependent velocity of the blood flowing inside the aorta, i.e., reduced average velocity $\overline{u_z/\mathrm{R}}$, is collected from Alastruey et al. [2], and taken into account for the aortic arch and the descending aorta, see Fig. 4.4. This velocity is composed by
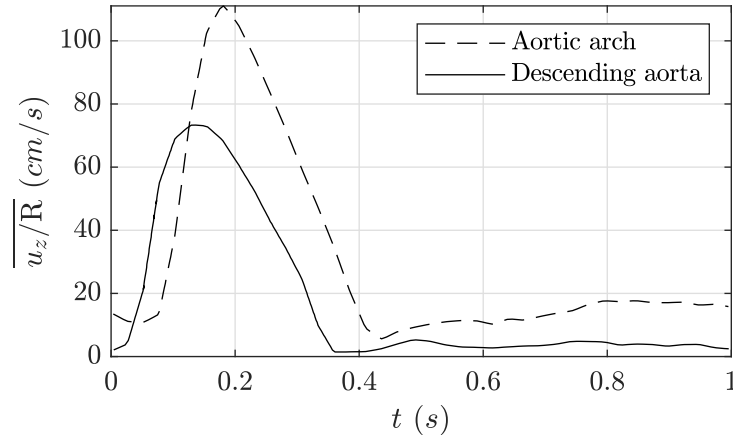
Figure 4.4.: Blood reduced average velocity in the aortic arch and the descending aorta during one cardiac cycle of 1 s. Figure readapted from Badeli et al. [10].

$\overline{u_z}$ as the spatial average blood velocity, and $\overline{R}$ as the spatial average cross-sectional radius of the aorta. During the systolic phase of a cardiac cycle, the heart contracts to pump blood into the aorta, and in the diastolic phase, the heart relaxes after contraction. As also confirmed in the previous chapter, the pulsatile blood flow causes the variation of blood conductivity inside the aorta. The reason is the orientation and deformation of the RBCs in case of flowing blood. At higher velocities, the shear stress increases, deforms the RBCs in the layer with the highest stress close to the vessel wall, and aligns them throughout the vessel. Both effects lead to a higher conductivity than the resting blood, see Fig. 4.5 for reference [56, 76].

Based on the formulation described in Hoetink et al. [76] where the blood is modeled as a Newtonian fluid in steady flow, the blood conductivity changes as a function of reduced average velocity $\overline{u_z/\mathrm{R}}$. Different hematocrit levels also alter $\Delta\sigma_{\mathrm{bl}}$ as shown in Fig. 4.5. From this figure, it is evident that more conductivity changes of blood exist with higher hematocrit levels. It is also evident that the conductivity changes mainly occur at lower blood velocities, and the slope of the $\Delta\sigma_{\mathrm{bl}}$ curve decreases significantly for higher velocities.

As already demonstrated in the previous chapter, and shown in Gaw et al. [63] and successively in Gaw et al. [64], the blood conductivity during pulsatile blood flow is not the same at any given velocity during acceleration and deceleration. This disparity is a consequence of the RBCs' inability to achieve complete randomization at end-systole, which leads to minor but still considerable conductivity changes during the cardiac cycle. For simplicity, a steady flow assumption is considered in this study. The conductivity changes shown in Fig. 4.6 have been assumed in the simulation model.

Sensitivity analysis This study aims to use a SA technique to identify which electrode configuration has significant changes in impedance cardiogram $-|\mathrm{d}\underline{Z}/\mathrm{d}t|$ given the uncertainty on TBAD's developed status. The difference in impedance cardiograms between healthy and dissected models provides the changes between the two states of the patient, so to simulate
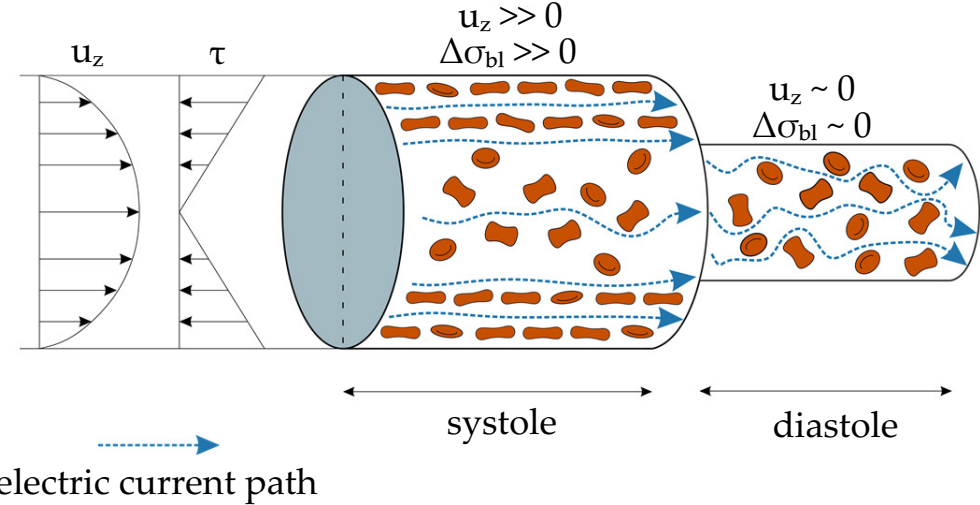
Figure 4.5.: Effect of orientation and deformation of RBCs on the electrical conductivity of blood in a vessel during the systole and diastole. Figure readapted from Badeli et al. [10].

TBAD identification.

In this application, only the first- and the total-order Sobol indices are considered. Any interaction between the input random variable can be derived by subtracting the second index from the first. Consequently, the difference will result in the amount of interaction present in the model.

The Sobol indices are computed from a PCE [158], representing a valid mathematical meta-model. Finally, it is possible to estimate the two sensitivity indices as the ratio between the PCE coefficients from the PCE. Since the case study is evaluated in time, the implementation of time-dependent indices is implemented following Alexanderian et al. [3]. The PCE is computed through the UQLab toolbox for Matlab [99]. However, the time-dependent indices are developed manually from the extrapolation of the PCE coefficients.

4.4. Simulation model

Geometry, physics and formulation   A 3-D numerical simulation model is used to investigate the changes in the electric potential and the impedance changes on the thorax surface. The model has been set up in COMSOL Multiphysics™ for the underlying time-harmonic current flow problem. Since the cardiac cycle duration is much higher than the period of the injecting current, simulations can be performed in the frequency domain. The electric potential drop is evaluated
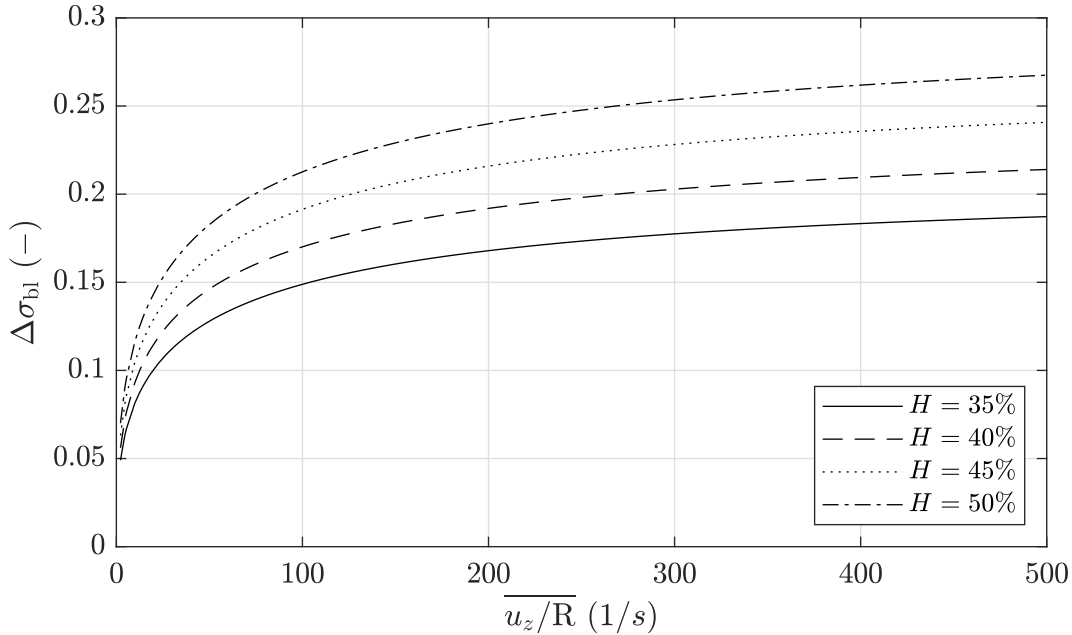
Figure 4.6.: Relative blood conductivity changes as a function of reduced average velocity $\overline{u_z/\mathrm{R}}$ for different hematocrit H levels. Figure readapted from Badeli et al. [10].

between the measuring electrodes by solving the Laplace equation for the electric potential V:

$$\nabla \cdot \left[(\sigma^{(e)} + j\omega^{(e)}\varepsilon^{(e)})\Delta V \right] = 0 \ . \tag{4.1}$$

where $(\nabla \cdot)$ denotes the divergence, and $\sigma^{(e)}$ is the electrical conductivity. Since the simulations are performed in the frequency domain, V is considered as a phasor with frequency $\omega^{(e)}$, and electrical permittivity $\varepsilon^{(e)}$. The term in the square brackets is also defined as *complex conductivity*. The subscript (e) is added to the terms in Eq. (4.1) to avoid confusion with previously introduced quantities.

The model consists of a simplified geometry, as shown in Fig. 4.7. Three pairs of source electrodes (injection) are placed on the surface of the thorax (each pair in one vertical line) and inject an alternating current with a magnitude of $5\,\mathrm{mA}$ and a frequency of $100\,\mathrm{kHz}$ asynchronously. For each injection, the electric potential drop is evaluated between five measurement electrode pairs (each pair in one vertical line) which leads to the thoracic impedance

$$\underline{Z} = \frac{\underline{V}_\mathrm{u} - \underline{V}_\mathrm{l}}{\underline{I}} \ , \tag{4.2}$$

where $\underline{V}_\mathrm{u}$ and $\underline{V}_\mathrm{l}$ are the potentials measured at the upper and lower sensors, respectively. The boundary conditions are defined as

- $\underline{V}_\mathrm{u}$ is constant
- $\int_S \left[(\sigma + j\omega\varepsilon)\Delta\underline{V}_\mathrm{u} \right] \cdot \boldsymbol{n}dS = I_0$

4. On configuration optimization of simulated thoracic bioimpedance
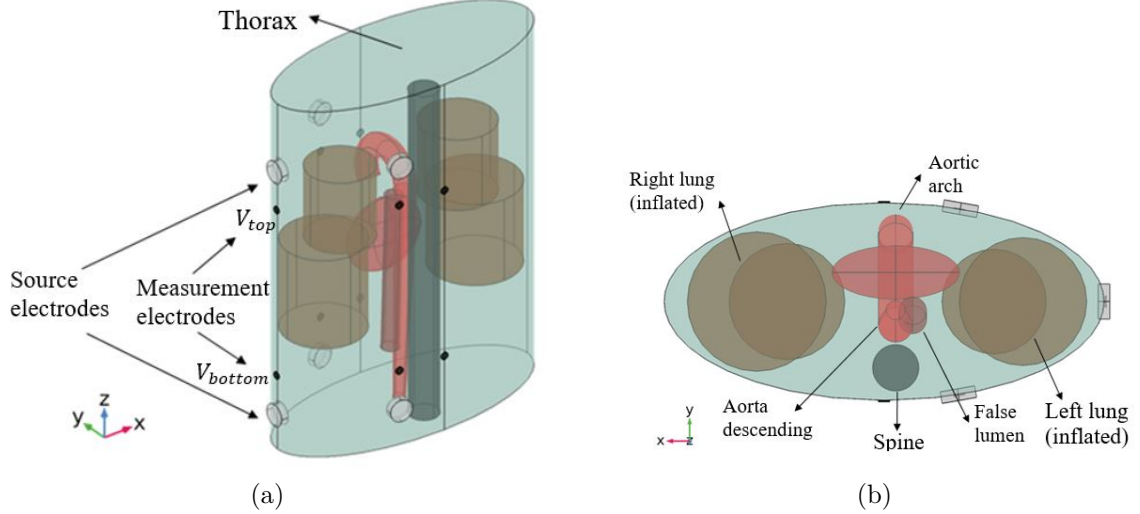
Figure 4.7.: Simulation model setup: a) 3D view and b) bottow view. Figure readapted from Badeli et al. [10].

- $\underline{V}_l = 0$
- $\boldsymbol{n} \cdot \left[(\sigma + j\omega\varepsilon)\Delta V \right] = 0$ on the thorax surface

where $\boldsymbol{n}$ is the normal unit vector. A tetra-polar spot electrode configuration is used as proposed by Mansouri et al. [97]. Different positions for source and measurement electrodes have been chosen to reach the most noticeable discrepancy between the impedance cardiograms of the healthy and dissected conditions [135]. The conductivity and the permittivity of tissue types considered in the simulation model have been taken from data provided in [58–60]. Other surrounding materials such as muscles, fat, and ribs are not considered directly in the simulation model. However, a mean conductivity and permittivity are assigned to the thorax domain to provide a realistic value for the static thoracic impedance Z_0 of about $25\,\Omega$, as reported in Bernstein [15]. Only the first half of the cardiac cycle is considered in the simulation model in order to reduce the computational cost.

Modelling physiological changes in the presence of the false lumen It has been shown that the blood flow is highly disturbed inside the aorta and changes locally to turbulent flow with strong recirculation [37, 148]. Flow disturbances occur around the dissection, which inhibits the deformation and orientation of the RBCs. Thus, the flow shear rate and, consequently, the electrical properties of blood are altered. At the highest blood flow velocity, i.e., at the highest RBCs' deformation and orientation rate, a remarkable difference in the electrical conductivity between the healthy (non-disturbed flow) and the aortic dissection conditions can be expected [11]. Since no experimental or simulation data exist regarding conductivity changes of blood in this kind of disturbed flow, it is assumed that the blood flow disturbances increase with a radially growing FL, thus descresing the conductivity changes. Due to the imposed variation
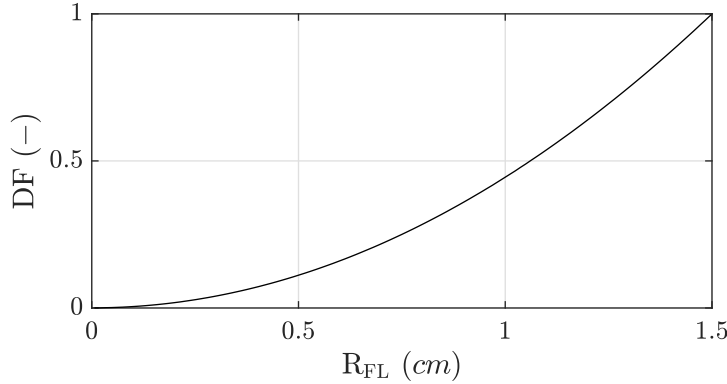
Figure 4.8.: Damage factor DF as a function of the radius of the FL R_{FL}. Figure readapted from Badeli et al. [10].

given by the application of SA, several TBAD conditions can be simulated, hence, several FL radii are produced. To quantify this assumption, a damage factor DF has been introduced for each simulation. DF is the ratio of the dissection volume to the maximum volume of the FL

$$\text{DF} = \frac{\pi R_{FL}^2 L_{FL}}{\pi \max\left(R_{FL}^2\right) L_{FL}} = \frac{R_{FL}^2}{\max(R_{FL}^2)} \ , \tag{4.3}$$

where R_{FL} and L_{FL} are the radius and the height of the FL, respectively. The maximum value for the radius of the FL in the simulation model is $1.5\,\text{cm}$. When $R_{FL} = 1.5\,\text{cm}$, it is assumed that the flow disturbances in the descending aorta are at maximum, see Fig. 4.8. DF is applied to the conductivity changes of blood in the descending aorta during the cardiac cycle to model the decrease in the conductivity changes of blood due to dissection, as described in the next section.

4.5. Application

Since the study aims to catch the difference between different health conditions, two numerical models are set. The metamodels simulate the healthy and diseased condition of a virtual patient. Given the nature of these surrogates, different health and disease conditions can be described. The first one refers to the healthy condition, and the second one to the dissected condition. As described earlier, the latter differs from the first one in the presence of the FL and different blood flow profile. Therefore, different input spaces variations are produced for each model. Besides, introducing variability in the input space of the models will guarantee the realization of as many virtual patient-specific cases as the dimension of the input sample. Thus, a deeper understanding of the impedance cardiography for a human thorax can be revealed. From the models' evaluations, the PCEs for the healthy and dissected conditions are constructed, and analyzing the differences between them will guide the choice of the best electrode configuration. A visualization of the procedure to achieve the aim of the current study is visualized in Fig. 4.9.

4. On configuration optimization of simulated thoracic bioimpedance
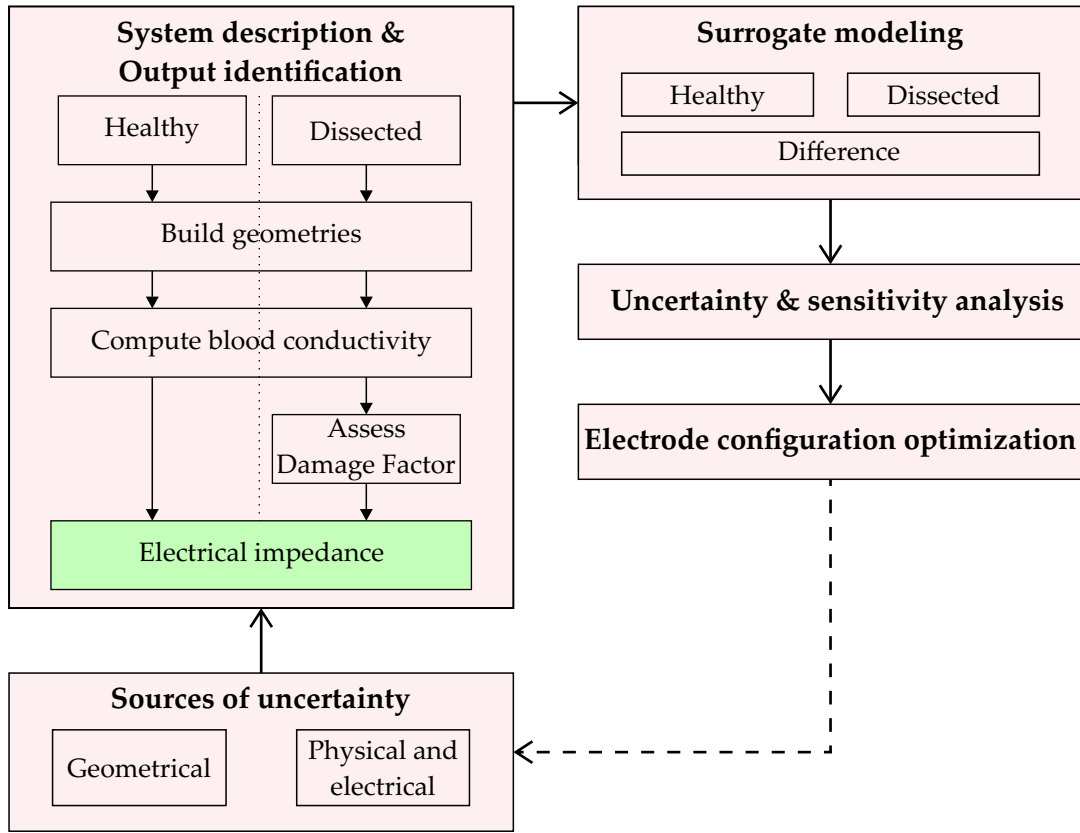
Figure 4.9.: Electrode configuration optimization scheme. After defining the source of uncertainty, both healthy and dissected models are built, the electrical conductivity of the system's blood is computed, and the damage factor DF is computed for the dissected model. Next, surrogate modeling of both cases and their difference is evaluated, leading to uncertainty and sensitivity analysis. Finally, the best candidates electrode configurations are determined.

The input space of the healthy case is composed of only two random variables, namely the maximum radius of the TL R_{TL} and the blood conductivity coefficient ζ_H. R_{TL} is considered uniformly distributed between $1.35\,\mathrm{cm}$ and $1.95\,\mathrm{cm}$, according to the study of Wolak et al. [176]. As shown in Fig. 4.3, the average radius of the aorta changes in time due to pressure changes over a cardiac cycle. Since the aorta in the simulation model is considered a blood-filled lumen, different values of the R_{TL} emulate different blood volumes dilating the aorta, in other words, different stroke volumes (SV). It has to be mentioned that changes in the SV will also vary the peak blood velocity in the aorta. Since almost all the RBCs are entirely aligned and deformed for higher velocities, the differences among the blood conductivity changes for different SVs are not significant. Based on the distribution's moments of R_{TL}, the SV changes approximately between $62\,\mathrm{mL}$ and $140\,\mathrm{mL}$ in the simulation model.

The coefficient ζ_H expresses the blood conductivity change variation due to hematocrit level,

Table 4.2.: Input space description for the healthy and dissected study cases. Table readapted from Badeli et al. [10].

	$p(x_i)$	Unit
R_{TL}	$\mathcal{U}[1.35,\ 1.95]$	cm
ζ_H	$\mathcal{U}[1.00,\ 1.10]$	-
R_{FL}	$\mathcal{U}[0.30,\ 1.50]$	cm
α_{FL}	$\mathcal{U}[2.90,\ 3.65]$	rad

as shown in Fig. 4.6; thus, it emulates a scaling factor for $\Delta\sigma_{bl}$ as

$$\Delta\sigma_{bl}(u_z, H) = \zeta_H \Delta\sigma_{bl}\left(u_z, H^\dagger\right) \tag{4.4}$$

where $H^\dagger$ refers to hematocrit level 35 %, as this is the minimum level considered for the model. The parameter ζ_H is set as

$$\zeta_H = \begin{cases} 1 & H = H^\dagger \\ 1 + h' & H > H^\dagger \end{cases} . \tag{4.5}$$

The coefficient h' is formulated as the variation of conductivity changes with respect to the reference $\Delta\sigma_{bl}\left(H^\dagger\right)$ at the basic hematocrit level. Its formulation is expressed as

$$h' = \frac{\Delta\sigma_{bl}\left(H\right) - \Delta\sigma_{bl}\left(H^\dagger\right)}{\Delta\sigma_{bl}\left(H^\dagger\right)} . \tag{4.6}$$

This equation computes the difference in conductivity changes between two hematocrit levels. In conclusion, since the variable H is uniformly distributed between 35 % and 55 %, ζ_H is also uniformly distributed between 1 and 1.1. Therefore, the blood conductivity changes for the healthy case is computed as:

$$\Delta\sigma_{bl}\left(u_z, H\right) = \zeta_H \Delta\sigma_{bl}\left(u_z, H^\dagger\right) . \tag{4.7}$$

The dissected condition includes both the random variables of the healthy condition, the radius of the FL R_{FL} and the radial position of the FL to the TL α_{FL}, representing different possible positions of the FL. The two new parameters have been considered uniformly distributed since knowledge regarding the dimension and position of the FL is not available before the measurement, and the uniform distribution better represents the lack of knowledge regarding a model variable. The description of the input space for both case studies are given in Tab. 4.2. Furthermore, since the damage factor DF affects the conductivity changes in the case of aortic dissection, the blood conductivity change results in

$$\Delta\sigma_{bl}\left(u_z, H\right) = \zeta_H \Delta\sigma_{bl}\left(u_z, H^\dagger\right)\left(1 - DF\right) . \tag{4.8}$$

The two models produce a measurement of the impedance cardiograms for each source electrode pairs N_{inj} and each measuring electrode pairs N_{meas} at each time step N_t. The time interval is limited to the first half of the cardiac cycle. After setting the input and output space characteristics, the next step is to set up the options for the PCE. It is essential to notice that a minimum number of point evaluations N_s is needed to have an accurate surrogate. N_s is defined to satisfy

$$N_s \geqslant 2\frac{(M+d)!}{M!d!} \; , \tag{4.9}$$

where M is the input space dimension, and d is the order of the polynomial. The healthy condition model has N_s equal to 100, while for the dissected condition, N_s is assumed 150. To ensure proper construction of the metamodel and an accurate representation of the interaction between the random input variables, polynomial order of 4 has been chosen for both models. Such a degree guarantees the presence of enough interaction terms in the expansion and minimize the approximation error.

Two PCE functions $\widetilde{HC}(t)$ and $\widetilde{DC}(t)$ are introduced. The two surrogates express the impedance cardiograms of the healthy HC and the dissected condition DC models as

$$\widetilde{HC}_{n,m}(t) = -\left|\frac{\mathrm{d}\underline{Z}}{\mathrm{d}t}\right|_{HC} \tag{4.10a}$$

$$\widetilde{DC}_{n,m}(t) = -\left|\frac{\mathrm{d}\underline{Z}}{\mathrm{d}t}\right|_{DC} \; , \tag{4.10b}$$

where n and m are the indices related to the source and the measurement electrode pairs, respectively. The difference $\tilde{Y}_{n,m}(t)$ between the last two equations is then calculated as

$$\tilde{Y}_{n,m}(t) = \widetilde{HC}_{n,m}(t) - \widetilde{DC}_{n,m}(t) \; . \tag{4.11}$$

Three source electrode pairs (A, B, and C) and five measurement electrode pairs (m_1 to m_5) are considered in the simulation models of the healthy and dissected conditions, see Fig. 4.10. Each simulation contains an injection from one of the source electrode pairs and measuring from all the five measurement electrode pairs. For each simulation, the impedance cardiogram $-|\mathrm{d}\underline{Z}/\mathrm{d}t|$ is computed, and through all the simulation results, i.e., for different input variables, the two surrogates are evaluated. The aim is to find the setup which gives the maximum difference between the impedance cardiograms measured for the healthy and dissected conditions, which is denoted as $\tilde{Y}_{max}$.

4.6. Results and discussion

Combinations of injections have been applied, and the results of $\tilde{Y}_{n,m}(t)$ are shown in Fig. 4.11. The figure displays the difference between the measurements of the healthy and dissected cases. This difference is color-coded so to spot significant discrepancies between the cases. The time, i.e.,
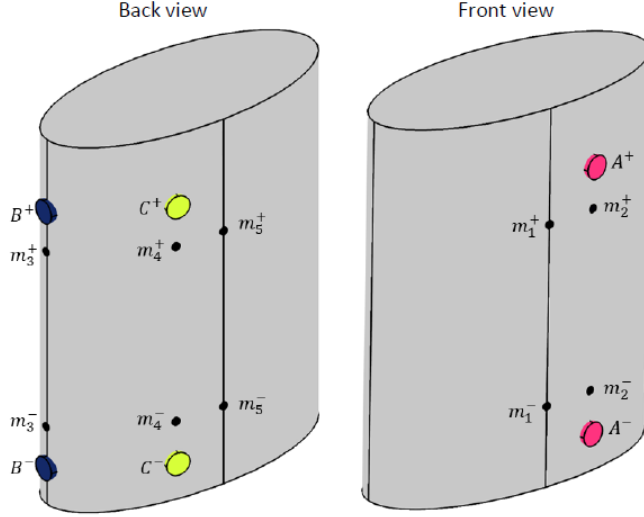
Figure 4.10.: Source electrode pairs and measurement electrode positions. Figure readapted from Badeli et al. [10].

from $t = 0\,\mathrm{s}$ to $t = 0.5\,\mathrm{s}$, is represented on the y-axis and discretized in 20 time instances. The x-axis displays the measurement sensor position. For each electrode configuration, the highest difference occurs in the third time step where, indeed, the blood velocity is at the peak level, or in other words, the blood conductivity is the highest. In the classical ICG application the maximum value of the impedance cardiogram is used for calculating stroke volume and cardiac output [16].

Successively, the best electrode configuration will be identified as having the highest $\widetilde{Y}_{n,m}(t)$ value at the third time instance. There are in total 15 possible configurations when using three injection points and five measurement sensors. To identify the ones that are worth analyzing, a plot that shows the variance of the outputs $\widetilde{Y}_{n,m}$ at peak systole is employed and displayed in Fig. 4.12. As noticeable, the highest variance is detected in configurations A2 and C4. Note that the configuration notation identifies the injection electrode in the first and the measurement sensor in the second. Other configurations, such as A1 and C5, also show relatively high output variability. However, their analysis is omitted here. Configurations A2 and C4 are then considered as game changers configurations during the simulation. Their high variation can result from volumetric changes, which is, in this case, TBAD disease. It is now of interest to understand what is causing this variability. The highest discrepancies are showing high variability in all the configurations. Therefore, an analysis of the input sensitivity is required to analyze the system mechanics better. For this purpose, the use of SA is employed. For the sake of comparison, configuration B3 is chosen since it is often the favorite configuration in clinics.

The A2, B3, and C4 configurations are selected, and the corresponding ICG signal is illustrated
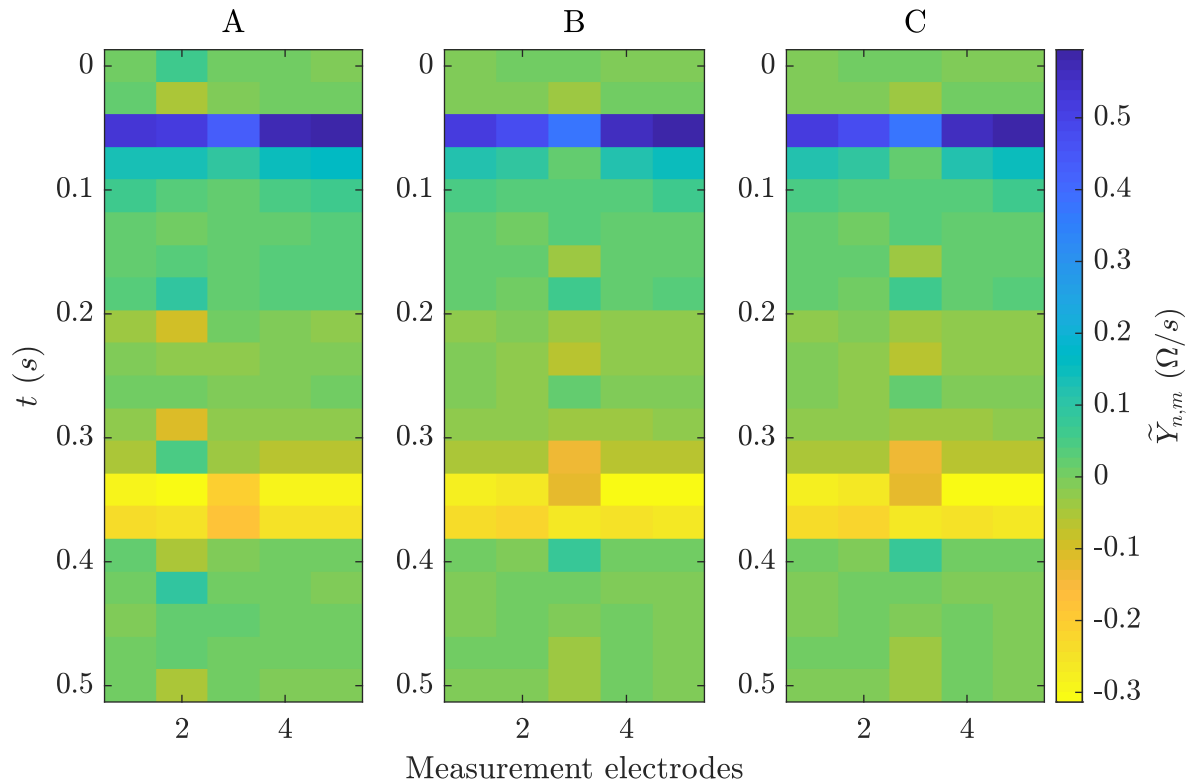
Figure 4.11.: Value of $\widetilde{Y}_{n,m}(t)$ reflecting the discrepancy between the healthy and dissected conditions for 20 time steps and all proposed electrode combinations. Figure readapted from Badeli et al. [10].
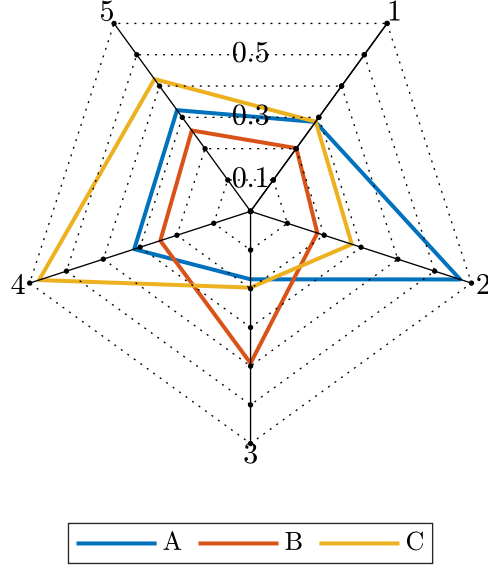
Figure 4.12.: Variance of ICG dignal difference for the three injection and five measurement sensors. The represented variance is computed at the peak systole of the cardiac cycle, that is the time with maximum difference between healthy and dissected condition case. Figure readapted from Badeli et al. [10].

in Fig. 4.13, together with the total-order sensitivity indices. It can be observed that the computed impedance reaches values higher than $0.5\,\Omega\,\mathrm{s}^{-1}$ at the peak systole for A2, as expected. The sensitivity indices show the dominance of $\mathrm{R_{FL}}$ on this output. Other parameters ($\mathrm{R_{TL}}$, ζ_{H}, and α_{FL}) appear to be uninfluential on the model output. Given this conclusion, the A2 configuration appears to be a strong candidate for a valuable electrode configuration to identify TBAD.

A different conclusion stands for the B3 configuration, where the signal appears to depend on both radii equally. In addition, the ICG discrepancy between healthy and dissected cases is not as high as desired. A different scenario is present for configuration C4. As visible, this configuration produces the highest discrepancies between the healthy and dissected cases. The higher value of $-|\mathrm{d}\underline{Z}/\mathrm{d}t|$ is registered in this configuration at the peak systole. In addition, the $\mathrm{R_{FL}}$ is the most sensitive parameter during the whole heart cycle, suggesting that the secondary volume, i.e., the FL, is the critical element in the ICG measurement from this configuration. The sensitivity analysis of the difference between the healthy and the dissected cases shows that $\mathrm{R_{FL}}$ has the highest sensitivity, thus enforces the highest impact on the output $\widetilde{Y}_{C,4}(t)$ followed by $\mathrm{R_{TL}}$, while ζ_{H} and α_{FL} are not sensitive.

Both configurations, A2 and C4, are valuable candidates to be the best configuration in TBAD detection. However, it is crucial to notice the role of $\mathrm{R_{FL}}$ in those scenarios. While the radius

4. On configuration optimization of simulated thoracic bioimpedance
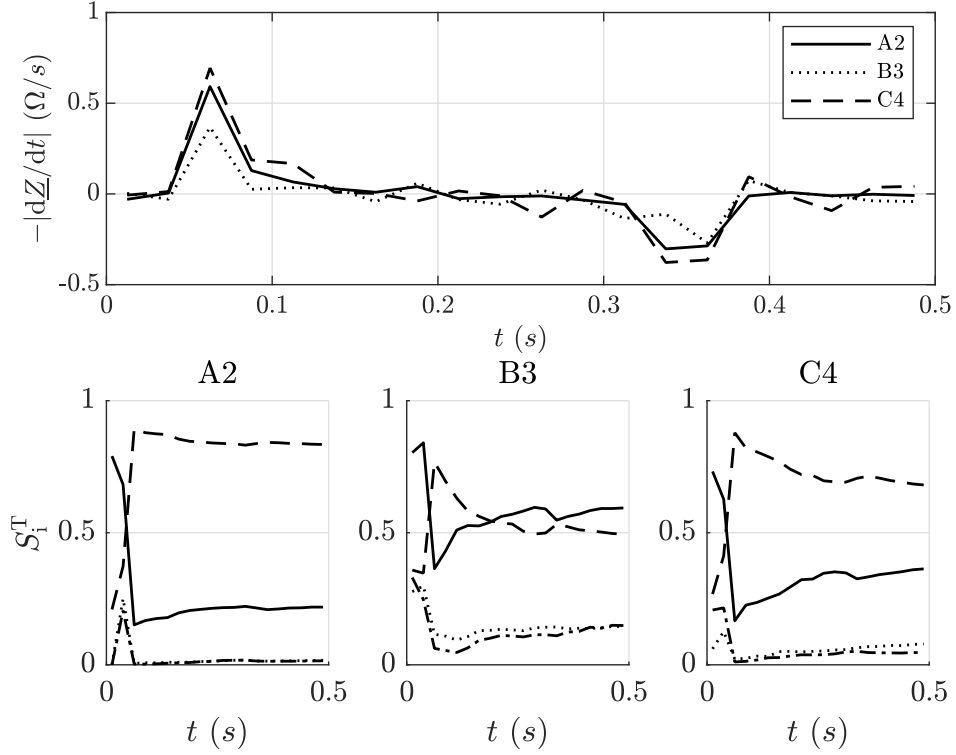
Figure 4.13.: (top) Difference ICG signal $\widetilde{Y}$ for the electrode configurations A2, B3, and C4. (bottom) Sensitivity analysis results of $\widetilde{Y}$. The total order sensitivity indices are related to R_{TL} (continuous line), ζ_H (dotted line), R_{FL} (dashed line), and α_{FL} (dash-dotted line). Figure readapted from Badeli et al. [10].

of the FL is constantly dominant in the ICG process for the first configuration, its influence is slightly decreasing in time for the C4 arrangement. Therefore, further analysis may help to identify the solution optimization.

In Fig. 4.13, the total sensitivity index S_i^{T} is displayed. The first sensitivity index is omitted. For completeness, the difference between total- and first-order sensitivity indices is reported in Fig. 4.14. The C4 configuration is subject to a shallow interaction rate, which can be seen in the low value of the indices difference. However, the A2 configuration again shows a more stable behavior of the sensitivity indices. Naturally, the R_{FL} is the dominant factor in the model, showing the highest interaction term. However, the interaction rate of the model can be considered neglected due to its low value in A2 and C4. This low interaction is a significant feature since factors' interactions could affect the final result in a non-predictable way. Thus, as expected, the discrepancy between the impedance cardiograms of the healthy and dissected cases primarily originates from the random variable R_{FL} and, consequently, the damage factor DF.

In Fig. 4.15, $\widetilde{Y}_{max}$, i.e., the ICG difference at peak systole, is shown as a function of the damage factor DF for each electrode configuration. $\widetilde{Y}_{max}$ increases almost linearly with the damage factor, which means that the probability of identifying an aortic dissection grows as the disease
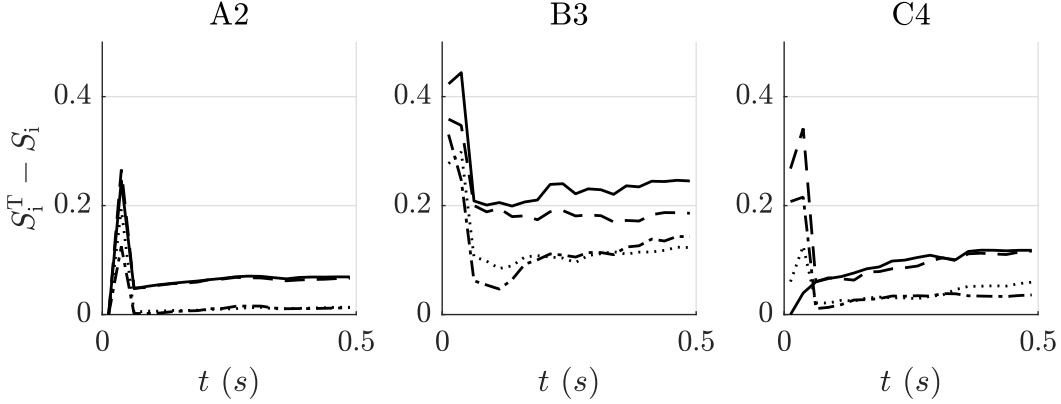
Figure 4.14.: Interaction level imposed by each input random variable on the ICG signal difference. The interaction is computed by the difference between the total and first order Sobol indices. The sensitivity indices are related to R_{TL} (continuous line), ζ_H (dotted line), R_{FL} (dashed line), and α_{FL} (dash-dotted line).

progresses. As a confirmation of the previous results, the DF can represent the progression of the aortic dissection, and the ICG difference between the healthy and diseased cases increases together with the damage factor. The injection from both A and C sensors appears to be the strongest in all the measuring sensors. The quadratic behavior visible for the B3 configuration, and the high interaction between the input factors, drive towards the conclusion that the side injection is not a valuable candidate for high TBAD detectability.

The same visualization purpose is displayed in Fig. 4.16. Here, $\widetilde{Y}_{max}$ is plotted for different values of the damage factor DF for the three selected configurations. Again, the B3 configuration fails in representing a clear cut between a healthy and a diseased measurement. The other two, i.e., A2 and C4, are characterized by a clear distinction of values in the systolic and early diastolic phases. Therefore, their importance in TBAD detection from ICG measurement is confirmed. In addition, these changes are also observable in the evaluation of SV and CO.

To summarise, in the first stages of the TBAD, in which the existence of the FL does not make apparent changes to the rheology of the blood flow, the presence of the disease by impedance cardiography might not be noticeable. However, as soon as the dissection creates remarkable pathological changes in the cardiovascular system, the changes in the measured impedance cardiogram due to the development of the disease, such as FL expansion and FL thrombosis, might be trackable. The best configuration for the diagnosis purpose is assumed to be the one with the highest $\widetilde{Y}_{max}$ value, which the configurations A2 and C4 reach. Furthermore, a FL expansion changes the blood flow significantly in both lumina. Thus, $\widetilde{Y}_{max}$ is accounted for tracking the status of the disease.
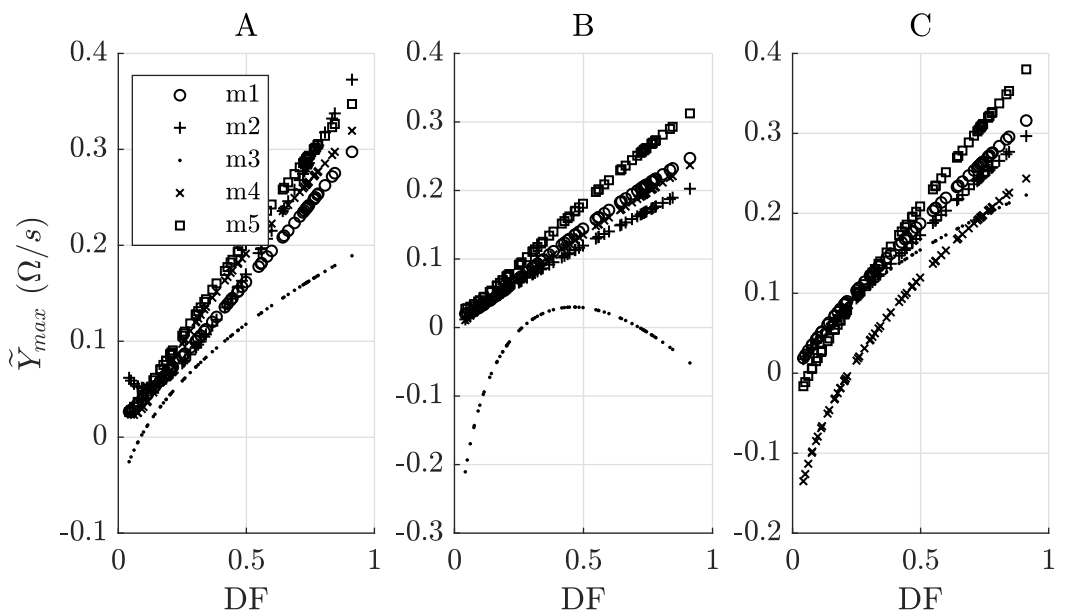
Figure 4.15.: Change of $\widetilde{Y}_{max}$ by the damage factor DF for each injection source (A, B, and C) and each measurement sensor pairs (m1 to m5). Figure readapted from Badeli et al. [10].
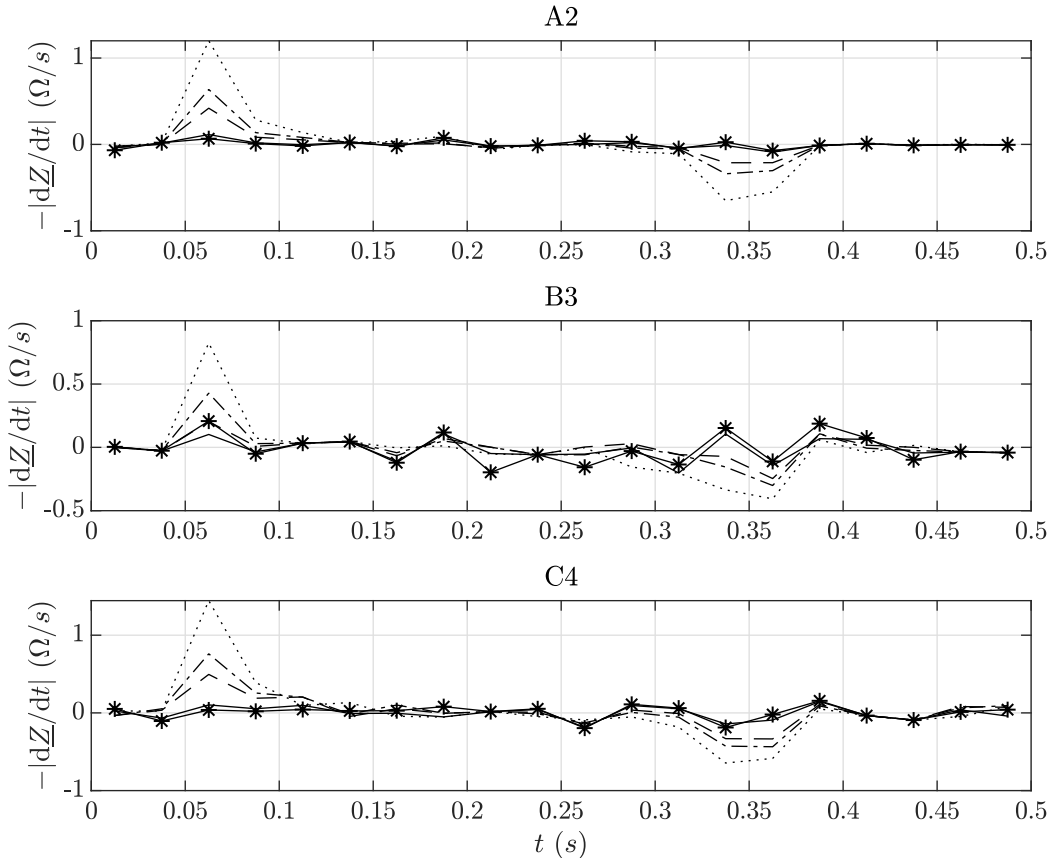
Figure 4.16.: Visualization of $\widetilde{Y}_{n,m}(t)$ variation by increasing the damage factor DF in the three config- urations A2, B3, and C4. The healthy case, DF = 0, is represented as a continuous line with asterisk markers (*). Diseased conditions are denoted by DF = 0.07 (continuous line), DF = 0.28 (dashed line), DF = 0.07 (dot-dashed line), and DF = 0.07 (dotted line). Figure readapted from Badeli et al. [10].

5. On thrombus formation

The focus is here on a phenomenological thrombus formation model and its variation when uncertainties are plugged in. Tuning model parameters have developed this particular model to fit a quantitative patient-specific result, i.e., the amount of thrombus produced. However, and again, physiological uncertainties were never taken into account. Jafarinia et al. [84] have performed an exciting outcome on the effect of blood hematocrit. Here, they claim that increasing the level of red blood cells will eventually lead to less thrombus formation. Much is unfortunately still to discover.

In the following work, the investigation is focused more on the model parameters. Therefore, the published work of Melito et al. [103] is here illustrated. The following sections are hence based on this publication.

5.1. Introduction

The hemodynamic conditions in the FL, including flow disturbance, recirculations, and significant variability in the wall shear stress (WSS), presumably promote the formation and growth of thrombi [106]. In Tsai et al. [167], it is shown that partial thrombosis is associated with a higher mortality rate, whereas complete thrombosis of the FL improves patients' prognosis [14, 137]. Up to now, it is not entirely clear what circumstances favor thrombosis following aortic dissection. Thrombus formation models may play a vital role in the analysis of hemodynamics in cardiovascular environments.

Thrombosis formation represents an uncertain field of research. It is a complex phenomenon that involves hemodynamics, physics, and biochemical reactions, to cite a few. It has been challenging to determine the actual process of thrombus formation, especially in TBAD. Recent studies [7] showed that the formation of the FL enhances thrombus growth in low shear rate areas. This process is due to the recirculation areas in proximity to the lumina tears.

Furthermore, the new hemodynamic situation intensifies herein the platelets activation and aggregation [71]. The formation of thrombus is therefore coupled to hemodynamics and particles' mechanics. Indeed, the blood is usually considered as a suspension with non-Newtonian rheological behavior. The principal element in the blood is the RBC, which is usually modeled as the solid in the solution. The volume percentage of RBCs is indicated as hematocrit, which is extremely sensitive to thrombus formation [84].

In Menichini and Xu [106] and Menichini et al. [107], a hemodynamic-based model capable of predicting false lumen thrombosis in TBAD is developed. However, because the model is primarily phenomenological, the model's parameters may not be determined from the chemical

or biological characteristics of the blood. Instead, the parameters will usually be obtained from inverse modeling, i.e., fitting to measured data. However, suitable time-resolved data of thrombus-formation is very sparse, so it is vital to narrow down the number of model parameters. A global sensitivity analysis is suggested to understand the influence of the parameters [158]. In particular, a variance-based SA is employed, and the computation of the sensitivity indices is performed through a PCE, which functions as a surrogate model.

The model performs well in predicting the location of thrombus formation; however, it cannot reproduce the growth rate as observed in in-vivo and in-vitro studies. More insight into the model parameters and their role in thrombus growth is needed to bridge the gap between numerical simulations and real-life studies. This work identifies the most critical parameters for the thrombus growth model, and further analysis of the thrombus characteristic growth time indicates the parameters that could accelerate or inhibit the process of thrombus formation.

5.2. Methods

This section will describe the models and methods used to solve the problem at hand. Initially, the thrombus formation model is concisely described, concerning the initial and boundary conditions and the coupling with the fluid model described in the previous chapters. Finally, a brief review of the SA techniques used in this application is provided. A schematics of the study and of the thrombus formation model is provided in Fig. 5.1.

5.2.1. Thrombus growth model

The description of the model is collected and readapted from Jafarinia et al. [83]. The constitutive model of Menichini et al. [107] is adapted to model thrombus formation in the FL. The model controls the formation of thrombus based on wall shear stress (WSS), shear rate, residence time, and the concentrations of coagulant, and resting, activated, and bounded platelets. The model achieves reasonable simulation times for thrombus formation since it employs cycle-averaged field variables.

The amount of thrombus formation is influenced by the threshold values of the cycle-averaged WSS $\langle \tau_{\mathrm{w}} \rangle_{\mathrm{t}}$, shear rate $\langle \dot{\gamma} \rangle_{\mathrm{t}}$, residence time $\langle \mathrm{T_R} \rangle_{\mathrm{t}}$, as well as concentrations of bounded platelets c_{BPt} and coagulant c_{ct}. Note that the subscript t denotes a threshold value and that a high concentration of bounded platelets is indication of thrombus existence. Regions with a high concentration of bounded platelets are associated with thrombus formation, which inhibits blood flow. This effect is captured by the modification of the momentum balance in Eq. 3.10. The conversion of platelets from activated to bounded is given by

$$\frac{\partial c_{\mathrm{BP}}}{\partial t} = k_{\mathrm{BP}} \; \frac{c_{\mathrm{c}}^2}{c_{\mathrm{c}}^2 + c_{\mathrm{ct}}^2} \; \frac{\langle \mathrm{T_R} \rangle^2}{\langle \mathrm{T_R} \rangle^2 + \langle \mathrm{T_R} \rangle_{\mathrm{t}}^2} \; \frac{\langle \dot{\gamma}_{\mathrm{t}} \rangle^2}{\langle \dot{\gamma} \rangle^2 + \langle \dot{\gamma}_{\mathrm{t}} \rangle^2} \; c_{\mathrm{AP}}, \tag{5.1}$$

where k_{BP} represents the reaction rate constant and c_{AP} describes the contraction of activated platelets. Activated platelets are generated by activating resting platelets through the following
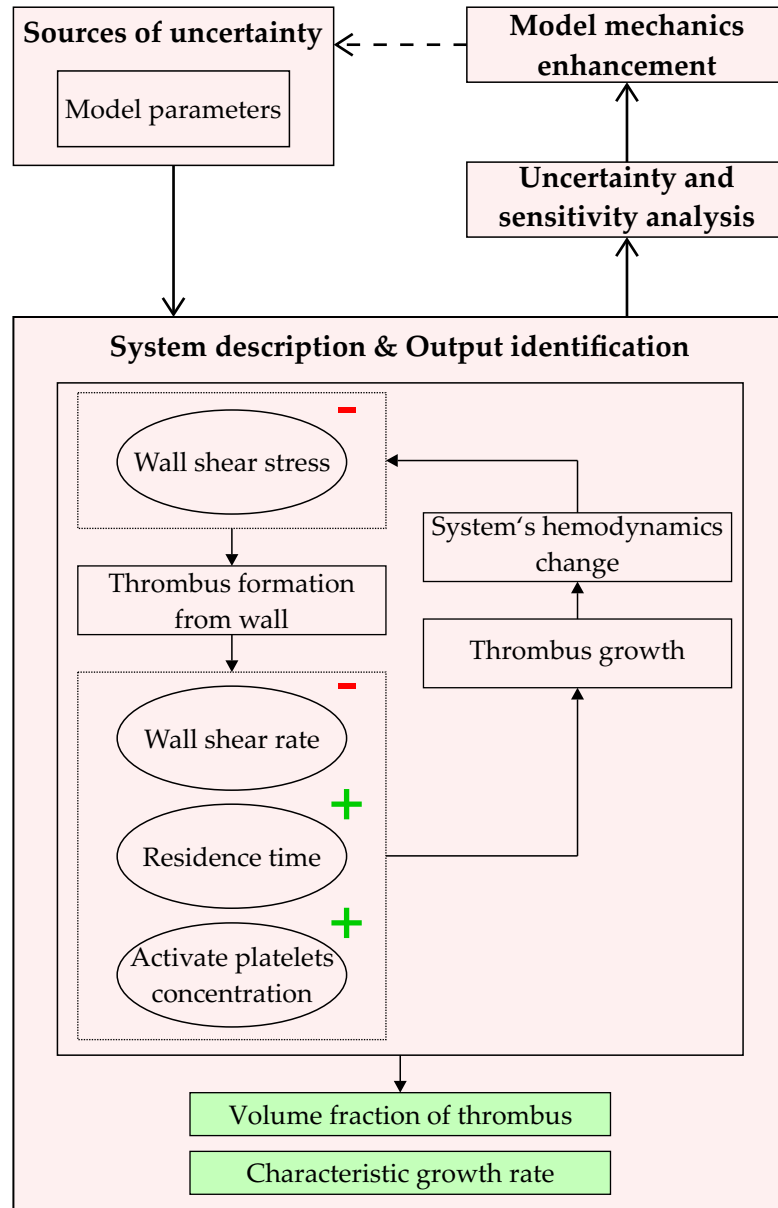
Figure 5.1.: The diagram of the thrombus formation study is here described. The model mechanics are illustrated. The rounded boxes represent model field variables, and the plus (+) and minus (-) signs express the increase and decrease of such variables. The volume fraction of thrombus and the characteristic growth rate are the quantities of interest used to decode the model mechanics.

5. On thrombus formation

transport equations

$$\frac{\partial c_{\text{RP}}}{\partial t} + \boldsymbol{u}\nabla c_{\text{RP}} = D_{\text{p}\dot{\gamma}}\nabla^2 c_{\text{RP}} - k_1 c_{\text{RP}} c_{\text{AP}} - k_2 c_{\text{RP}}\langle \text{T}_{\text{R}}\rangle \tag{5.2a}$$

$$\frac{\partial c_{\text{AP}}}{\partial t} + \boldsymbol{u}\nabla c_{\text{AP}} = D_{\text{p}\dot{\gamma}}\nabla^2 c_{\text{AP}} + k_1 c_{\text{RP}} c_{\text{AP}} + k_2 c_{\text{RP}}\langle \text{T}_{\text{R}}\rangle \ , \tag{5.2b}$$

where k_1 and k_2 being the reaction constants. The first accounts for the effect continuous activation of resting platelets, and the second considers the activation of platelets by thrombin exposure.

Red blood cells have a shear-dependent effect on platelets transportation. As already proposed [83, 107], the diffusion coefficient of platelets $D_{\text{p}\dot{\gamma}}$ is enhanced with an additional term, which includes the shear rate $\dot{\gamma}$ and the parameter β_{th}, as

$$D_{\text{p}\dot{\gamma}} = D_{\text{b}} + \beta_{\text{th}}\dot{\gamma}, \tag{5.3}$$

where D_{b} represents the Brownian diffusivity.

The coagulant concentration c_{c} represents the lumped effect of all underlying biochemical reactions in the coagulation cascade [107], which can be described by

$$\frac{\partial c_{\text{c}}}{\partial t} + \boldsymbol{u} \cdot \nabla c_{\text{c}} = D_{\text{c}\dot{\gamma}}\nabla^2 c_{\text{c}} + k_{\text{c}}\frac{c_{\text{BP}}^2}{c_{\text{BP}}^2 + c_{\text{BPt}}^2}\ \frac{\langle\dot{\gamma}\rangle_{\text{t}}^2}{\langle\dot{\gamma}\rangle^2 + \langle\dot{\gamma}\rangle_{\text{t}}^2}, \tag{5.4}$$

where k_{c} is a reaction constant for coagulant production. The effective diffusion coefficient $D_{\text{c}\dot{\gamma}}$ gets enhanced in areas of low cycle-averaged shear rates [107]

$$D_{\text{c}\dot{\gamma}} = D_{\text{c}}\frac{\langle\dot{\gamma}\rangle_{\text{t}}^2}{\langle\dot{\gamma}\rangle^2 + \langle\dot{\gamma}\rangle_{\text{t}}^2}, \tag{5.5}$$

where D_{c} is the coagulate diffusivity.

The reactive source term in Eq. (5.4) shows that the coagulant c_{c} is produced where c_{BP} is sufficiently higher than its threshold value c_{BPt} and where $\langle\dot{\gamma}\rangle$ is lower than its threshold value $\langle\dot{\gamma}\rangle_{\text{t}}$. However, the decisive production of coagulant concentration, initially assumed to be zero, occurs at the vessel wall via Neumann boundary conditions. The coagulant flux into the domain through the wall, denoted by the subscript w, is given by

$$D_{\text{c}\dot{\gamma}}\frac{\partial c_{\text{c}}}{\partial \boldsymbol{n}}\bigg|_{\text{w}} = k_{\text{cw}}\left(\langle\tau_{\text{w}}\rangle, c_{\text{BP}}\right) \ , \tag{5.6}$$

where k_{cw} is the coagulant reaction constant. If the cycle-averaged WSS exceeds the threshold value $\langle\tau_{\text{w}}\rangle \geqslant 0.2\,\text{Pa}$ and, simultaneously, the concentration of bounded platelets at the wall is greater than $c_{\text{BP}} \geqslant 2 \times 10^5\,\text{nmol/m}^3$, the reaction constant is equal to zero, i.e., $k_{\text{cw}} = 0$. The cycle-averaged residence time T_{R} is normalized by its maximum value in the corresponding cycle and defined as

$$\langle \text{T}_{\text{R}}\rangle = \frac{1}{\max(\text{T}_{\text{R}})} \cdot \frac{1}{T}\int_{nT}^{(n+1)T} \text{T}_{\text{R}}(x, y, z, t)\text{d}t \ . \tag{5.7}$$

Table 5.1.: Model parameters of the thrombus model. Table readapted from Melito et al. [103].

		Value	Unit
Bounded platelets concentration threshold	c_{BPt}	2×10^4	nmol/m^3
Coagulant concentration threshold	c_{ct}	1×10^4	nmol/m^3
Residence time threshold	$\langle \mathrm{T_R} \rangle_{\mathrm{t}}$	9×10^{-1}	-
Shear rate threshold	$\langle \dot{\gamma} \rangle_{\mathrm{t}}$	50	s^{-1}
Constant sink term	k_{th}	1×10^7	kg/m^3/s
Reaction rate bounded platelets	k_{BP}	8×10^{-10}	nmol/m^3/s
Reaction rate coagulant	k_{c}	2×10^6	nmol/m^3/s
Reaction rate constant platelets activation	k_1	1.2×10^{-14}	m^3/s
Reaction rate constant platelets activation	k_2	5×10^{-1}	s^{-1}
Brownian diffusion coefficient	D_{b}	1.6×10^{-13}	m^2/s
Diffusion coefficient of coagulant	D_{c}	1.6×10^{-8}	m^2/s
Coagulant reaction const. at wall	k_{cw}	2×10^4	nmol/m^2/s
Shear-enhancing coefficient	β_{th}	1.6×10^{-3}	m^2
Blood self-diffusion coefficient	$D_{\mathrm{T_R}}$	1.14×10^{-11}	m^2/s

Finally, the residence time $\mathrm{T_R}$ of the liquid components or the platelets in the field is determined by the following transport equation

$$\frac{\partial \mathrm{T_R}}{\partial t} + \boldsymbol{u} \cdot \nabla \mathrm{T_R} = D_{\mathrm{T_R}} \nabla^2 \mathrm{T_R} + 1 \ , \tag{5.8}$$

where $D_{\mathrm{T_R}}$ is the self-diffusivity of blood. The values of the constants applied in the thrombus formation model are listed in Table 5.1.

The thrombus growth is acting in the fluid model of Eq. (5.9). Here, the sinking term $-k_{\mathrm{th}}\phi_{\mathrm{th}}\boldsymbol{u}$ includes the k_{th} coefficient that stops the flow in presence of thrombus, and the degree of local thrombosis $0 \leqslant \phi_{\mathrm{th}} \leqslant 1$.

5.2.2. Coupling with rheological model

The fluid model is coupled with the thrombus model for several applications. In this case, the coupling process imposes some changes in the governing equations of the fluid. The central assumption of incompressible fluid and constant fluid density ρ is still valid. The Navier-Stokes equation in Eq. (3.10) includes the thrombus growth. Therefore, the blood flow model is described

5. On thrombus formation

by

$$\rho \left[\frac{\partial \boldsymbol{u}}{\partial t} + (\boldsymbol{u} \cdot \nabla)\boldsymbol{u} \right] = -\nabla p + \nabla \cdot \boldsymbol{\tau} - k_{\text{th}}\phi_{\text{th}}\boldsymbol{u} \ , \tag{5.9}$$

where ϕ_{th} is considered the degree of local thrombosis in the range $0 \leqslant \phi_{\text{th}} \leqslant 1$, as in

$$\phi_{\text{th}}(c_{\text{BP}}, c_{\text{BPt}}) = \frac{c_{\text{BP}}^2}{c_{\text{BP}}^2 + c_{\text{BPt}}^2} \ . \tag{5.10}$$

where c_{BP} is the concentration of bounded platelets. The thrombus is added by considering it a sink term, i.e., $-k_{\text{th}}\phi_{\text{th}}\boldsymbol{u}$, in the fictitious domain method. The value of k_{th} is sufficiently low to stop the flow where the thrombus is created.

5.2.3. Initial and boundary condition

For the inlet boundary condition of the velocity, a uniform velocity profile resulting in Reynolds number of 490 was imposed, with the no-slip condition for the walls. The only non-zero component of the inlet flow velocity $\boldsymbol{u}$ is u_x, while the second component u_y is set to zero given the 2D nature of the model geometry. The pressure gradient is equal to zero on all the boundaries except the outlet, which is considered to have a fixed value of zero. As discussed in Sect. 5.2.1, there are five equations to be solved for the thrombus formation model. For solving residence time T_{R} in equation Eq. (5.8), which is initially zero, the inlet value of T_{R} is fixed to zero, and the normal gradient on all the other boundaries is also set to zero. Initial values of resting platelets RP and activated platelets AP in the blood are taken from Menichini and Xu [106]. The inlet values of RP and AP in Eq.s (5.2a) and (5.2b) are fixed to their initial values. Zero normal gradients of AP and RP is imposed on all the other boundaries. For the coagulant equation in Eq. (5.4), the Neumann boundary condition discussed in Sect. 5.2.1 is implemented for the walls, while a zero fixed value at the inlet and a zero normal gradient at the outlet are applied. The bounded platelets equation is solved with zero initial concentration of bounded platelets.

5.2.4. Backward-facing step benchmark

The thrombus formation simulation starts at 12 seconds from the steady-state flow solution. A Reynolds number of 490 is chosen to be consistent with in-vitro results in Taylor et al. [162] and numerical simulations in Taylor et al. [161]. To test the performance of numerical simulations, the reattachment length R_L at the back of the step for four Reynolds numbers is compared to the numerical results of Biswas et al. [20]. For this comparison, the expansion ratio of $1 + S/2R = 2$ is adopted. The Reynolds number Re is computed as in Eq. (3.21), with hydraulic diameter equal to $4R$, blood density $\rho = 1060\,\text{kg/m}^3$, and blood viscosity $\eta = 4.7 \times 10^{-3}\,\text{m}^2/\text{s}$ [161]. The inlet velocity is spatially averaged over the inlet diameter and indicated as $\overline{u}_x$. Fig. 5.2 shows that the present results are in good agreement with the benchmark solutions [20]. Mesh and time-step sensitivity analysis resulted in $20\,000$ elements and a time-step of $0.005\,\text{s}$.
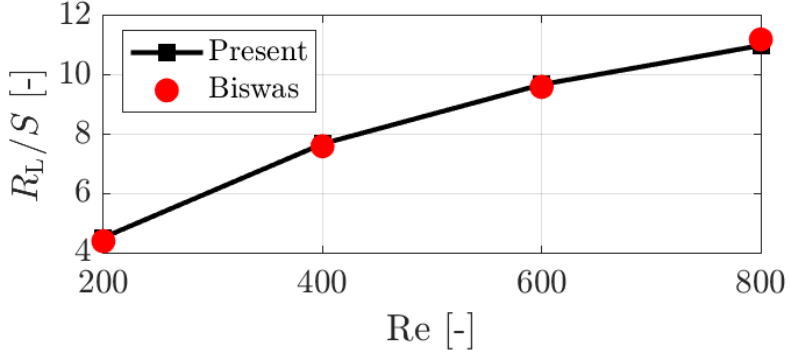
Figure 5.2.: Normalized reattachment length with respect to step height versus Reynolds number. The results are validated with the results of Biswas et al. [20]. Figure readapted from Melito et al. [103].
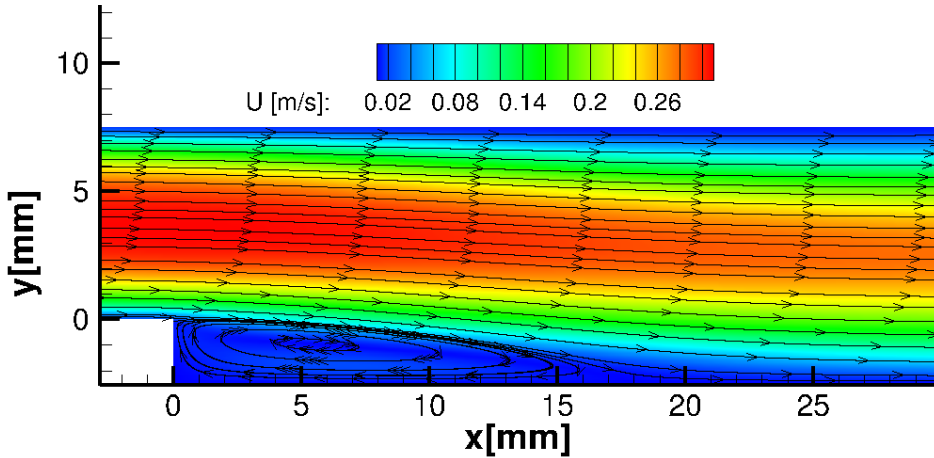
Figure 5.3.: Streamlines and magnitude of velocity indicating recirculation at the back of the step. Figure readapted from Melito et al. [103].

In Fig. 5.3, the recirculation area behind the step is highlighted by the streamlines superposed on a density plot of the magnitude of the fluid velocity. The model predicts thrombus formation in the recirculation area behind the step which qualitatively matches with in-vitro results in Taylor et al. [162] and numerical simulations in Taylor et al. [161], see Fig. 5.4.

The model adopted here is, however, invariant in time. Therefore the time averaging of the model quantities is neglected. OpenFOAM software is used for solving the blood flow and thrombus formation equations. The blockMesh utility in OpenFOAM is used for generating a structured hexahedral mesh. Blood is modeled as a Newtonian fluid. The geometry is characterized by a step depth of $S = 2.5\,\mathrm{mm}$, inlet height $2R = 7.5\,\mathrm{mm}$, and a total length $L = 120\,\mathrm{mm}$.
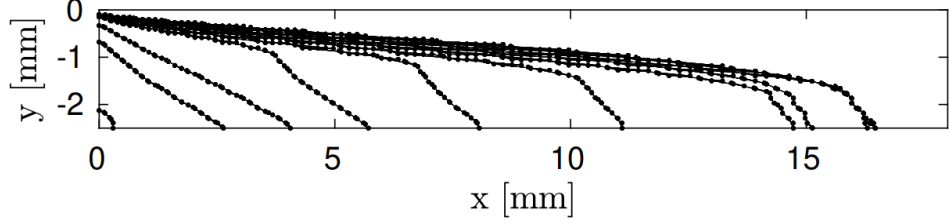
Figure 5.4.: Evolution of thrombus in time at the back of the step. The thrombus has reached 16 mm length in 50 s. Figure readapted from Melito et al. [103].

5.2.5. Sensitivity analysis

The analysis aims to identify which are the model factors that influence the produced thrombus the most. The sensitivity analysis is employed in this study, particularly the variance-based method with the aid of a surrogate model PCE for each output. Only the first- and the total-order indices, S_i and S_i^{T}, are used in this application, both for a scalar and vectorized output.

Each model input factor is treated as a uniformly distributed random variable on a given interval since their actual values and distributions are unknown, see Tab. 5.2. The sample is produced with LHS sampling techniques with size N_s equal to 450. The number of simulations is bounded by the high computational cost of the model and fulfills the requirements for the construction of the PCE. The latter is solved with the regression LARS method through the Matlab toolbox UQlab [99], where the polynomial degree is set to 3.

5.3. Application

The input parameters that are considered to represent uncertainty are listed in Tab. 5.2. To adequately cover and understand the sensitivity of thrombus formation on the selected parameters, the volume fraction of the thrombus, the thrombus growth rate, and a characteristic growth time t_c are considered the quantities of interest. The volume fraction of thrombus expressed as a percentage is defined as

$$\overline{\phi}_{\mathrm{th}}(t) = \frac{1}{\Omega} \int_{\Omega} \phi_{\mathrm{th}}(x, y, z, t) \mathrm{d}\Omega \cdot 100 \ , \tag{5.11}$$

where Ω is the domain volume and the thrombus growth rate ($\% \, \mathrm{s}^{-1}$) as

$$\dot{\overline{\phi}}_{\mathrm{th}}(t) = \frac{\mathrm{d}}{\mathrm{d}t} \left(\overline{\phi}_{\mathrm{th}}(t) \right) \ . \tag{5.12}$$

It seems promising to introduce an indicator that describes the development of the thrombus in time. This indicator could improve model fitting to experimental data, introduce a time scale in thrombus growth, or both. Therefore, a characteristic growth time t_c is therefore introduced, which is defined by the maximum peak of the thrombus growth rate, thus the time after which
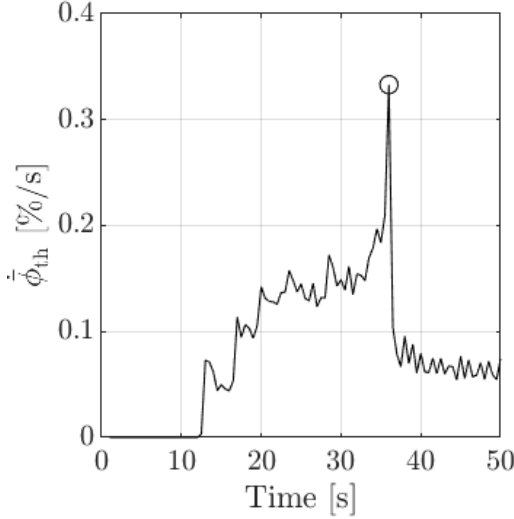
Figure 5.5.: Example of thrombus growth rate in time. A black circle indicates the characteristic growth time t_c. Figure readapted from Melito et al. [103].

the thrombus growth rate decreases significantly. At t_c, the thrombus formation is considered almost complete, and the thrombus is said to be developed, i.e., its volume will no longer change significantly in time. An example of t_c identification is illustrated in Fig. 5.5, where the growth rate of one typical simulation is plotted over the simulation time. The characteristic growth time t_c is unique for each simulation. However, not all simulations reached a growth rate peak in the simulation time, preventing the assignment of the characteristic growth time. Such simulations were excluded from the sensitivity analysis.

The developed thrombus and its characteristic growth time are directly connected. Acceleration or deceleration of the thrombus formation results in a variation of t_c in the model. For an in-depth understanding of the growth characteristics, this relationship should be analyzed in detail.

5.4. Results and discussion

The sensitivity indices S_i and S_i^{T} for the maximum volume fraction of thrombus are listed in Tab. 5.3. By looking at the first column, one observes that the first-order sensitivity indices do not sum up to one, which occurs in the presence of non-additive model behavior. Circa 90% of the output variance can be attributed to c_{BPt}, k_{BP}, and c_{AP}. The bounded platelets threshold c_{BPt} accounts alone, i.e., without considering interactions, for about 64% of the volume fraction variation of thrombus. By subtracting the first-order from the total-order indices of Tab. 5.3, the interaction effect is estimated.

Since the thrombus develops in time, it is essential to understand how its development evolves in time. The results show several trends (Fig.s 5.6 and 5.7). Increasing variability in time is

Table 5.2.: Input parameters of the thrombus model and their probabilistic distribution used for the sensitivity analysis. All input parameters follow a uniform probability distribution on the indicated interval. Table readapted from Melito et al. [103].

	Notation	$p(x_i)$	Unit
Activated platelets concentration	c_{AP}	$\mathcal{U}[1 \times 10^{-10},\ 1 \times 10^{-6}]$	mol/m^3
Coagulant diffusivity	D_c	$\mathcal{U}[2 \times 10^4,\ 2 \times 10^6]$	m^2/s
Coagulant kinetic constant	k_c	$\mathcal{U}[8 \times 10^{-11},\ 8 \times 10^{-9}]$	mol/m^3/s
Bounded platelets reaction rate	k_{BP}	$\mathcal{U}[1000,\ 100\,000]$	mol/m^3/s
Coagulant concentration threshold	c_{ct}	$\mathcal{U}[2000,\ 200\,000]$	mol/m^3
Bounded platelets concentration threshold	c_{BPt}	$\mathcal{U}[0.1,\ 3]$	mol/m^3
Coagulant kinetic constant at wall	k_{cw}	$\mathcal{U}[100,\ 100\,000]$	mol/m^3/s
Residence time threshold	T_{Rt}	$\mathcal{U}[0.75 \times 10^{13},\ 2.25 \times 10^{13}]$	-
Bounded platelets concentration threshold at wall	c_{BPwt}	$\mathcal{U}[100,\ 250\,000]$	mol/m^3

visible, especially towards the end of the simulation time. In Fig. 5.6, at 50 s of simulation time, the distribution of the recorded maximum volume fraction of thrombus varies from the absence of thrombus to a thrombus coverage of circa 30 % of the volume domain. Such variability is critical for a model in which the computation of the thrombus volume is an important goal.

The results of the generalized total-order indices for the volume fraction of thrombus and the thrombus growth rate are shown in Fig 5.8. The sensitivity analysis results do not differ for the two quantities of interest in Eq.s (5.11) and (5.12); therefore, only one plot is shown. Furthermore, the first-order index does not display a trend that differs from the total-order index, suggesting a low degree of interaction between the input random variables [104]. In Fig 5.8, the sensitivity analysis of the volume fraction of thrombus and thrombus growth rate in time shows the significant influence of the bounded platelets concentration threshold c_{BPt}. Besides this, only the bounded platelets reaction rate k_{BP} shows a comparably strong effect on the volume fraction of the thrombus.

The other input random variables mostly have a small or negligible effect on the output and might be model constants. The only exception is the significant role of the residence time threshold T_{Rt} in the early stage of thrombus initiation. However, this parameter is responsible primarily for sparking off the formation of the thrombus, while its effect on the final thrombus

Table 5.3.: Sobol indices of the input random variables on the maximum volume fraction of thrombosis. Table readapted from Melito et al. [103].

	S_i	S_i^{T}	$S_i^{\mathrm{T}} - S_i$
c_{BPt}	0.638	0.730	0.093
k_{BP}	0.198	0.277	0.078
c_{AP}	0.043	0.060	0.017
D_{c}	0.012	0.017	0.004
$\mathrm{T_{Rt}}$	0.007	0.014	0.007
k_{cw}	0.001	0.008	0.007
c_{BPwt}	0	0.005	0.004
c_{t}	0	0.005	0.005
k_{c}	0	0.001	0.001
Total	0.900	1.117	0.218

size is also negligible. The influence of the coagulant diffusivity D_{c} shows a small peak right after the first formation of the thrombus but remains low throughout the simulation time.

As may be read from Eq. (5.1), bounded platelets are generated from activated platelets in areas with low shear rate, high residence time, and high coagulant concentration. The bounded platelets can stop the flow if their concentration is sufficiently higher than the threshold value, c_{BPt}. Any variation of the bounded platelets concentration threshold will significantly change the process of thrombus formation, i.e., it essentially controls where and how fast the thrombus can form. Moreover, the reaction rate k_{BP} determines how fast the concentration of bounded platelets may reach the threshold value c_{BPt}.

The interconnected roles of the two parameters k_{BP} and c_{BPt} on thrombus formation advocate the idea that there might be a correlation between these parameters and a characteristic time of the thrombus formation process. A sensitivity analysis is also performed for this quantity of interest to verify if the characteristic growth time t_{c} is the right candidate for characterizing the thrombus growth rate.

The sensitivity analysis results for the characteristic growth time t_{c} of the thrombus are shown in Fig. 5.9. Here, the sensitivity indices are shown in a bar plot, where the first- and total-order indices are shown side-by-side to highlight the presence of potential interactions, given by their difference in value. The main parameters affecting the shift in t_{c} are the bounded platelets concentration threshold c_{BPt} and the bounded platelets reaction rate k_{BP}.

From the sensitivity analysis results for t_{c} in Fig. 5.9, the characteristic growth time is a function of c_{BPt} and k_{BP}. Because a high threshold c_{BPt} delays thrombus growth, while a high reaction rate k_{BP} has an accelerating effect, the ratio between them is introduced as a

5. On thrombus formation
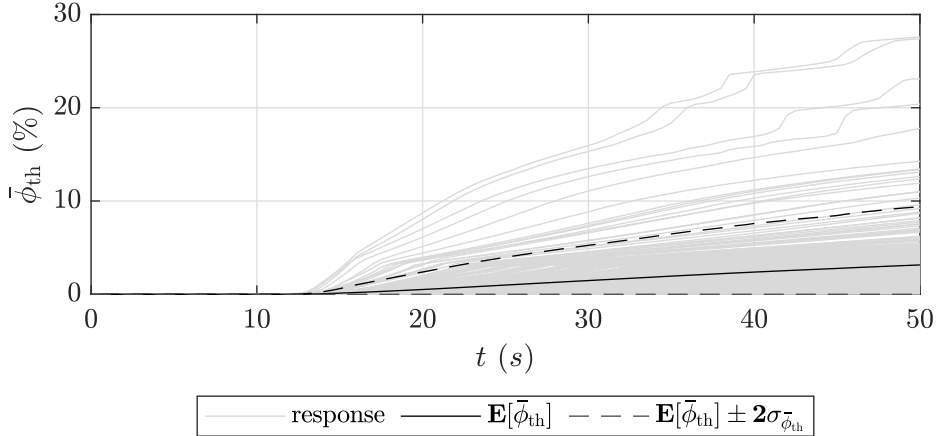
Figure 5.6.: Volume fraction of thrombus. The continuous line shows the mean value; the dashed line represents the 2 standard deviations of the data. Figure readapted from Melito et al. [103].
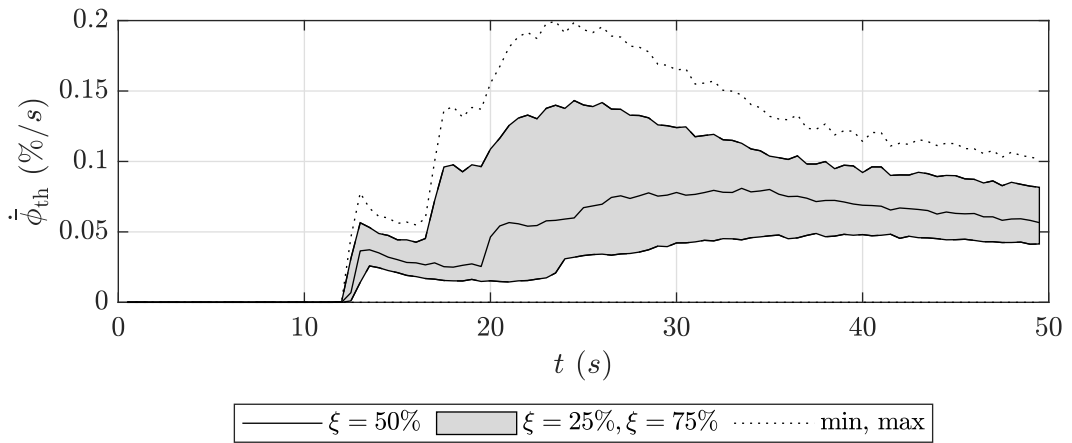
Figure 5.7.: Thrombus growth rate in time. The central continuous black line identifies the median value; the gray area represents the interquartile range; the dotted lines are the maximum and minimum data points. Figure readapted from Melito et al. [103].

characteristic growth rate $\dot{\Phi}_c$ of the model,

$$\dot{\Phi}_c = \frac{k_{BP}}{c_{BPt}} \ , \tag{5.13}$$

with the dimension of a cubic meter per second (m^3/s). Its relationship to the characteristic growth time t_c is shown in Fig. 5.10. Here, the data are produced with the computation of the metamodel for the characteristic growth time considering all input parameters, except for c_{BPt} and k_{BP}, as constants. The data was fit with non-linear regression. A low value of the characteristic growth rate $\dot{\Phi}_c$ leads to high values of t_c, which can be interpreted as delayed thrombus growth. Such behavior is a consequence of a low value of bounded platelets reaction
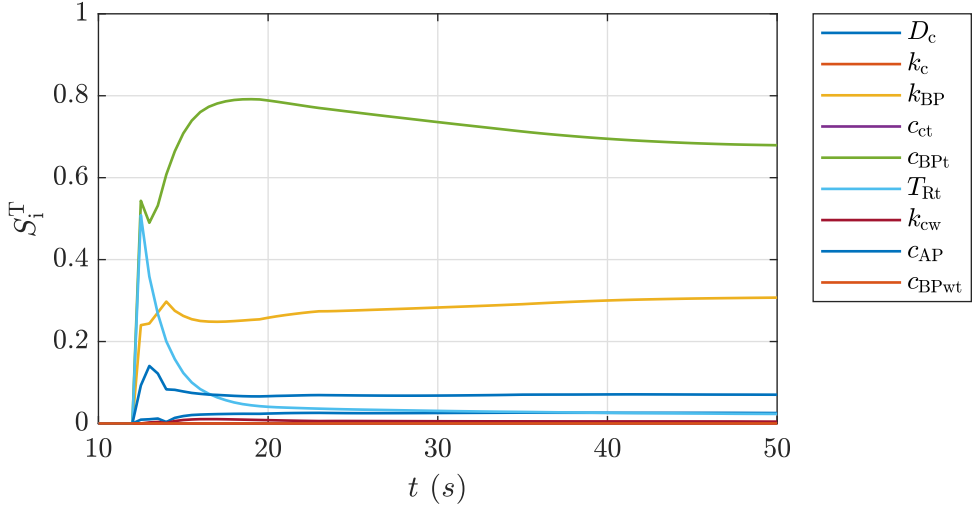
Figure 5.8.: Generalized total Sobol index for the volume fraction of thrombus $\overline{\phi}_{\text{th}}(t)$. Figure readapted from Melito et al. [103].
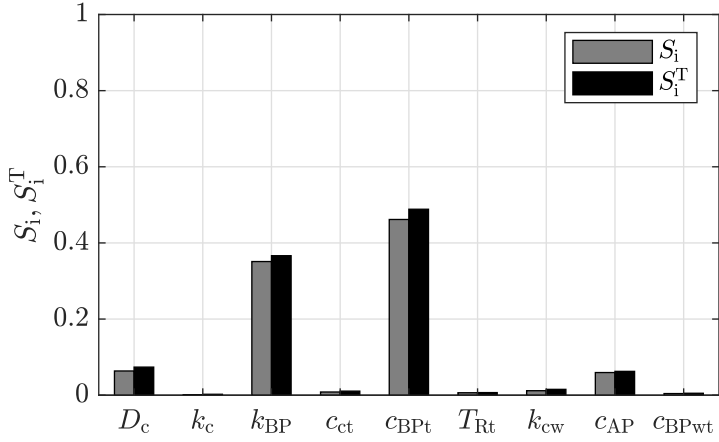
Figure 5.9.: Sensitivity analysis results for the characteristic growth time of thrombus t_c. Figure readapted from Melito et al. [103].

rate k_{BP}, and a high bounded platelets concentration threshold c_{BPt}. In the case of high c_{BPt}, the required number of bounded platelets to form a thrombus has to be higher, reducing its growth.

The data have been fitted by

$$t_c \frac{\overline{u}_x}{2\text{R}} = a \left(\frac{\dot{\Phi}_c}{Q} \right)^b , \qquad (5.14)$$

where $\overline{u}_x/2\text{R}$ is the model convection time given by the ratio of inlet velocity magnitude $\overline{u}_x$ and inlet height 2R, $Q_{\text{s}} = \overline{u}_x * A$ is the volumetric flow rate, where the area A is the product of inlet height 2R and geometry depth 1 m. The constants a and b are computed by non-linear regression

5. On thrombus formation
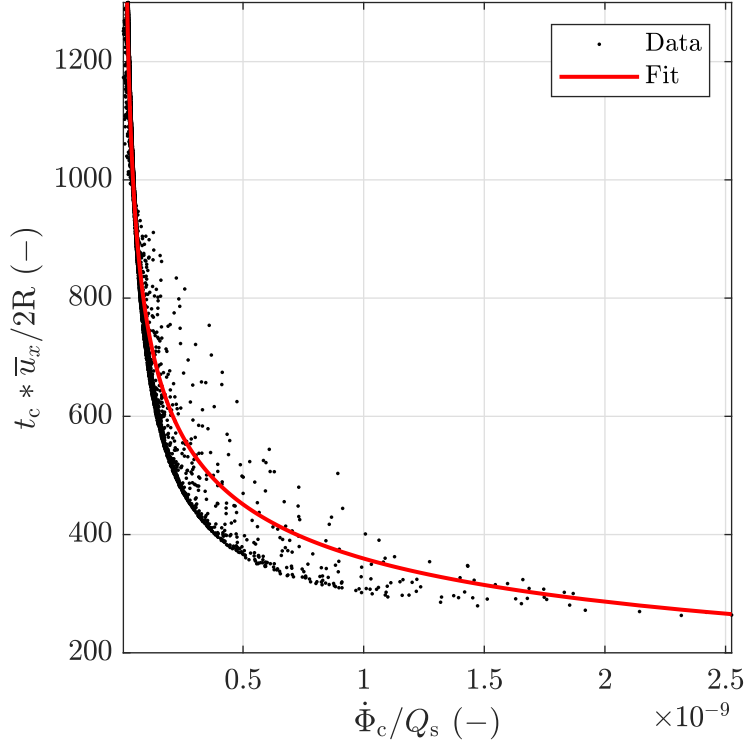
Figure 5.10.: Variation of characteristic growth time of thrombus t_c normalized by convection time $\overline{u}_x/2R$ as a function of the characteristic growth rate $\dot{\Phi}_c$ normalized by volumetric flow rate Q_s. Figure readapted from Melito et al. [103].

analysis. Their values, together with their $95\,\%$ confidence intervals, are: $a = 0.33 \pm 2.21 \times 10^{-2}$, and $b = -3.36 \times 10^{-1} \pm 2.80 \times 10^{-3}$. The coefficient of determination $R^2 = 0.93$.

Such a formulation of the characteristic growth time of the thrombus appears as a promising tool for the modeling phase. By varying the characteristic growth rate of the problem, it is possible to accelerate or inhibit the thrombus formation.

Part III.

Conclusions

6. Conclusions and outlook

In this chapter, the conclusion of the various studies is exposed. Further conclusions on the role of sensitivity analysis in the medical engineering field is left in the last section, as a conclusive remark to the work that has been produced.

6.1. On model assumptions for electrical conductivity of flowing blood

The study described in Chapter 3 showed how to reduce the uncertainty of electrical conductivity of flowing blood and analyzed the impact of different model assumptions on such blood property. The conductivity model is coupled with three different fluid mechanics model assumptions: *i.* Newtonian fluid and steady flow, *ii.* Newtonian fluid and harmonically pulsating flow, *iii.* non-Newtonian fluid and harmonically pulsating flow. A global sensitivity analysis is performed within fluid mechanics models to understand the impact of such assumptions better. Given the study's scope to reduce the variability in the model outputs, a variance-based method and a surrogate model, i.e., polynomial chaos expansion, are employed. The surrogate model is solved either with ordinary least squares or with the least-angle regression, which selection is due to the computational cost of each model assumption. The computation of the Sobol indices as quantitative measures of input factors sensitivity is performed through the solution of the surrogate model. Other sensitivity analysis methods, e.g., non-parametric or density-based, are discarded from this study due to the undefined behavior of the model before the analysis.

Two outputs are considered quantities of interest: the average value over one cardiac cycle of the blood conductivity change and its amplitude, namely $\langle \Delta\sigma_{\text{bl}} \rangle$ and $\Delta\hat{\sigma}_{\text{bl}}$. Initial analysis of the distribution of the results underlines the inability of a steady flow model assumption in representing the natural behavior of the blood conductivity changes and, as might be expected, its amplitude response. Therefore, a steady flow model assumption is left out from the sensitivity analysis and considered inadequate for the aim of the study.

The sensitivity analysis shows that the hematocrit level of the blood generally has the highest effect on the average value of the conductivity change of blood for both a Newtonian and non-Newtonian formulation of the fluid in a pulsating flow domain. The theoretical formulation of the problem confirms this result. It is indeed evident the effect that non-conductive red blood cells have on the computation of blood conductivity. However, switching to a shear-thinning generalized model for the computation of the conductivity change amplitude, the effect of the hematocrit level loses its influence dominance in favor of the flow rate ratio between pulsating and steady

flow and the undeformed RBCs axes ratio. This change in model mechanics better represents the physicality of the electrical characteristics of blood. The non-Newtonian formulation enables a different path for the computation of the blood conductivity changes, emphasizing the effect of the flow's pulsation and the RBCs' patient-specific characteristics on the outcome. The latter random variable was demonstrated to be more influential than the hematocrit level, contrary to the common belief that hematocrit represents the driving force of conductivity variation. In conclusion, given the different results from the sensitivity analysis for the two model responses, the choice of the quantity of interest for any further computation has to be thoughtfully considered. Further development of the flow model, including physiologically accurate volumetric flow rates and pipe wall elasticity, may deepen these investigations and initiate new scientific challenges.

6.2. On configuration optimization in ICG

In Chapter 4, a preliminary study is initially performed on the effect of an impedance cardiography model in detecting blood volumes changes caused by aortic dissection. The study aims at detecting the highest impedance variation given by the signal oscillations, typical of the human body. A simple model is developed in the software COMSOL multiphysics, including the thorax and the aorta affected by aortic dissection. In the preliminary study, two sensitivity analysis methods are employed to eliminate most of the input uncertainties. An initial screening is performed with the elementary effect method. Then, the resulting most influential variables are analyzed with the variance-based method, particularly with the aid of a polynomial chaos expansion. Since the variance-based method becomes complex for many random variables, such an approach is highly recommended.

During a deep analysis of the model's needs, the uncertainty is imposed on some input variables. They are successively divided into the following groups. The geometric variables vary the radius of the aortic arch, the radius of the true and false lumen, and the plane angle between the lumina. The physical-electrical variables include a blood velocity variable, the hematocrit of blood, and the conductivities of blood and thorax. The first group is shown to affect the impedance measurement more than the second group of physical-electrical variables. This result is justified by the nature of the methodology, i.e., impedance cardiography, which focuses precisely on blood volumetric changes. The computational model of the thorax with TL and FL can be defined as suitable, or verified, for the identification of AD because it is sensitive to geometric changes produced precisely by the FL.

In summary, the variables that produce the most outcome variation are the radius of the FL, the relative position of the FL to the aorta, the value of electrical conductivity assigned to the thorax, and finally, the variation of the radius of the TL. These results are taken into account to increase the model's complexity and implement new geometries in the thorax, such as the lungs and the heart. The following modeling steps consider the illustrated results, increasing the awareness of the modeler about the inherent model uncertainty before the next modeling phase.

The subsequent study examines different electrode configurations for measuring the discrepancy in impedance cardiography measurements between healthy and type B aortic dissection patients.

For this purpose, a numerical simulation model is set up using a simplified chest geometry taken from the previous study. A global sensitivity analysis on the computed signal is implemented to quantify the model output variance, due to the many uncertainties regarding the model parameters. Sensitivity analysis of the model output shows that the highest difference in impedance cardiograms between healthy and diseased patients occurs when the velocity is highest in the aorta, i.e., during the systolic peak produced by the heart.

To define how the maximum cardiographic impedance value varies between healthy and diseased patients is necessary to determine the electrode configuration with the highest likelihood of identifying aortic dissection. As the analysis results, the most significant outcome variation is verified with injection sensors at the front and back of the chest with measuring sensors in their vicinity. Such a conclusion is reached by analyzing the highest outcome variation produced by different electrode configurations. As known, the imposed input uncertainty drives this model fluctuation. Therefore, the focus of the analysis is on the outcome with the most significant variation. Hence, a sensitivity analysis of the input parameters is performed for the mentioned electrode configurations to discover which output is most affected by the FL radius variable.

It has already been verified that the size of the false lumen has an enormous effect on the impedance cardiogram in patients with type B aortic dissection. Indeed, pathological changes caused by the FL can result in various hemodynamic conditions, easily measured by impedance cardiography rather than by other methods. In the course of aortic dissection, events like false lumen expansion and false lumen thrombosis cause pathological changes that alter the measured impedance cardiogram. Thus, applying impedance cardiography to track pathological changes can be helpful for the medical management of this disease. Future works will consider the electrical conductivity changes of the blood in the case of disturbed aortic flow. The possibility of tracking false lumen thrombosis by impedance cardiography will be investigated in future studies.

6.3. On thrombus formation model

Thrombus formation in aortic dissection represents a critical topic, as it can easily represent a benefit or a problem for the patient and his clinical condition. Thrombus modeling is currently a challenge in the engineering field due to the lack of data on which to rely and reconstruct the thrombus growth system.

Some models of thrombus formation do exist, and the one used in this manuscript is phenomenological, meaning that no biochemical reactions are modeled. The employed model has high variation due to the inherent uncertainty of the input parameters, which are usually collected from different sources in the literature. The input variation is modeled with uniform probability distributions for nine random model input variables, and a sensitivity analysis is performed by constructing a polynomial chaos expansion surrogate. The quantities of interest are the thrombus volume fraction, the thrombus growth rate, and the instant at which the peak of the growth rate is recorded, i.e., the characteristic growth time.

Input parameters such as the bound platelet reaction rate and the activated platelet concentration threshold show high sensitivity indices. Therefore, although determining their exact value

undoubtedly requires very complex investigations, they considerably reduce model uncertainty when adequately assessed. In general, input parameters involving platelet mechanics control most of the process, except for the concentration of bounded platelets at the wall.

All other random input variables, including coagulant-related parameters, have little or no influence on the considered outputs and thus can be assumed as constants without altering the model response. The sensitivity analysis results for the model outputs show that the threshold of bounded platelets concentration exerts the most substantial influence. The reaction rate of bounded platelets plays the second most crucial role in thrombus growth rate and volume fraction.

These results are, of course, significant for the proper calibration of the model. Despite these results, this model is still based on phenomenological aspects, and consequently, it is difficult to determine the accuracy of the terminology used for the various input parameters. However, this model can adequately represent thrombus formation, especially in FL; therefore, the sensitivity results are undoubtedly helpful to improve the computational model.

Calibration of this model remains a very desirable goal in this scientific field. Therefore, thanks to the isolation of the most sensitive variables of the model, it was possible to define the characteristic growth rate given by the ratio between the reaction rate and the concentration threshold of bounded platelets. This new quantity seems to be a promising indicator for the rate of thrombus formation. This characteristic rate should be helpful in fitting model results to experimental results, improving the hemodynamics-based model in predicting thrombus formation on an appropriate time scale.

6.4. General conclusions and remarks

In this thesis, sensitivity analysis solved essential questions that often plague modelers and engineers when developing new analytical or numerical models, especially in medical engineering. Models are necessary to fit experimental results in medical engineering and provide reliable statistical information about a given phenomenon. However, it is interesting to note that building a model requires statistical input and output information. In medicine, such information is usually complex to obtain.

The engineering field often successfully implements appropriate solutions that greatly simplify the diagnosis and treatment of various diseases through the assumption of such simplifications. It has been seen that a link between physicians and engineers is often challenging to obtain. There is a rampant skepticism of computational models in the medical field. This is understandable considering that formulated models are often built on simplifying assumptions and that different scientific background is sometime insurmountable.

Sensitivity analysis comes into play by reinforcing a link that can bring the two scientific fields closer together. On the one hand, it pushes computational models to higher performance through statistical information, i.e., reducing uncertainty and identifying uncertainty propagation paths within the model. On the other hand, it creates a more accessible environment for clinicians to analyze models more familiarly, i.e., through statistics. Unfortunately, sensitivity analysis

is a relatively new scientific field and consequently struggles to emerge as an interdisciplinary medium.

Patient-specific models are having great success in the medical and biomechanical fields because of the ability to obtain data from an individual patient and compare it to the model itself. Fine-tuning of initial parameters is essential in these cases. These models are very accurate in representing a specific disease condition or patient but, unfortunately, lack the flexibility to investigate the disease problem from a broader perspective. Customization (or personalization) of models underestimates the implementation of sensitivity analysis in the modeling process. In this process, the focus is on tuning a minimal set of parameters, often singularly, rather than the entire input domain.

This thesis shows that sensitivity analysis can enter the modeling cycle by analyzing the intrinsic mechanics of the model. In sensitivity analysis and uncertainty quantification, models are often considered *black boxes*, similar to machines that produce a finished product given a specific initial input. Formalizing the problem in this way can be quick for the analyst who does not have to delve into the depths of mathematical formulations, although at the same time, it may leave out critical constructive details of the model. Typically, any computational model must undergo a rigorous verification and validation process before being used in any scientific field. This assumption is maintained in this text, and the notion of a black box treats this feature as guaranteed.

The process of modeling natural systems can be conducted in various ways. Many models are created based on concepts and assumptions observed by the modeler and linked together by mathematical formulations. Such models are called "physics-based models" and must follow a rigid creation process. In this process are included the verification and validation phase. The first one is to check that the mathematical implementation reflects the developer's intended concept. The second phase of validation controls how much the model, when used for the prefixed scope, is approached to represent reality. These phases, when satisfied, are usually followed by a further phase of calibration and experimentation.

It has been seen that sensitivity analysis can enter the production cycle of a computational model at an early stage to quantify the weight of different hypotheses. As in the case of the blood electrical conductivity study, this mathematical tool can analyze and quantify the influence of several primary hypotheses. In this study, the focus was on the fluid type and flow hypothesis. In engineering, one is always looking for alternative and simplified solutions to model reality, as these are easier to calculate. However, in this specific case, these simplifications are disadvantageous in calculating the electrical conductivity of blood. Consequently, it is better to consider blood as a non-Newtonian fluid, especially in the case of pulsating flow.

Nowadays, the advancement of technology and computer science makes it possible to accumulate and save an enormous amount of data about various aspects of life. We often hear that we now live in the "data age." In this context, it is possible to create computational models that, instead of being based on assumptions and notions, are created by analyzing large amounts of data. Such models are referred to as "data-driven models." After collecting the data, it is cleaned and organized, classified, and regressed to extract the necessary features.

6. Conclusions and outlook

Sensitivity analysis in this thesis has been applied only to physical models derived from observations or intuitions and not measurements. Some of the models illustrated are unfortunately still very young and are in a weak state of validation, which is necessary to continue towards the experimental phase. Therefore, the sensitivity analysis has been used as a tool to support modeling. As noted by the framework illustrated in the introduction, a process of uncertainty quantification and sensitivity analysis should be carried out iteratively with the aim of reducing the variability of the model under study as much as possible. In some of the cases illustrated, such iteration has not been possible as there is a lack of experimental data related to the studied phenomenon that could validate or not such models.

Of course, creating data-driven models would be an advantage as many aspects of reality could be implemented. Reality, human body, and natural phenomena include a high complexity and multi-modality that is often difficult to describe with physics-driven models. Unfortunately, at the same time, in the medical field, it is not easy to obtain a large number of measurements and data. The need to respect the ethical value of patients and doctors slows down and complicates the process of data assimilation, and subjecting patients to lengthy data collection treatments is often inappropriate.

The optimal situation would be to have limited but sufficient medical measurements available to validate and calibrate the presented models. Also, especially in the medical field, it is difficult to identify the parameters that lead to certain conditions or pathologies of a patient due to the high human variability. Consequently, appropriate use of sensitivity analysis must be introduced, including verifying the domain in which the model will operate.

The implementation of sensitivity analysis also allows for creating a new concept, such as that of virtual patients. This concept is based on creating data that might reflect a particular disease condition and a random patient. The data, or sampling, results from the simple implementation of uncertainty quantification and sensitivity analysis in the modeling phase, as the level of variability is imposed to analyze the variation in the system in question. Each combination of inputs truly represents a hypothetical medical patient. Therefore, the model increases its power of diagnosis and prediction.

In the future, the models analyzed in this text must undergo a rigorous validation and calibration process. In this way, we can move in a direction in which these tools can be used as a resource in detecting or monitoring TBAD. Before achieving this, it has been seen that the use of sensitivity analysis as a tool aimed at deep model analysis has led to a significant reduction in model uncertainty.

Bibliography

[1] Brian M Adams, William J Bohnhoff, Keith R Dalbey, JP Eddy, MS Eldred, DM Gay, K Haskell, Patricia D Hough, and Laura P Swiler. Dakota, a multilevel parallel object-oriented framework for design optimization, parameter estimation, uncertainty quantification, and sensitivity analysis: version 5.0 user's manual. *Sandia National Laboratories, Tech. Rep. SAND2010-2183*, 2009.

[2] Jordi Alastruey, Nan Xiao, Henry Fok, Tobias Schaeffter, and C Alberto Figueroa. On the impact of modelling assumptions in multi-scale, subject-specific models of aortic haemodynamics. *Journal of The Royal Society Interface*, 13(119):20160073, 2016.

[3] Alen Alexanderian, Pierre A Gremaud, and Ralph C Smith. Variance-based sensitivity analysis for time-dependent processes. *Reliability Engineering & System Safety*, 196:106722, 2020.

[4] Daniel B Alfson and Sung W Ham. Type b aortic dissections: current guidelines for treatment. *Cardiology clinics*, 35(3):387–410, 2017.

[5] Luis Altamirano-Diaz, Eva Welisch, Adam A Dempsey, Teresa Sohee Park, Michael Grattan, and Kambiz Norozi. Non-invasive measurement of cardiac output in children with repaired coarctation of the aorta using electrical cardiometry compared to transthoracic doppler echocardiography. *Physiological measurement*, 39(5):055003, 2018.

[6] Luis Altamirano-Diaz, Andrea D Kassay, Baran Serajelahi, Christopher W McIntyre, Guido Filler, and Sanjay R Kharche. Arterial hypertension and unusual ascending aortic dilatation in a neonate with acute kidney injury: mechanistic computer modeling. *Frontiers in physiology*, 10:1391, 2019.

[7] M Anand, K Rajagopal, and KR Rajagopal. A model incorporating some of the mechanical and biochemical factors underlying clot formation and dissolution in flowing blood. *Journal of Theoretical Medicine*, 5(3-4):183–218, 2003.

[8] George E Andrews and Richard Askey. Classical orthogonal polynomials. In *Polynômes orthogonaux et applications*, pages 36–62. Springer, 1985.

[9] R Askey and J Wilson. Some basic hypergeometric polynomials that generalize jacobi polynomials (memoirs of the american mathematical society, 319). *American Mathematical Society, Providence, RI*, 1985.

Bibliography

[10] V. Badeli, G. M. Melito, A. Reinbacher-Köstinger, O. Bíró, and K. Ellermann. Electrode positioning to investigate the changes of the thoracic bioimpedance caused by aortic dissection – a simulation study. *Journal of Electrical Bioimpedance*, 11(1):38–48, 2020. doi: doi:10.2478/joeb-2020-0007. URL `https://doi.org/10.2478/joeb-2020-0007`.

[11] Vahid Badeli, Alice Reinbacher-Köstinger, Oszkar Biro, and Christian Magele. Numerical simulation of impedance cardiogram changes in case of chronic aortic dissection. In *International Conference on Electrical Bioimpedance*, pages 55–59. Springer, 2019.

[12] Jean-Pierre Barral and Alain Croibier. 2 - circulatory physiology. In Jean-Pierre Barral and Alain Croibier, editors, *Visceral Vascular Manipulations*, pages 27–45. Churchill Livingstone, Oxford, 2011. ISBN 978-0-7020-4351-2. doi: https://doi.org/10.1016/B978-0-7020-4351-2. 00002-8.

[13] Tushar Kanti Bera. Bioelectrical impedance methods for noninvasive health monitoring: a review. *Journal of medical engineering*, 2014, 2014. doi: 10.1155/2014/381251.

[14] Yvette Bernard, Hugues Zimmermann, Sidney Chocron, Jean-François Litzler, Bruno Kastler, Joseph-Philippe Etievent, Nicolas Meneveau, François Schiele, and Jean-Pierre Bassand. False lumen patency as a predictor of late outcome in aortic dissection. *The American journal of cardiology*, 87(12):1378–1382, 2001.

[15] Donald P Bernstein. Impedance cardiography: Pulsatile blood flow and the biophysical and electrodynamic basis for the stroke volume equations. *Journal of Electrical Bioimpedance*, 1(1):2–17, 2010.

[16] Donald P Bernstein and HJM Lemmens. Stroke volume equation for impedance cardiography. *Medical and Biological Engineering and Computing*, 43(4):443–450, 2005.

[17] M Berveiller, B Sudret, and M Lemaire. Presentation of two methods for computing the response coefficients in stochastic finite element analysis. In *Proc. 9th ASCE Specialty Conference on Probabilistic Mechanics and Structural Reliability, Albuquerque, USA*, 2004.

[18] Marc Berveiller, Bruno Sudret, and Maurice Lemaire. Stochastic finite element: a non intrusive approach by regression. *European Journal of Computational Mechanics/Revue Européenne de Mécanique Numérique*, 15(1-3):81–92, 2006.

[19] R. B. Bird, R. C. Armstrong, and O. Hassager. *Dynamics of Polymeric Liquids - Volume 1 Fluid Mechanics*. A Wiley-Interscience puplication, 1987. ISBN 978-0-471-80245-7.

[20] Gautam Biswas, Michael Breuer, and Franz Durst. Backward-facing step flows for various expansion ratios at low and moderate reynolds numbers. *J. Fluids Eng.*, 126(3):362–374, 2004.

[21] M Bitbol and F Leterrier. Measurement of the erythrocyte orientation in a flow by spin labeling. *Biorheology*, 19(6):669–680, 1982. doi: 10.3233/BIR-1982-19601.

[22] M. Bitbol and D. Quemada. Measurement of erythrocyte orientation in flow by spin labeling. *Biorheology*, 22(1):31–42, 1985. doi: 10.3233/BIR-1985-22103.

[23] Géraud Blatman and Bruno Sudret. An adaptive algorithm to build up sparse polynomial chaos expansions for stochastic finite element analysis. *Probabilistic Engineering Mechanics*, 25(2):183–197, 2010.

[24] Géraud Blatman and Bruno Sudret. Adaptive sparse polynomial chaos expansion based on least angle regression. *Journal of computational Physics*, 230(6):2345–2367, 2011.

[25] Aron S Bode, Wouter Huberts, E Marielle H Bosboom, Wilco Kroon, Wim PM Van der Linden, R Nils Planken, Frans N Van de Vosse, and Jan HM Tordoir. Patient-specific computational modeling of upper extremity arteriovenous fistula creation: its feasibility to support clinical decision-making. *PloS one*, 7(4):e34491, 2012.

[26] Gert Böhme. *Strömungsmechanik nicht-newtonscher Fluide (Mechanics of non-Newtonian Fluids, in German)*. B.G. Teubner-Verlag, 2000.

[27] Anna M Booher, Eric M Isselbacher, Christoph A Nienaber, Santi Trimarchi, Arturo Evangelista, Daniel G Montgomery, James B Froehlich, Marek P Ehrlich, Jae K Oh, James L Januzzi, et al. The irad classification system for characterizing survival after aortic dissection. *The American journal of medicine*, 126(8):730–e19, 2013.

[28] Emanuele Borgonovo. A new uncertainty importance measure. *Reliability Engineering & System Safety*, 92(6):771–784, 2007.

[29] Emanuele Borgonovo and George E Apostolakis. A new importance measure for risk-informed decision making. *Reliability Engineering & System Safety*, 72(2):193–212, 2001.

[30] Emanuele Borgonovo and Lorenzo Peccati. Sensitivity analysis in investment project evaluation. *International Journal of Production Economics*, 90(1):17–25, 2004.

[31] Emanuele Borgonovo and Elmar Plischke. Sensitivity analysis: a review of recent advances. *European Journal of Operational Research*, 248(3):869–887, 2016.

[32] S. Brandstaeter, S. L. Fuchs, J. Biehler, R. C. Aydin, W. A. Wall, and C. J. Cyron. Global sensitivity analysis of a homogenized constrained mixture model of arterial growth and remodeling. *Journal of Elasticity*, 145:191–221, 2021. doi: https://doi.org/10.1007/s10659-021-09833-9.

Bibliography

[33] Francesca Campolongo and Andrea Saltelli. Sensitivity analysis of an environmental model: an application of different analysis methods. *Reliability Engineering & System Safety*, 57 (1):49–69, 1997. ISSN 0951-8320. doi: https://doi.org/10.1016/S0951-8320(97)00021-5. The Role of Sensitivity Analysis in the Corroboration of Models and its Links to Model Structural and Parametric Uncertainty.

[34] Francesca Campolongo, Jessica Cariboni, and Andrea Saltelli. An effective screening design for sensitivity analysis of large models. *Environmental modelling & software*, 22 (10):1509–1518, 2007.

[35] P. J. Carreau. *Rheological equations from molecular network theories.* PhD thesis, University of Wisconsin, Madison, 1968.

[36] Jacson Purchase Medical Center. Impedance cardiography, 2021. URL `https://www.jacksonpurchase.com/heart-and-lung/impedance-cardiography`.

[37] Z Cheng, FPP Tan, CV Riga, CD Bicknell, MS Hamady, RGJ Gibbs, NB Wood, and XY Xu. Analysis of flow patterns in a patient-specific aortic dissection model. *Journal of Biomechanical Engineering*, 2010. doi: 10.1115/1.4000964.

[38] S. Chien, S. Usami, R. J. Dellenback, and M. I. Gregersen. Shear-dependent deformation of erythrocytes in rheology of human blood. *American Physiological Society*, 219(1):136–142, 1970. doi: 10.1152/ajplegacy.1970.219.1.136.

[39] Thierry Crestaux, Olivier Le Maıtre, and Jean-Marc Martinez. Polynomial chaos expansion for sensitivity analysis. *Reliability Engineering & System Safety*, 94(7):1161–1172, 2009.

[40] George J. Crystal, Sherif I. Assaad, and Paul M. Heerdt. 24 - cardiovascular physiology: Integrative function. In Hugh C. Hemmings and Talmage D. Egan, editors, *Pharmacology and Physiology for Anesthesia (Second Edition)*, pages 473–519. Elsevier, Philadelphia, second edition edition, 2019. ISBN 978-0-323-48110-6. doi: https://doi.org/10.1016/B978-0-323-48110-6.00024-7.

[41] Martin Czerny, Jürg Schmidli, Sabine Adler, Jos C van den Berg, Luca Bertoglio, Thierry Carrel, Roberto Chiesa, Rachel E Clough, Balthasar Eberle, Christian Etz, et al. Editor's choice–current options and recommendations for the treatment of thoracic aortic pathologies involving the aortic arch: an expert consensus document of the european association for cardio-thoracic surgery (eacts) & the european society for vascular surgery (esvs). *European Journal of Vascular and Endovascular Surgery*, 57(2):165–198, 2019.

[42] Pat O Daily, H Ward Trueblood, Edward B Stinson, Robert D Wuerflein, and Norman E Shumway. Management of acute aortic dissections. *The Annals of thoracic surgery*, 10(3): 237–247, 1970.

[43] Michael E De Bakey, Walter S Henly, Denton A Cooley, George C Morris Jr, E Stanley Crawford, and Arthur C Beall Jr. Surgical management of dissecting aneurysms of the aorta. *The Journal of thoracic and cardiovascular surgery*, 49(1):130–149, 1965.

[44] A De Sitter, RM Verdaasdonk, and TJC Faes. Do mathematical model studies settle the controversy on the origin of cardiac synchronous trans-thoracic electrical impedance variations? a systematic review. *Physiological measurement*, 37(9):R88, 2016.

[45] WP Donders, W Huberts, FN van de Vosse, and T Delhaas. Personalization of models with many model parameters: an efficient sensitivity analysis approach. *International journal for numerical methods in biomedical engineering*, 31(10), 2015.

[46] VG Eck, J Feinberg, HP Langtangen, and LR Hellevik. Stochastic sensitivity analysis for timing and amplitude of pressure waves in the arterial system. *International journal for numerical methods in biomedical engineering*, 31(4):e02711, 2015.

[47] VG Eck, J Sturdy, and LR Hellevik. Effects of arterial wall models and measurement uncertainties on cardiovascular model predictions. *Journal of biomechanics*, 50:188–194, 2017.

[48] Vinzenz Gregor Eck, Wouter Paulus Donders, Jacob Sturdy, Jonathan Feinberg, Tammo Delhaas, Leif Rune Hellevik, and Wouter Huberts. A guide to uncertainty quantification and sensitivity analysis for cardiovascular applications. *International journal for numerical methods in biomedical engineering*, 32(8), 2016.

[49] R. H. Edgerton. Conductivity of sheared suspensions of ellipsoidal particles with application to blood flow. *IEEE Transactions on Biomedical Engineering*, BME-21:33–43, 1974. doi: 10.1109/TBME.1974.324359.

[50] Bradley Efron and Charles Stein. The jackknife estimate of variance. *The Annals of Statistics*, pages 586–596, 1981.

[51] Jan Egger, Simon Gunacker, Antonio Pepe, Gian Marco Melito, Christina Gsaxner, Jianning Li, Katrin Ellermann, and Xiaojun Chen. A comprehensive workflow and framework for immersive virtual endoscopy of dissected aortae from CTA data. In Baowei Fei and Cristian A. Linte, editors, *Medical Imaging 2020: Image-Guided Procedures, Robotic Interventions, and Modeling*, volume 11315, pages 774 – 779. International Society for Optics and Photonics, SPIE, 2020. doi: 10.1117/12.2559239. URL `https://doi.org/10.1117/12.2559239`.

[52] Joseph Feher. 5.4 - the heart as a pump. In Joseph Feher, editor, *Quantitative Human Physiology (Second Edition)*, pages 516–524. Academic Press, Boston, second edition edition, 2012. ISBN 978-0-12-800883-6. doi: https://doi.org/10.1016/B978-0-12-800883-6.00047-1.

Bibliography

[53] Council for Regulatory Environmental Modeling. Guidance on the development, evaluation, and application of environmental models. Technical report, United States Environmental Protection Agency, 2009. URL `https://www.epa.gov/sites/default/files/2015-04/documents/cred_guidance_0309.pdf`.

[54] R. A. Frewer. The electrical conductivity of flowing blood. *Biomedical Engineering*, 9(12): 552–555, 1974.

[55] H. Fricke. A mathematical treatment of the electric conductivity and capacity of disperse systems I. The electric conductivity of a suspension of homogeneous spheroids. *Physical Review*, 24:575–587, 1924. doi: 10.1103/PhysRev.24.575.

[56] M. Fujii, K. Nakajima, K. Sakamoto, and H. Kanai. Orientation and deformation of erythrocytes in flowing blood. *Annals of the New York Academy of Sciences*, 873:245–261, 1999. doi: 10.1111/j.1749-6632.1999.tb09473.x.

[57] R. Fåhræus and T. Lindqvist. The viscosity of the blod in narrow capillary tubes. *American Physiological Society*, 96(3):562–568, 1931. doi: 10.1152/ajplegacy.1931.96.3.562.

[58] Camelia Gabriel, Sami Gabriel, and y E Corthout. The dielectric properties of biological tissues: I. literature survey. *Physics in medicine & biology*, 41(11):2231, 1996.

[59] Sami Gabriel, RW Lau, and Camelia Gabriel. The dielectric properties of biological tissues: II. measurements in the frequency range 10 hz to 20 ghz. *Physics in medicine & biology*, 41(11):2251, 1996.

[60] Sami Gabriel, RW Lau, and Camelia Gabriel. The dielectric properties of biological tissues: III. parametric models for the dielectric spectrum of tissues. *Physics in medicine & biology*, 41(11):2271, 1996.

[61] T. Christian Gasser, Ray W. Ogden, and Gerhard A. Holzapfel. Hyperelastic modelling of arterial layers with distributed collagen fibre orientations. *Journal of the royal society interface*, 3(6):15–35, 2006.

[62] Richelle L Gaw, Bruce H Cornish, and Brian J Thomas. Comparison of a theoretical impedance model with experimental measurements of pulsatile blood flow. In *13th International Conference on Electrical Bioimpedance and the 8th Conference on Electrical Impedance Tomography*, pages 32–35. Springer, 2007.

[63] Richelle L Gaw, Bruce H Cornish, and Brian J Thomas. The electrical impedance of pulsatile blood flowing through rigid tubes: an experimental investigation. In *13th International Conference on Electrical Bioimpedance and the 8th Conference on Electrical Impedance Tomography*, pages 73–76. Springer, 2007.

[64] Richelle L Gaw, Bruce H Cornish, and Brian J Thomas. The electrical impedance of pulsatile blood flowing through rigid tubes: a theoretical investigation. *IEEE Transactions on Biomedical Engineering*, 55(2):721–727, 2008. doi: 10.1109/TBME.2007.903531.

[65] Richelle Leanne Gaw. *The effect of red blood cell orientation on the electrical impedance of pulsatile blood with implications for impedance cardiography.* PhD thesis, Queensland University of Technology, 2010.

[66] Roger G Ghanem and Pol D Spanos. *Stochastic finite elements: a spectral approach.* Courier Corporation, 2003.

[67] T Giujusa, C Dario, G Risica, E Franceschini, A Carlini, A Moro, and V Cuzzato. Aortic dissection: an incidence study based on hospital cases. *Cardiologia (Rome, Italy)*, 39(2): 107–112, 1994.

[68] Shyam Sunder Gopalakrishnan, Benoît Pier, and Arie Biesheuvel. Dynamics of pulsatile flow through model abdominal aortic aneurysms. *Journal of Fluid Mechanics*, 758:150–179, 2014. doi: 10.1017/jfm.2014.535.

[69] Peter G Hagan, Christoph A Nienaber, Eric M Isselbacher, David Bruckman, Dean J Karavite, Pamela L Russman, Arturo Evangelista, Rossella Fattori, Toru Suzuki, Jae K Oh, et al. The international registry of acute aortic dissection (irad): new insights into an old disease. *Jama*, 283(7):897–903, 2000.

[70] Steven R Hanha. Air quality model evaluation and uncertainty. *Japca*, 38(4):406–412, 1988.

[71] James J Hathcock. Flow effects on coagulation and thrombosis. *Arteriosclerosis, thrombosis, and vascular biology*, 26(8):1729–1737, 2006.

[72] Jon C Helton. Uncertainty and sensitivity analysis techniques for use in performance assessment for radioactive waste disposal. *Reliability Engineering & System Safety*, 42(2): 327–367, 1993. ISSN 0951-8320. doi: https://doi.org/10.1016/0951-8320(93)90097-I.

[73] H Hinghofer-Szalkay and JE Greenleaf. Continuous monitoring of blood volume changes in humans. *Journal of applied physiology*, 63(3):1003–1007, 1987.

[74] HELMUT Hinghofer-Szalkay. Method of high-precision microsample blood and plasma mass densitometry. *Journal of Applied Physiology*, 60(3):1082–1088, 1986.

[75] Jennifer A Hoeting, David Madigan, Adrian E Raftery, and Chris T Volinsky. Bayesian model averaging: a tutorial. *Statistical science*, pages 382–401, 1999.

[76] A.E. Hoetink, T.J.C. Faes, K.R. Visser, and R.M. Heethaar. On the flow dependency of the electrical conductivity of blood. *IEEE transactions on Biomedical Engineering*, 51(7): 1251–1261, 2004. doi: 10.1109/TBME.2004.827263.

Bibliography

[77] Toshimitsu Homma and Andrea Saltelli. Importance measures in global sensitivity analysis of nonlinear models. *Reliability Engineering & System Safety*, 52(1):1–17, 1996.

[78] W. Huberts, W.P. Donders, T. Delhaas, and F.N. van de Vosse. Applicability of the polynomial chaos expansion method for personalization of a cardiovascular pulse wave propagation model. *International journal for numerical methods in biomedical engineering*, 30(12):1679–1704, 2014. doi: https://doi.org/10.1002/cnm.2695.

[79] Wouter Huberts, Stefan GH Heinen, Niek Zonnebeld, Daniel AF van den Heuvel, Jean-Paul PM de Vries, Jan HM Tordoir, D Rodney Hose, Tammo Delhaas, and Frans N van de Vosse. What is needed to make cardiovascular models suitable for clinical decision support? a viewpoint paper. *Journal of computational science*, 24:68–84, 2018.

[80] B. Iooss, Da Veiga S., A. Janon, and G. Pujol. Sensitivity: Global sensitivity analysis of model output, r package version 1.26.0, 2021. URL `https://cran.r-project.org/package=sensitivity`.

[81] Bertrand Iooss and Paul Lemaître. A review on global sensitivity analysis methods. In *Uncertainty management in simulation-optimization of complex systems*, pages 101–122. Springer, 2015.

[82] Bertrand Iooss and Andrea Saltelli. *Introduction to Sensitivity Analysis*, pages 1–20. Springer INternational Publishing, 01 2015. doi: 10.1007/978-3-319-11259-6_31-1.

[83] A. Jafarinia, T. S. Müller, U. Windberger, G. Brenn, and T. Hochrainer. Blood rheology influence on false lumen thrombosis in type B aortic dissection. *J Biosci Bioeng*, 7:13–24, 2020.

[84] Alireza Jafarinia, Thomas Stephan Müller, Ursula Windberger, Günter Brenn, and Thomas Hochrainer. Blood rheology influence on false lumen thrombosis in type b aortic dissection. *Journal of Biomedical Engineering and Biosciences (JBEB)*, 7(1):1–8, 2020.

[85] Wei Jia, Brian McPherson, Feng Pan, Zhenxue Dai, and Ting Xiao. Uncertainty quantification of CO2 storage using bayesian model averaging and polynomial chaos expansion. *International Journal of Greenhouse Gas Control*, 71:104–115, 2018.

[86] David F Kallmes. Point: Cfd—computational fluid dynamics or confounding factor dissemination. *AJNR: American Journal of Neuroradiology*, 33(3):395, 2012.

[87] Robert E Kass and Adrian E Raftery. Bayes factors. *Journal of the american statistical association*, 90(430):773–795, 1995.

[88] T Kenner. The measurement of blood density and its meaning. *Basic research in cardiology*, 84(2):111–124, 1989.

[89] Z Kharboutly, M Fenech, JM Treutenaere, I Claude, and C Legallais. Investigations into the relationship between hemodynamics and vascular alterations in an established arteriovenous fistula. *Medical engineering & physics*, 29(9):999–1007, 2007.

[90] J.P.C Kleijnen and J.C Helton. Statistical analyses of scatterplots to identify important factors in large-scale simulations, 2: robustness of techniques. *Reliability Engineering & System Safety*, 65(2):187–197, 1999. ISSN 0951-8320. doi: https://doi.org/10.1016/S0951-8320(98)00090-8.

[91] C. Koutras, J. Pérez, K. Kardash, and M. A. Otaduy. A study of the sensitivity of biomechanical models of the spine for scoliosis brace design. *Computer Methods and Programs in Biomedicine*, 207:106125, 2021. ISSN 0169-2607. doi: https://doi.org/10.1016/j.cmpb.2021.106125.

[92] S Kucherenko and O Zaccheus. Sobolgsa software, 2017.

[93] Maya Landenhed, Gunnar Engström, Anders Gottsäter, Michael P Caulfield, Bo Hedblad, Christopher Newton-Cheh, Olle Melander, and J Gustav Smith. Risk profiles for aortic dissection and ruptured or surgically treated aneurysms: a prospective cohort study. *Journal of the American Heart Association*, 4(1):e001513, 2015.

[94] Loïc Le Gratiet, Stefano Marelli, and Bruno Sudret. *Metamodel-Based Sensitivity Analysis: Polynomial Chaos Expansions and Gaussian Processes*, pages 1289–1325. Springer International Publishing, Cham, 2017. ISBN 978-3-319-12385-1. doi: 10.1007/978-3-319-12385-1_38.

[95] CAD Leguy, EMH Bosboom, H Gelderblom, APG Hoeks, and FN Van de Vosse. Estimation of distributed arterial mechanical properties using a wave propagation model in a reverse way. *Medical engineering & physics*, 32(9):957–967, 2010.

[96] Fuyou Liang and Hao Liu. A closed-loop lumped parameter computational model for human cardiovascular system. *JSME International Journal Series C Mechanical Systems, Machine Elements and Manufacturing*, 48(4):484–493, 2005.

[97] Sofienne Mansouri, Tareq Alhadidi, Souhir Chabchoub, and Ridha Ben Salah. Impedance cardiography: recent applications and developments. *Biomedical Research*, 29(19):3542–3552, 2018.

[98] S. Marelli, N. Lüthen, and B. Sudret. Uqlab user manual – polynomial chaos expansions. Technical report, Chair of Risk, Safety and Uncertainty Quantification, ETH Zurich, Switzerland, 2021. Report # UQLab-V1.4-104.

[99] Stefano Marelli and Bruno Sudret. *UQLab: A Framework for Uncertainty Quantification in Matlab*, pages 2554–2563. American Society of Civil Engineers, 2014. doi: 10.1061/9780784413609.257.

Bibliography

[100] Frederic Martini and Michael J Timmons. *Fundamentals of Human Anatomy and Physiology*. Prentice Hall, 1995.

[101] James Clerk Maxwell. *A treatise on electricity and magnetism*, volume 1. Clarendon press, 1881.

[102] Gian Marco Melito, Vahid Badeli, Alice Reinbacher-Köstinger, and Katrin Ellermann. Sensitivity analysis for electrical detection of aortic dissection. *PAMM*, 19(1):e201900062, 2019. doi: https://doi.org/10.1002/pamm.201900062. URL `https://onlinelibrary.wiley.com/doi/abs/10.1002/pamm.201900062`.

[103] Gian Marco Melito, Alireza Jafarinia, Thomas Hochrainer, and Katrin Ellermann. Sensitivity analysis of a phenomenological thrombosis model and growth rate characterisation. *Journal of Biomedical Engineering and Biosciences (JBEB)*, 7(1):31–40, 2020.

[104] Gian Marco Melito, Alireza Jafarinia, Thomas Hochrainer, and Katrin Ellermann. Sensitivity analysis of a hemodynamic-based model for thrombus formation and growth. In *Proceedings of the 6th World Congress on Electrical Engineering and Computer Systems and Sciences (EECSS'20): ICBES'20*, 2020.

[105] G.M. Melito, T. S. Müller, V. Badeli, K. Ellermann, G. Brenn, and A. Reinbacher-Köstinger. Sensitivity analysis study on the effect of the fluid mechanics assumptions for the computation of electrical conductivity of flowing human blood. *Reliability Engineering & System Safety*, 213:107663, 2021. ISSN 0951-8320. doi: https://doi.org/10.1016/j.ress.2021.107663.

[106] C. Menichini and X.Y. Xu. Mathematical modeling of thrombus formation in idealized models of aortic dissection: initial findings and potential applications. *Journal of mathematical biology*, 73(5):1205–1226, 2016.

[107] C. Menichini, Z. Cheng, R. G. J. Gibbs, and X. Y. Xu. Predicting false lumen thrombosis in patient-specific models of aortic dissection. *J R Soc Interface*, 13(124), 2016.

[108] E. W. Merrill. Rheology of blood. *Physiological Reviews*, 49(4):863–888, 1969. doi: 10.1152/physrev.1969.49.4.863.

[109] E. W. Merrill, E. R. Gilliland, G. Cokelet, H. Shin, A. Britten, and R. E. Wells. Rheology of human blood, near and at zero flow: effects of temperature and hematocrit level. *Biophysical Journal*, 3(3):199–213, 1963. doi: 10.1016/S0006-3495(63)86816-2.

[110] Istvan Meszaros, Jozsef Morocz, Jozsef Szlavi, Janos Schmidt, Laszlo Tornoci, Laszlo Nagy, and Laszlo Szép. Epidemiology and clinicopathology of aortic dissection. *Chest*, 117(5):1271–1278, 2000.

[111] A. B. Metzner and J. C. Reed. Flow of non-newtonian fluids - correlation of the laminar, transition, and turbulent-flow regions. *American Institute of Chemical Engineers*, 1(4): 434–440, 1955. doi: 10.1002/aic.690010409.

[112] Gerald E. Miller. Chapter 14 - biomedical transport processes. In John D. Enderle and Joseph D. Bronzino, editors, *Introduction to Biomedical Engineering (Third Edition)*, Biomedical Engineering, pages 937–993. Academic Press, Boston, third edition edition, 2012. ISBN 978-0-12-374979-6. doi: https://doi.org/10.1016/B978-0-12-374979-6.00014-9.

[113] Raad H Mohiaddin, Philip J Kilner, Simon Rees, and Donald B Longmore. Magnetic resonance volume flow and jet velocity mapping in aortic coarctation. *Journal of the American College of Cardiology*, 22(5):1515–1521, 1993.

[114] Douglas C Montgomery. *Design and analysis of experiments*. John wiley & sons, 2017.

[115] Max D Morris. Factorial sampling plans for preliminary computational experiments. *Technometrics*, 33(2):161–174, 1991.

[116] Horacio Murillo, Lior Molvin, Anne S. Chin, and Dominik Fleischmann. Aortic dissection and other acute aortic syndromes: Diagnostic imaging findings from acute to chronic longitudinal progression. *RadioGraphics*, 41(2):425–446, 2021. doi: 10.1148/rg.2021200138.

[117] D. Mutua, E. N. M. Njagi, and G. O. Orinda. Hematological profile of normal pregnant women. *Journal of Blood & Lymph*, 8(2):1–6, 2018. doi: 10.4172/2165-7831.1000220.

[118] Foeke JH Nauta, Santi Trimarchi, Arnoud V Kamman, Frans L Moll, Joost A Van Herwaarden, Himanshu J Patel, C Alberto Figueroa, Kim A Eagle, and James B Froehlich. Update in the management of type b aortic dissection. *Vascular Medicine*, 21(3):251–263, 2016.

[119] Jeremy E Oakley and Anthony O'Hagan. Probabilistic sensitivity analysis of complex models: a bayesian approach. *Journal of the Royal Statistical Society: Series B (Statistical Methodology)*, 66(3):751–769, 2004.

[120] Robert V O'Neill. Error analysis of ecological models. Technical report, Oak Ridge National Lab., Tenn., 1971.

[121] World Health Organization. Cardiovascular diseases (CVDs), 2021. URL `https://www.who.int/news-room/fact-sheets/detail/cardiovascular-diseases-(cvds)`.

[122] Francesca Pianosi and Thorsten Wagener. A simple and efficient method for global sensitivity analysis based on cumulative distribution functions. *Environmental Modelling & Software*, 67:1–11, 2015.

[123] Francesca Pianosi, Fanny Sarrazin, and Thorsten Wagener. A matlab toolbox for global sensitivity analysis. *Environmental Modelling & Software*, 70:80–85, 2015.

Bibliography

[124] Nico HJ Pijls, Berry Van Gelder, Pepijn Van der Voort, Kathinka Peels, Frank ALE Bracke, Hans JRM Bonnier, and Mamdouh IH El Gamal. Fractional flow reserve: a useful index to evaluate the influence of an epicardial coronary stenosis on myocardial blood flow. *Circulation*, 92(11):3183–3193, 1995.

[125] L. Pochhammer. Ueber die differentialgleichung der allgemeineren hypergeometrischen reihe mit zwei endlichen singulären punkten. *Journal für die reine und angewandte Mathematik (Crelles Journal)*, 1888(102):76–159, 1888. doi: doi:10.1515/crll.1888.102.76.

[126] René Prêtre and Ludwig K Von Segesser. Aortic dissection. *The Lancet*, 349(9063): 1461–1464, 1997.

[127] Sjeng Quicken, Wouter P Donders, Emiel MJ van Disseldorp, Kujtim Gashi, Barend ME Mees, Frans N van de Vosse, Richard GP Lopata, Tammo Delhaas, and Wouter Huberts. Application of an adaptive polynomial chaos expansion on computationally expensive three-dimensional cardiovascular models for uncertainty quantification and sensitivity analysis. *Journal of Biomechanical Engineering*, 138(12), 2016.

[128] Herschel Rabitz and Ömer F Aliş. General foundations of high-dimensional model representations. *Journal of Mathematical Chemistry*, 25(2-3):197–233, 1999.

[129] Sascha Ranftl, Gian Marco Melito, Vahid Badeli, Alice Reinbacher-Köstinger, Katrin Ellermann, and Wolfgang von der Linden. On the diagnosis of aortic dissection with impedance cardiography: A bayesian feasibility study framework with multi-fidelity simulation data. *Proceedings*, 33(1), 2019. ISSN 2504-3900. doi: 10.3390/proceedings2019033024. URL `https://www.mdpi.com/2504-3900/33/1/24`.

[130] Sascha Ranftl, Gian Marco Melito, Vahid Badeli, Alice Reinbacher-Köstinger, Katrin Ellermann, and Wolfgang von der Linden. Bayesian uncertainty quantification with multi-fidelity data and gaussian processes for impedance cardiography of aortic dissection. *Entropy*, 22(1), 2020. ISSN 1099-4300. doi: 10.3390/e22010058. URL `https://www.mdpi.com/1099-4300/22/1/58`.

[131] Saman Razavi and Hoshin V. Gupta. A new framework for comprehensive, robust, and efficient global sensitivity analysis: 1. theory. *Water Resources Research*, 52(1):423–439, 2016. doi: https://doi.org/10.1002/2015WR017558.

[132] Saman Razavi and Hoshin V. Gupta. A new framework for comprehensive, robust, and efficient global sensitivity analysis: 2. application. *Water Resources Research*, 52(1):440–455, 2016. doi: https://doi.org/10.1002/2015WR017559.

[133] Saman Razavi, Anthony Jakeman, Andrea Saltelli, Clémentine Prieur, Bertrand Iooss, Emanuele Borgonovo, Elmar Plischke, Samuele Lo Piano, Takuya Iwanaga, William Becker, Stefano Tarantola, Joseph H.A. Guillaume, John Jakeman, Hoshin Gupta, Nicola Melillo,

Giovanni Rabitti, Vincent Chabridon, Qingyun Duan, Xifu Sun, Stefán Smith, Razi Sheikholeslami, Nasim Hosseini, Masoud Asadzadeh, Arnald Puy, Sergei Kucherenko, and Holger R. Maier. The future of sensitivity analysis: An essential discipline for systems modeling and policy support. *Environmental Modelling & Software*, 137:104954, 2021. ISSN 1364-8152. doi: https://doi.org/10.1016/j.envsoft.2020.104954.

[134] Alice Reinbacher-Köstinger, Vahid Badeli, Gian Marco Melito, Christian Magele, and Oszkar Bíró. Numerical simulation of various electrode configurations in impedance cardiography to identify aortic dissection. In Pedro Bertemes-Filho, editor, *17th International Conference on Electrical Bioimpedance*, pages 51–54, Singapore, 2020. Springer Singapore. ISBN 978-981-13-3498-6.

[135] Alice Reinbacher-Köstinger, Vahid Badeli, Oszkár Bíró, and Christian Magele. Numerical simulation of conductivity changes in the human thorax caused by aortic dissection. *IEEE Transactions on Magnetics*, 55(6):1–4, 2019. doi: 10.1109/TMAG.2019.2895418.

[136] William C Roberts. Aortic dissection: anatomy, consequences, and causes. *American heart journal*, 101(2):195–214, 1981.

[137] Trimarchi S., Tolenaar J.L., Jonker F.H.W., Murray B., Tsai T.T., Eagle K.A., Rampoldi V., Verhagen H.J.M., van Herwaarden J.A., Moll F.L., Muhs B.E., and Elefteriades J.A. Importance of false lumen thrombosis in type b aortic dissection prognosis, 2013. ISSN 0022-5223. Proceedings of the Aortic Symposium 2012.

[138] Michaela Saisana, Andrea Saltelli, and Stefano Tarantola. Uncertainty and sensitivity analysis techniques as tools for the quality assessment of composite indicators. *Journal of the Royal Statistical Society: Series A (Statistics in Society)*, 168(2):307–323, 2005.

[139] K. Sakamoto and H. Kanai. Electrical characteristics of flowing blood. *IEEE Transactions on Biomedical Engineering*, BME-26(12):686–695, 1979. doi: 10.1109/TBME.1979.326459.

[140] Andrea Saltelli. Making best use of model evaluations to compute sensitivity indices. *Computer physics communications*, 145(2):280–297, 2002.

[141] Andrea Saltelli. A short comment on statistical versus mathematical modelling. *Nature communications*, 10(1):1–3, 2019.

[142] Andrea Saltelli, Stefano Tarantola, Francesca Campolongo, et al. Sensitivity anaysis as an ingredient of modeling. *Statistical Science*, 15(4):377–395, 2000.

[143] Andrea Saltelli, Stefano Tarantola, Francesca Campolongo, and Marco Ratto. *Sensitivity analysis in practice: a guide to assessing scientific models*, volume 1. Wiley Online Library, 2004.

Bibliography

[144] Andrea Saltelli, Marco Ratto, Stefano Tarantola, Francesca Campolongo, European Commission, et al. Sensitivity analysis practices: Strategies for model-based inference. *Reliability Engineering & System Safety*, 91(10-11):1109–1125, 2006.

[145] Andrea Saltelli, Marco Ratto, Terry Andres, Francesca Campolongo, Jessica Cariboni, Debora Gatelli, Michaela Saisana, and Stefano Tarantola. *Global sensitivity analysis: the primer.* John Wiley & Sons, 2008.

[146] Andrea Saltelli, Paola Annoni, Ivano Azzini, Francesca Campolongo, Marco Ratto, and Stefano Tarantola. Variance based sensitivity analysis of model output. Design and estimator for the total sensitivity index. *Computer physics communications*, 181(2):259–270, 2010.

[147] Hua Shen, Siqi Li, Yu Wang, and Kai-Rong Qin. Effects of the arterial radius and the center-line velocity on the conductivity and electrical impedance of pulsatile flow in the human common carotid artery. *Medical & biological engineering & computing*, 57(2): 441–451, 2019. doi: 10.1007/s11517-018-1889-x.

[148] Ilya M Sobol. Sensitivity estimates for nonlinear mathematical models. *Mathematical modelling and computational experiments*, 1(4):407–414, 1993.

[149] Ilya M Sobol. Global sensitivity indices for nonlinear mathematical models and their monte carlo estimates. *Mathematics and computers in simulation*, 55(1-3):271–280, 2001.

[150] Il'ya Meerovich Sobol. On sensitivity estimation for nonlinear mathematical models. *Matematicheskoe modelirovanie*, 2(1):112–118, 1990.

[151] IM Sobol and S Kucherenko. Derivative based global sensitivity measures. *Procedia-Social and Behavioral Sciences*, 2(6):7745–7746, 2010.

[152] Jong-Min Song, Sung-Doo Kim, Jeong-Hoon Kim, Mi-Jeong Kim, Duk-Hyun Kang, Joon Beom Seo, Tae-Hwan Lim, Jae Won Lee, Meong-Gun Song, and Jae-Kwan Song. Long-term predictors of descending aorta aneurysmal change in patients with aortic dissection. *Journal of the American College of Cardiology*, 50(8):799–804, 2007.

[153] L Speelman, EMH Bosboom, GWH Schurink, FAMVI Hellenthal, J Buth, M Breeuwer, MJ Jacobs, and FN van de Vosse. Patient-specific aaa wall stress analysis: 99-percentile versus peak stress. *European Journal of Vascular and Endovascular Surgery*, 36(6):668–676, 2008.

[154] A. F. Stalder, A. Frydrychowicz, M. F. Russe, J. G. Korvink, J. Henning, K. Li, and M. Markl. Assessment of flow instabilities in the healthy aorta using flow-sensitive MRI. *Journal of magnetic resonance imaging*, 33:839–846, 2011. doi: 10.1002/jmri.22512.

[155] Nikos Stergiopulos, Berend E Westerhof, and Nico Westerhof. Total arterial inertance as the fourth element of the windkessel model. *American Journal of Physiology-Heart and Circulatory Physiology*, 276(1):H81–H88, 1999.

[156] NMJWN Stergiopulos, JJ Meister, and N Westerhof. Evaluation of methods for estimation of total arterial compliance. *American Journal of Physiology-Heart and Circulatory Physiology*, 268(4):H1540–H1548, 1995.

[157] Jacob Sturdy, Johannes Kløve Kjernlie, Hallvard Moian Nydal, Vinzenz G Eck, and Leif R Hellevik. Uncertainty quantification of computational coronary stenosis assessment and model based mitigation of image resolution limitations. *Journal of Computational Science*, 31:137–150, 2019.

[158] Bruno Sudret. Global sensitivity analysis using polynomial chaos expansions. *Reliability engineering & system safety*, 93(7):964–979, 2008.

[159] Tech Me Surgery. Aortic dissection, 05/2021. URL `https://teachmesurgery.com/vascular/arterial/aortic-dissection/`.

[160] Stefano Tarantola, A Corradi, P Ruffo, and Andrea Saltelli. Global sensitivity analysis techniques for the analysis of the oil potential of sedimentary beams, Jul 2001.

[161] J. O. Taylor, R. S. Meyer, S. Deutsch, and K. B. Manning. Development of a computational model for macroscopic predictions of device-induced thrombosis. *Biomechanics and modeling in mechanobiology*, 15(6):1713–1731, 2016.

[162] J.O. Taylor, K.P. Witmer, T. Neuberger, B.A. Craven, R. S. Meyer, S. Deutsch, and K. B. Manning. In vitro quantification of time dependent thrombus size using magnetic resonance imaging and computational simulations of thrombus surface shear stresses. *Journal of Biomechanical Engineering*, 136(7):071012, 2014.

[163] Gary A Thibodeau and Kevin T Patton. Anatomy and physiology 4° edition. *Support and Movement*, pages 162–314, 1999.

[164] G. B. Thurston. Viscoelasticity of human blood. *Biophysical Journal*, 12:1205–1217, 1972. doi: 10.1016/S0006-3495(72)86156-3.

[165] Jip L Tolenaar, Jasper W Van Keulen, Santi Trimarchi, Frederik HW Jonker, Joost A Van Herwaarden, Hence JM Verhagen, Frans L Moll, and Bart E Muhs. Number of entry tears is associated with aortic growth in type b dissections. *The Annals of thoracic surgery*, 96(1):39–42, 2013.

[166] Santi Trimarchi, Christoph A Nienaber, Vincenzo Rampoldi, Truls Myrmel, Toru Suzuki, Eduardo Bossone, Valerio Tolva, Michael G Deeb, Gilbert R Upchurch Jr, Jeanna V Cooper, et al. Role and results of surgery in acute type b aortic dissection: insights from the international registry of acute aortic dissection (irad). *Circulation*, 114(1_supplement): I–357, 2006.

[167] Thomas T Tsai, Arturo Evangelista, Christoph A Nienaber, Truls Myrmel, Gabriel Meinhardt, Jeanna V Cooper, Dean E Smith, Toru Suzuki, Rossella Fattori, Alfredo Llovet, et al. Partial thrombosis of the false lumen in patients with acute type b aortic dissection. *New England Journal of Medicine*, 357(4):349–359, 2007.

[168] M. Ulbrich, J. Mühlsteff, S. Leonhardt, and M. Walter. Influence of physiological sources on the impedance cardiogram analyzed using 4d fem simulations. *Physiological measurement*, 35:1451, 2014. doi: 10.1088/0967-3334/35/7/1451.

[169] PCJ Vergouwen, T Collee, and JJM Marx. Haematocrit in elite athletes. *International journal of sports medicine*, 20(08):538–541, 1999.

[170] Klaas R Visser. Electric conductivity of stationary and flowing human blood at low frequencies. In *Images of the Twenty-First Century. Proceedings of the Annual International Engineering in Medicine and Biology Society*, pages 1540–1542. IEEE, 1989. doi: 10.1109/IEMBS.1989.96329.

[171] K.R. Visser. Electric properties of flowing blood and impedance cardiography. *Annals of biomedical engineering*, 17(5):463–473, 1989. doi: 10.1007/BF02368066.

[172] H. K. Walker, W. D. Hall, and J. W. Hurst. *Clinical Methods: The History, Physical, and Laboratory Examinations.* Boston : Butterworths, 3 edition, 1990.

[173] R. E. Wells and E. W. Merrill. The variability of blood viscosity. *The American Journal of Medicine*, 31(4):505–509, 1961. doi: 10.1016/0002-9343(61)90134-6.

[174] Norbert Wiener. The homogeneous chaos. *American Journal of Mathematics*, 60(4): 897–936, 1938.

[175] A Winnerkvist, U Lockowandt, E Rasmussen, and K Rådegran. A prospective study of medically treated acute type b aortic dissection. *European journal of vascular and endovascular surgery*, 32(4):349–355, 2006.

[176] Arik Wolak, Heidi Gransar, Louise EJ Thomson, John D Friedman, Rory Hachamovitch, Ariel Gutstein, Leslee J Shaw, Donna Polk, Nathan D Wong, Rola Saouaf, et al. Aortic size assessment by noncontrast cardiac computed tomography: normal limits by age, gender, and body surface area. *JACC: Cardiovascular Imaging*, 1(2):200–209, 2008.

[177] J. R. Womersley. Method for the calculation of velocity, rate of flow and viscous drag in arteries when the pressure gradient is known. *Journal of Physiology*, 127:553–563, 1955. doi: 10.1113/jphysiol.1955.sp005276.

[178] J. R. Womersley. Oscillatory flow in arteries: the constrained elastic tube as a model of arterial flow and pulse transmission. *Physics in medicine and biology*, 2(2):178–187, 1957.

[179] Dongbin Xiu. *Numerical methods for stochastic computations*. Princeton university press, 2010.

[180] Dongbin Xiu and George Em Karniadakis. Modeling uncertainty in steady state diffusion problems via generalized polynomial chaos. *Computer methods in applied mechanics and engineering*, 191(43):4927–4948, 2002.

[181] Dongbin Xiu and George Em Karniadakis. The wiener–askey polynomial chaos for stochastic differential equations. *SIAM journal on scientific computing*, 24(2):619–644, 2002.

[182] Huijuan Xu, Davide Baroli, and Alessandro Veneziani. Global sensitivity analysis for patient-specific aortic simulations: the role of geometry, boundary condition and les modeling parameters. *Journal of Biomechanical Engineering*, 2020.

[183] Josef Šťásek, Petr Němec, and Jiří Vítovec. Summary of the 2014 esc guidelines on the diagnosis and treatment of aortic diseases: Prepared by the czech society of cardiology. *Cor et Vasa*, 57(4):e297–e319, 2015. ISSN 0010-8650. doi: https://doi.org/10. 1016/j.crvasa.2015.05.001. URL `https://www.sciencedirect.com/science/article/pii/S0010865015000466`.